NTNU – Trondheim
Norwegian University of
Science and Technology

Energy storage, and design of tractive system for EV application

Eirik Børsheim
Martin Standal Skåravik

Master of Energy and Environmental Engineering
Submission date: June 2014
Supervisor: Trond Toftevaag, ELKRAFT

Norwegian University of Science and Technology
Department of Electric Power Engineering

Problem description

This master thesis work is performed as part of the project developing Norway's first ever electric racecar. The objective of the thesis is to design and develop a complete accumulator system for the tractive system of this prototype racecar. Focus is set on studying the relevant technologies for energy storage in EV applications from available literature and manufacturer data, testing of battery cells for proper dimensioning of discharge capability and capacity, modelling the system through simulation software and laboratory, as well as in car, testing of the complete system.

The work will be based on available literature, innovative design using Visio for circuit visualization, Simulink and Matlab for simulation work and Solidworks for 3D modelling.

Acknowledgements

We would like to express our deepest gratitude to Prof. Magnus Thomassen at SINTEF Materials and Chemistry for taking the time to assist our work with theoretical guidance and facilitating battery tests. Without his advice and the test equipment made available by him, this master thesis work would not be possible to conduct.

Also, we extend our appreciation to Bård Almås and Svein Erling Norum at the department of electrical engineering, NTNU, for helping us with practical challenges and lending out the needed equipment during the thesis work. We would also like to extend our appreciation to Dominik Háger and Erland Strendo at the workshop at the department of electrical engineering, who have assisted us with prototyping, tools and ideas.

Since constructing a race-car is a team effort, much help has been received from the Revolve NTNU team during the whole process. Special thanks to Henrik Meland, Kristian Roaldsnes, Olav Ljøkjel and Victor Iversen for helping with PCB design and EMI – testing. Eivind Bere, Anders Broen and Kristian Brox from the Revolve NTNU team have also been crucial in the whole process of integrating the battery management- and charging system.

All the companies cooperating with Revolve NTNU have also been intricate in completing this thesis, and obtaining such a spectacular result. A special thanks to James Walker, Melasta Inc, Kabelpartner, Kongsberg Gruppen and Valeo for offering services and equipment free of charge. Without their help, Norways first ever electrical racecar would be nothing but an idea on paper.

Last but not least, we would like to thank our supervisor Trond Toftevåg for taking on this rather unconventional master thesis and helping us through the process.

11.06.2014

---------- ----------

Eirik Børsheim & Martin Skåravik

Abstract

The efficiency and specific power of electrical motors have for decades been superior to the combustion motors. With the arrival of modern permanent magnet motors the advantage of electrical propulsion for vehicles now greater than ever. Energy storage has previously been the restraining factor, but with the arrival of stable durable lithium – ion batteries the conventional car market has seen an exponential increase in the sales of electric vehicles. This development has also been picked up by the racecar niche markets and new full electric racecar competitions are being conceived all over the world. The purpose of the work presented in this thesis is to design, build and test a tractive system accumulator system for a prototype racecar.

In the thesis work, an extensive literature study and market survey is performed to evaluate the energy storage technology relevant for the system. Lithium - CoO_2 cells are chosen for their high energy density and have been subjected to testing with regards to performance in load situations relevant to racing operation and evaluation of the Peukert's effect. Cycle life is also evaluated for the variable load and the effect of resting the battery during discharge is studied. Using the Simulink add in for Matlab, a battery system model is developed, calibrated and used to estimate the required capacity in a battery system.

A complete automated system monitoring battery parameters and insulation quality as well as allowing manual shutdown is designed and presented. The system was thoroughly tested with regards to functionality using a water – break setup prior to installation in a prototype racecar. The effect of EMI in EV is discussed and tested.

Tests indicate that the Peukert's effect for LCO batteries is far inferior to the modern lead – acid batteries, and that a good approximation can be achieved for the variable load situation when modelled with the average current. Lifespan of the LCO batteries is proven to be affected positively in the variable load case and further improved by allowing the battery a rest time during discharge. The complete system is installed in a race-car and show excellent performance.

Preface

Revolve NTNU is an independent student organization aiming at educating Norways finest engineers. This is done through designing, producing and building a complete racecar from scratch each year. The 2014 team started the work towards constructing Norway's first ever electrical racecar in the spring of 2013 and is still going. The final objective for the team is to enter the Formula Student competitions in Germany and England, which take place in the summer of 2014. The project is funded by its main sponsor Kongsberg - gruppen, and by several other cooperating businesses as well as by the Norwegian University of Science and Technology.

Our role in the project has been to design and develop an energy storage system and the electrical high voltage system in the car. All the design work and testing is done by us, together with our colleagues in Revolve NTNU. The investigation focuses on creating an accumulator system with the highest specific energy ever seen in a tractive system battery and ensuring a fool-proof safety system, ensuring the absolute safety of the driver and the operating personnel of the car.

This thesis gives insight in the available market for relevant energy storage technology, the performance of lithium – ion battery cells at various load situations and modelling of battery systems in Simulink. It also presents the complete design of a functioning tractive system for a prototype racecar.

The results of the thesis work can be used by the upcoming teams and students entering the electric racecar market.

Sammendrag

Elektriske maskiner har i en årrekke vært forbrenningsmotorene overlegen i forhold til effektivitet. Med de nye permanentmagnet – maskinene er fordelen av elektrisk fremdrift i kjøretøy nå større enn noen gang. Teknologien for energilagring har tidligere vært den begrensende faktoren, men med inntoget av moderne stabile lithium – ion batterier ser man nå en eksponensiel økning i salget av konvensjonelle elektriske kjøretøy. Denne utviklingen er også overført til racerbil – miljøet, hvor nye elektriske konkurranser unnfanges årlig. Målet med denne masteroppgaven er å designe, produsere og gjennomteste ett komplett energilagringssystem med tilhørende sikkerhetsfunksjoner til Norges første elektriske racerbil.

Under arbeidet med oppgaven er det gjennomført ett omfattende litteratur- og markeds – søk på relevant teknologi for energilagring i elektriske kjøretøy. Lithium – ion celler basert på en kobolt-dioksid – katode er valgt grunnet den ekstreme spesifikke energien denne kjemiske sammensetningen tillater. Cellene er gjennomtestet med fokus på virkningsgrad ved høyt strømtrekk og oppførsel ved en typisk lastsituation for en elektrisk racerbil. Levetid og kartlegging av Peukert's effekt er studert gjennom laberatorietesting. Simulink – tillegget til Matlab er brukt for å etablere å konfigurere en komplett modell for å estimere nødvendig energi i systemet. Modellen har vist svært presis oppførsel i forhold til resultatene fra laberatorietestene.

Ett komplett automatisert sikkerhets-system er utviklet for å overvåke tilstanden til batteri og isolasjon under kjøring og lading. Dette systemet er funksjonalitetstestet i lab og installert i bil. Nødvendigheten av EMI – beskyttelse er også testet og evaluert.

Testene viser at Peukert's effekt for de valgte kobolt-dioksid baserte batteriene er svært lav sammenligned med for eksempel bly – syre batterier. Resultatene indikerer også at en god approksimasjon av battericellens oppførsel kan gjøres ved å modellere Peukert's effekt ved hjelp av lastprofilens gjennomsnittlige strøm. Ved en variabel lastprofil viser det seg også at batterienes levetid estimeres med større treffsikkerhet ved å bruke profilens gjennomsnittlige strøm. Testene indikerer dermed at korte forhøynede strømpulser ikke akselerer degraderingen av batteriet.

Hele systemet er installert i bil og er bevist funksjonelt. Grunnet problemer med telemetrien har ikke teamet i Revolve NTNU maktet å hente ut data i tide.

Abbreviations

AIR – Accumulator isolation relay

AMS – Accumulator management system

BOTS – Brake over travel switch

BSPD – Brake system plausibility device

CAD – Computer aided design

DOD – Depth of discharge

ECU – Engine control unit

EMI – Electromagnetic interference

EV – Electric vehicle

GLV – Grounded low voltage system

GLVMS – Grounded low voltage main switch

HEV - Hybrid electric vehicle

HV – High voltage

HVD – High voltage disconnect

KA – Kongsberg Automotive

IGBT – Insulated gate bipolar transistor

IMD – Insulation monitoring device

LCO – Cobalt dioxide based lithium battery

LFP – Iron phosphorus based lithium battery

LMO – Manganese oxide based lithium battery

LV – Low voltage

NCA – Nickel cobalt aluminum lithium battery

NI – National instruments

NiCd – Nickel cadmium

NiMH – Nickel metal hydrate

NMC – Nickel manganese cobalt based lithium battery

PHEV – Plug – in Hybrid electric vehicle

PMSM – Permanent magnet synchronous motor

SOC – State of charge

SOH – State of health

TSAL – Tractive system active light

TSMP – Tractive system measuring points

VRLA – Valve regulated lead acid

Table of Contents

List of figures

List of tables

1. Introduction

Over the last decade electric vehicles, EVs, and hybrid electric vehicles, HEVs, have been successfully introduced to the automotive market. From the introduction of the GM Impact in 1990 to the bestselling full electric passenger cars like the Tesla S and Nissan Leaf presented in 2013, the development has been exponentially accelerating. With the recent development of the permanent magnet synchronous motor, the race car – industry have recognized the advantages of the superior torque output and efficiency. This has led to the FIA Formula Electric Championships being conceived in 2012 and the FSEA expanding to electrical propulsion competing side by side with combustion cars.

1.1. Formula student

Now being the world's biggest engineering competition for students, the formula student competition was started as the SAE Mini Indy in 1978. At present, the competition includes a number of events all over the world. In 2010, a full electric class was introduced to the Formula Student UK competition and already in 2013 the competition saw its first full electric car overall champion as AMZ Racing from ETH Zurich stormed to victory with their car "Julier".

The competition is divided into 8 different events, whereas the obtainable points are distributed between static and dynamic events as seen in Figure 1-1. A total of 1000 points can be obtained.

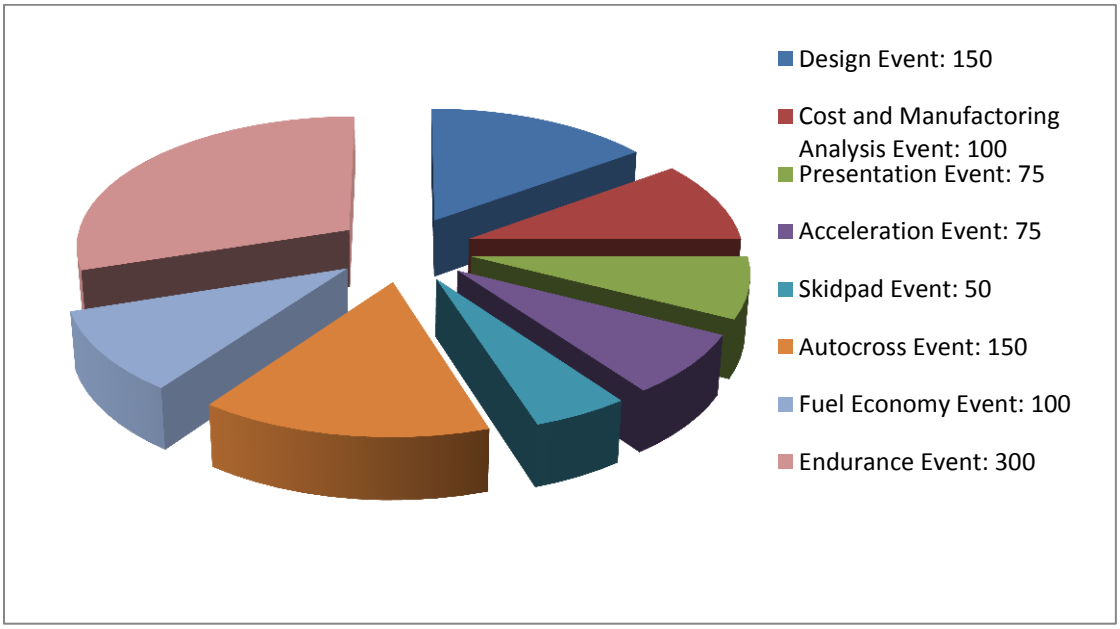

Figure 1-1: Overview of points and events for the Formula Student Competition.

The static events are design, cost and presentation. The points distributed in these events are independent of the actual performance of the car, and instead focus on the design process and cost of the chosen solutions. On the other hand, the dynamic events are all about the driving abilities of the car. Acceleration event is based on a 75 m long sprint, where points are distributed based on the finishing time. The skidpad event tests the car performance on a wet tarmac, and in the autocross event the car runs through a curvy track of about 1 km in a time trail competition. The most important event of the competition is the endurance event, where the car has to complete 23 laps on a track set up by Formula Student.

1.2. Revolve NTNU

The Norwegian University of Science and Technology student organization Revolve NTNU was founded in 2010, and entered their first ever Formula Student competition in 2012 with the combustion race car KA Borealis R. The first team consisted of 23 members from 6 different engineering departments at NTNU. At the FSAE UK event the team achieved high remarks and was awarded with the "best newcomer award" and finished in 17th place from 102 starting teams from around the globe. The following year, Revolve NTNU expanded its team to 46 members, with 30 of the members being new recruits. As a second year car, Revolve NTNU achieved a 16th place overall and received the National Instruments Measurements and Control Award for the electronic and control system of the car. To further build on the swift development of the organization, Revolve NTNU decided to make their third project to develop Norway's first ever electric race car.

The writers of this master thesis work have connected the voluntary work in the Revolve NTNU organization as part of the master studies at NTNU. As members of the technical management group, group leader for the battery and management system and electrical systems officer, our tasks in the team has been the development of the tractive system accumulator and the high voltage transmission system for the electrical drivetrain of the car. Our orientation in the organization structure can be seen in Figure 1-2.

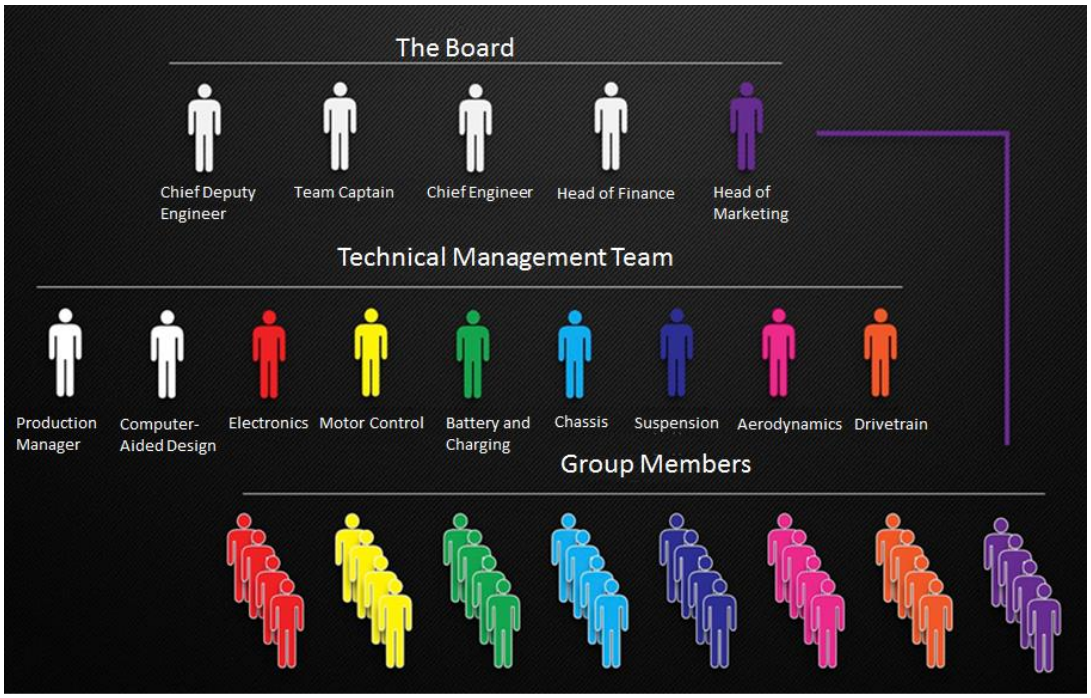

Figure 1-2: Overview of the organization structure in Revolve NTNU team 2014.

1.3. Purpose

The purpose of the master thesis is to design and development, through theoretical modelling, benchmarking and system testing, the tractive system in Norway's first electric race car. Special emphasis has been set on mapping the battery market to choose the optimal technology and design of the desired battery cells. Modelling the system for theoretical estimation of performance requirements has been combined with extensive benchmarking tests to properly calibrate the model. The report also focuses on the safety aspects of lithium – ion batteries and life – span estimation of the cells chosen for the application. The work accumulates to integrating this with the safety system and finally building a prototype race car for international competitions.

1.4. Outline

An extensive literature study and market survey of energy storage technology in the present market is presented in chapter 2 together with theory regarding safety aspects and life-span estimation of lithium – Ion batteries. In chapter 3, a literature study regarding battery monitoring systems and cell balancing is summarized. The important design considerations taken into account in the thesis work are presented in chapter 4. This chapter includes the battery parameters, safety circuitry, charging system, electrical connections and electromagnetic interference. In chapter 5, the software used as design tools and for simulation work is presented together

with the relevant racing situation load curve obtained. Following the theoretical background for design, the complete design of the developed system is presented in chapter 6. How this design is set up in tractive system tests using a water break setup is explained in chapter 7. In chapter 8, the experimental battery cell evaluation tests are presented. The simulations results are summarized together with the single cell battery tests in chapter 9. Results from tractive system tests are presented in chapter 10. In chapter 11 the test results and complete system design is discussed. Conclusions and further work is recapped in chapter 12.

2. A literature- and market study of energy storage for automotive purposes

2.1. General

Despite the fact that electrical machines have been superior to combustion engines for decades in terms of specific power and efficiency, the modern market is still dominated by vehicles burning fossil fuels. The technical limitations of the available energy storage alternatives to power an electrical machine have been the main reason for this situation. Due to vast resources being pumped into research and development towards more sustainable energy sources for commercial and private transportations, huge leaps have been made in battery and fuel cell technology.

The commercial market for batteries is distributed in various types based on different materials, chemical reactions and they come in all shapes and sizes. Many of these have been or are still relevant for the electrical vehicles, EVs, but the majority is not. Figure 2-1 visualizes the main groups of energy storage relevant for EV application.

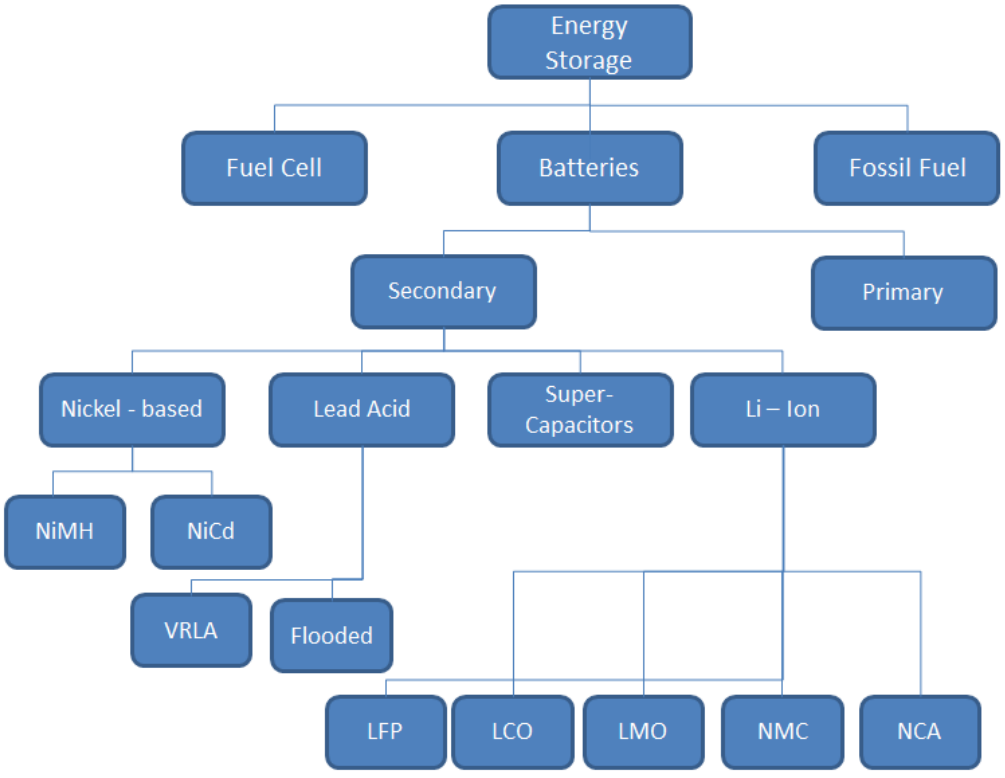

Figure 2-1 : Overview of the topics attended to in this literature and marked study of energy storage for automotive purposes.

Primary batteries are based on non-reversible chemical reactions, and can therefore only be discharged once [1]. Even though these batteries have very low costs as compared to secondary batteries, the share impracticality of changing the accumulator system at every discharge cycle, together with the potential waste – problem it would pose, leads to the primary battery technology being irrelevant as foundation for energy storage in EVs. Secondary batteries on the other hand, are based on reversible chemical reactions that permit the battery to accept as well as release charge.

The focus of this chapter will be comparing the critical parameters for the different technologies and discussing the applicability to electrical vehicles. The most important parameters attended to in this thesis work for a tractive system battery are described in Table 2-1. Safety concerns are also discussed later in the section.

Cyclic lifespan	Cycles (100 DOD @ 0.5 C)
Specific energy	kWh/kg
Energy density	kWh/l
Specific power	kW/kg
Cost	$ / kWh
Efficiency	% (@ 0.5C)

Table 2-1: Critical parameters for a tractive system battery cell.

Improving any one of these qualities for a certain battery cell always comes at the compromise of another. The values presented in in chapters 2.2 to 2.5 are therefore based on the best obtainable values for the given battery technology, and all parameters are not necessarily based on the same battery cell. With regards to safety, the term abused is used to describe poor handling of batteries, both mechanically and electrically. This implies i.e. discharging or charging to states beyond recommended values or when subjected to elevated currents.

Capacity, expressed in Ampere – hours is defined as the available current the battery can supply over a given period of time [1], and is a measure of electrical charge.

$$Q = \int_{t_1}^{t_2} I dt \tag{2.1}$$

During both discharge and charge, equation (2.1) gives the electrical charge received or supplied during the time period $t_1 - t_2$. Manufacturers assign a rated capacity to their batteries, giving the amount of charge a new battery should be able to deliver from a fully charged state to a completely discharged state. A battery rated for 7000 mAh should be able to deliver 7000 mA for one hour. The efficiency of a battery will vary with the current – level to which it is subjected, and the capacity is commonly referred to at a certain C – rate. The C-rating of a battery is defined from equation(2.2).

$$C_{rate} = \frac{I_{discharge}}{Q_{rated}} \tag{2.2}$$

Where $I_{discharge}$ is the discharge current and Q_{rated} is the rated capacity. Using this, it becomes evident that discharging a cell rated at 7000 mAh cell with a discharge current of 3500 mA translates to 0.5 C.

The open circuit voltage over a battery cell is a direct function of the amount of charge in the battery, or the "state of Charge". When the battery is fully charged, the SOC is 100%, and when fully discharged SOC is 0%. Manufacturers often set a high and low operational voltage limit for their batteries which can be directly compared to the state of charge, SOC, of the battery [2].

Due to degradation mechanisms the battery's capacity will fade with time and use. To determine the state of the battery, the term state of health, or SOH, is applied. The SOH calculations refer the general state of the battery at a given time directly to the initial capacity of the battery. To determine the SOH, the capacity is measured and compared to the initial capacity under identical conditions or the manufacturer rating [2], as given by equation (2.3)

$$SOH(t) = \frac{Q_{\max}(t) - \rho(Q_{rated})}{Q_{rated} - \rho(Q_{rated})} \tag{2.3}$$

Where ρ is a number from 0 to 1 describing the failure threshold of the battery, describing the reduction of available charge compared to rated capacity. For safety reasons, this is typically limited to 0.8. The importance of implementing such a limited is further elaborated in chapter 2.9

2.2. Lead Acid Batteries

2.2.1. General

Lead – acid based batteries are currently dominating the market for independent electrical systems [3]. The technology has existed for over 100 years and has yet to experience a revolutionary technological advance since it was first discovered. In the current market there are two fundamental categories of lead – acid batteries; flooded and valve – regulated lead acid batteries, or VRLA.

2.2.2. Mode of Operation

When the battery is fully charged there is a difference in the electric potential between the electrodes of 2V. During discharge, current is transferred through an external load while the chemical reaction between the electrolyte and the electrodes works to balance the battery. Figure 2-2 shows the chemical state of the battery when it is fully charged and fully discharged.

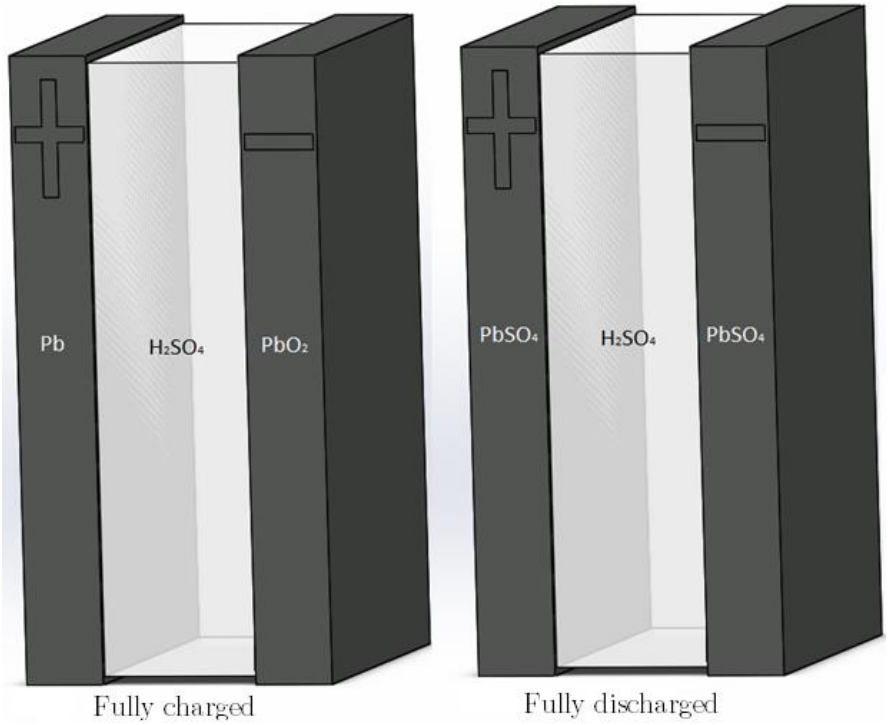

Figure 2-2: Chemical state of lead acid battery fully charged / discharged.

The internal chemical process is identical for the two fundamental types of lead – acid batteries, but their applications vary due to restrictions in system integration. VRLA batteries pose the advantage of not being subjected strict system requirements, like flooded batteries are. The flooded battery requires strict orientation relative to the gravitational force as the electrolyte can leak. VRLA

batteries are closed off and can be freely oriented. Since gas is developed and released to the surrounding during discharge of flooded batteries a properly ventilated environment is necessary. Requirements are less strict for VRLA batteries. Also maintenance of the electrolyte is substantially reduced for the VRLAs.

2.2.3. Specifications

The specifications given in Table 2-2 are based on data from [3], [4], [5] and [6].

	Flooded	VRLA
Energy density [Wh/l]	80	100
Specific Energy [Wh/kg]	30	40
Maintenance	Yes	No
Investment cost [($/kWh]	65	120
Cyclic lifespan	> 1200 (50% DOD) > 300 (100% DOD)	> 1000 (50% DOD) > 200 (100% DOD)
Temperature-sensitivity	> 25 °C	> 25 °C
Efficiency [%]	100% @ 1/20 C 80% @ $\frac{1}{4}$ C 60% @ 1 C	00% @ 1/20 C 80% @ $\frac{1}{4}$ C 60% @ 1 C
Internal impedance	< 25 mΩ	> 25 mΩ

Table 2-2: Specifications of lead acid battery technology

2.2.4.Summary

Pros and cons for lead acid batteries in automotive applications are summed up in Table 2-3.

Advantages	Disadvantages
Cheap	Low energy density
Handles abuse very well	Low spesific energy
	Poor life – span
	Elevated self discharge rate
	Elevated internal impedance
	Low efficiency
	Chemical memory

Table 2-3: Summary of lead – acid characteristics

2.3. Nickel – based batteries: NiMH and NiCd

According to [4], nickel – metal hydrate batteries, NiMH, were the dominating technology for energy storage in electrical hybrid vehicles in 2011. The article also points out that the technology has a bright future in energy storage in smart grids and stationary emergency energy supply.

The first NiCd – batteries were developed as early as 1899 and the technology was improving until the late 1990's. They are particularly rigid and can withstand abuse better than any of the other technologies attended to in this thesis work.

2.3.1.Mode of Operation

The positive electrode of the NiCd - battery is constructed from nickel oxide (Ni_2O_3), while the negative electrode is of cadmium. Between the electrodes there is a separator and an alkaline electrolyte. Around these components there is a metal sheath with an incorporated safety valve. During discharge, cadmium is oxidized at the anode and nickel reduced at the cathode. This is shown in equation (2.4) and(2.5).

$$Cd + 2OH^- \rightarrow Cd(OH)_2 + 2e^- \quad (2.4)$$

$$2NiO(OH) + 2H_2O + 2e^- \rightarrow 2Ni(OH)_2 + 2OH^- \quad (2.5)$$

The principle and structure of the NiMH – cell is identical to the NiCd – cell, but the difference is that the nickel –metal hydride battery uses hydrogen, absorbed in a metal alloy for the active negative material in place of the cadmium used in NiCd batteries [1]. The change of positive electrode material allows the NiMH to store more energy per weight and volume, and in many ways make the nickel – cadmium battery superfluous.

2.3.2.Specifications

The values listed in Table 2-4 are based on data obtained from [7], [8] and [9].

	Ni/MH	NiCd
Energy-density [Wh/L]	< 160	< 150
Specific energy [Wh/kg]	< 80	< 60
Specific power [W/kg]	< 1000	< 150
Maintenance	No	No
Invest cost [$/kWh]	Approx. 364 Approx. 702	Aprox. 533
Antall ladesykluser	< 1000 @ 50% DOD	> 2000 @ 50% DOD
Temperatur-sensitivitet	Ja	Nei
Virkningsgrad	< 80-95%	< 84 % @0.1C
Internal Resistance		> 17 m mΩ

Table 2-4: Specifications of nickel – based batteries.

2.3.3.Summary

Data from chapter 2.3 is summarized as advantages and disadvantages of the nickel – based batteries

NiMH		NiCd	
Advantages	Disadvantages	Advantages	Disadvantages
Elevated energy density and specific energy	Limited life – span	Permits rapid charging	Low spesific energy
Possible to recycle	Does not handle elevated charging currents	Good cyclic lifespan	Chemical memory, needs full charge and discharge cycles.
Reduced chemical memory.	Elevated self - discharge	Rigid, handles abuse very well	Environmentally unfriendly due to use of cadmium
	High production of heat when subjected to elevated charging / Discharging currents	Elevated shelf life rates and low natural degradation over time	Elevated self discharge rates.
		Low cost	

Table 2-5: Summary of nickel-based battery technology.

2.4. Super – Capacitor

As opposed to the energy storage technologies reviewed, the super - capacitor, or ultra – capacitor has only emerged onto the market in recent years. In line with the rapid technology development, Maxwell Technologies has now released a new series of automotive super - capacitors to operate in cooperation with lithium batteries in hybrid and full electric vehicles.

2.4.1. Mode of Operation

An electrochemical capacitor, or super – capacitor, is based on two electrodes separated by a permeable iron – membrane and an electrolyte to ensure electrical

contact between the electrodes. When voltage is applied over the electrodes, an electric double-layer is formed, with positive or negative ions deposited in a mirror image on the each electrode [10].

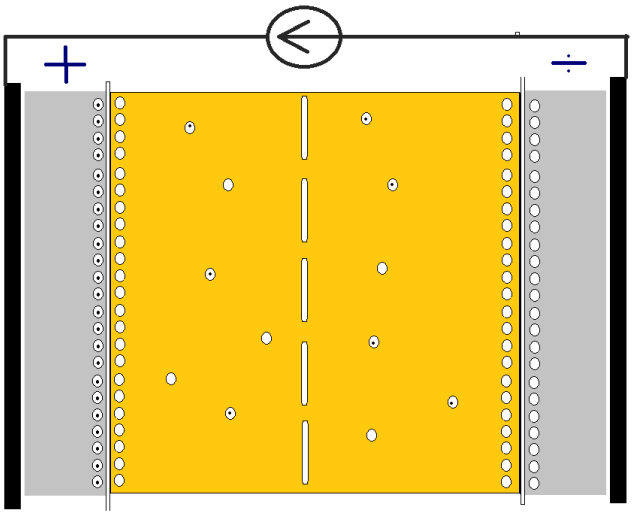

Figure 2-3: Description of double layer super-capacitor.

2.4.2. Specifications

Performance specifications in Table 2-6 are based on data from [9], [10] and actual capacitors from the Maxwell Technologies portfolio [11].

	Super - Capacitor
Energy-density [Wh/L]	7
Specific energy [Wh/kg]	< 6
Specific power [W/kg]	< 7000
Maintenance	No
Investment cost [$/kWh]	2400
Lifespan [50 % DOD]	$> 1\ 000\ 000$
Temperature sensitivity	-40 – 65 °C
Efficiency	97 %
Internal Resistance	< 0.29 mΩ

Table 2-6: Specifications of performance data for the super-capacitor.

2.4.3.Summary

Advantages	Disadvantages
Superior specific power	Very low specific energy
Superior life span in terms of discharge cycles	Very low energy density
Low internal impedance	Expensive

Table 2-7: Summary of super capacitor advantages and disadvantages for automotive application

2.5. Lithium – Ion

2.5.1. General

The term lithium – batteries describe primary batteries wielding lithium connections or lithium metal as anode material. As previously discussed, a primary battery is not relevant for the automotive industry. However, lithium – ion batteries are secondary batteries where lithium ions are transferred between the anode and the cathode [12]. Research on lithium – ion batteries started already in the 1960's, but the real breakthrough came later in the 1990's. The most substantial driving forces behind the research have been the desire to improve energy storage for portable electronic devices. Corporations behind these are still dominating the research, but also military and automotive industries are stepping up their efforts.

There are many types of lithium-ion batteries, but they are all based on the same principles and mode of operation. Because of the flexibility in design, the superior energy density and specific energy, lithium – ion batteries are now dominating the battery – markets, and over 63% of the batteries sold in 2005 where lithium – based [13].

A common misconception regarding the difference between lithium ion and lithium ion – polymer batteries is that they are two different types of batteries on an electrochemical level. All chemical reactions releasing energy and the electrode materials are the same. The difference lies with the electrolyte. Whilst the lithium ion battery has a liquid electrolyte, the lithium ion polymer battery has a solid polymer electrolyte that permits construction of a smaller and lighter outer casing

for the battery. The major advantage of the polymer cells is the flexibility it gives with regards to design. They can be made extremely thin and thus facilitate assembly of the cells in stacks. The disadvantages are that they are less rigid and handle mechanical abuse worse than a lithium-ion cell with a metal casing.

2.5.2. Mode of operation

The electrochemical reaction in lithium – ion cell uses three active components: Negative electrode, positive electrodes and the electrolyte. Both electrodes allow ions to migrate both to and from. When the cell is discharged, the positive ions are extracted from the negative electrode, which is usually a graphite structure, and is then intercalated in the positive electrode [12]. If discharged, this process is reversed. During the intercalation, lithium ions are deposited in the lattice – structure of the lithium compound, or the anode – material, and during the extraction they are removed. This is visualized in Figure 2-4.

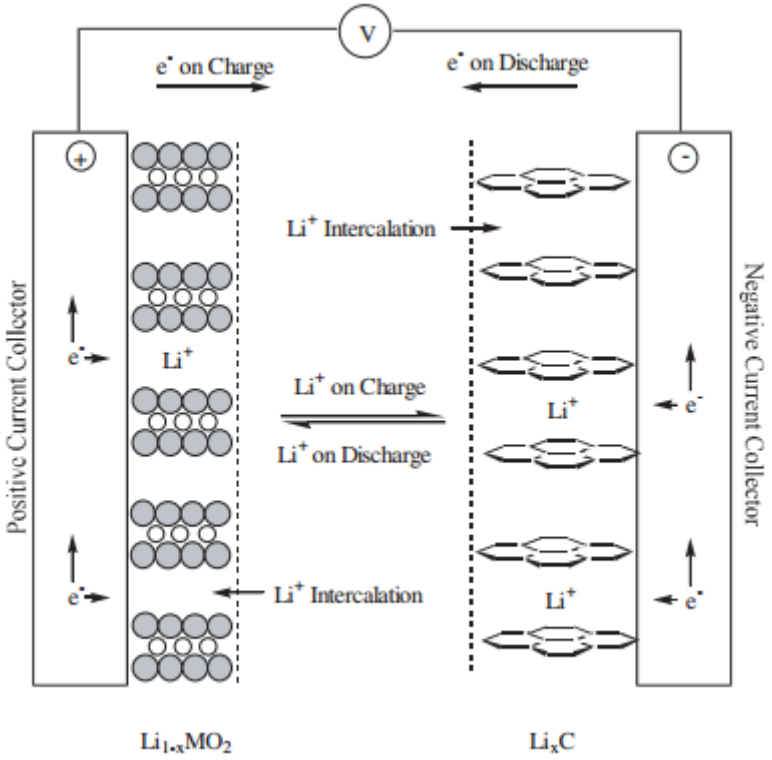

Figure 2-4: Schematic of the electrochemical process in a Li-ion cell. From [1].

If the cell's current carrying capability is exceeded, the lithium – structure is saturated and lithium – oxide is produced instead. The dangers connected to this reaction are attended to in 2.9.

Lithium salts like $LiPF_6$, $LiBF_4$ or $LiClO_4$ are often used as the electrolyte in lithium – ion batteries [1]. The battery's characteristics will vary significantly depending on the combination of positive and negative electrode- and electrolyte materials. Some combinations of active components could also give unwanted chemical reactions in the interface between electrolyte and electrode [13].

The majority of all available lithium – ion cells is designed with graphite as the anode material. Since the graphite anode holds such a low electrode potential it can be expected that the intercalated lithium – ions react immediately with the solvents in the electrolyte. However, during the formation process of the cell, when the cell accepts its first charge, a permanent passivizing layer is formed. This layer is referred to as the SEI – layer, or the solid electrolyte interface. This layer protects the lithium – ions in the negative electrode. The SEI – layer is resistant to the lithium – ions, but not to the electrolyte. It is therefore very important that the cell is built up around a stable electrolyte [12].

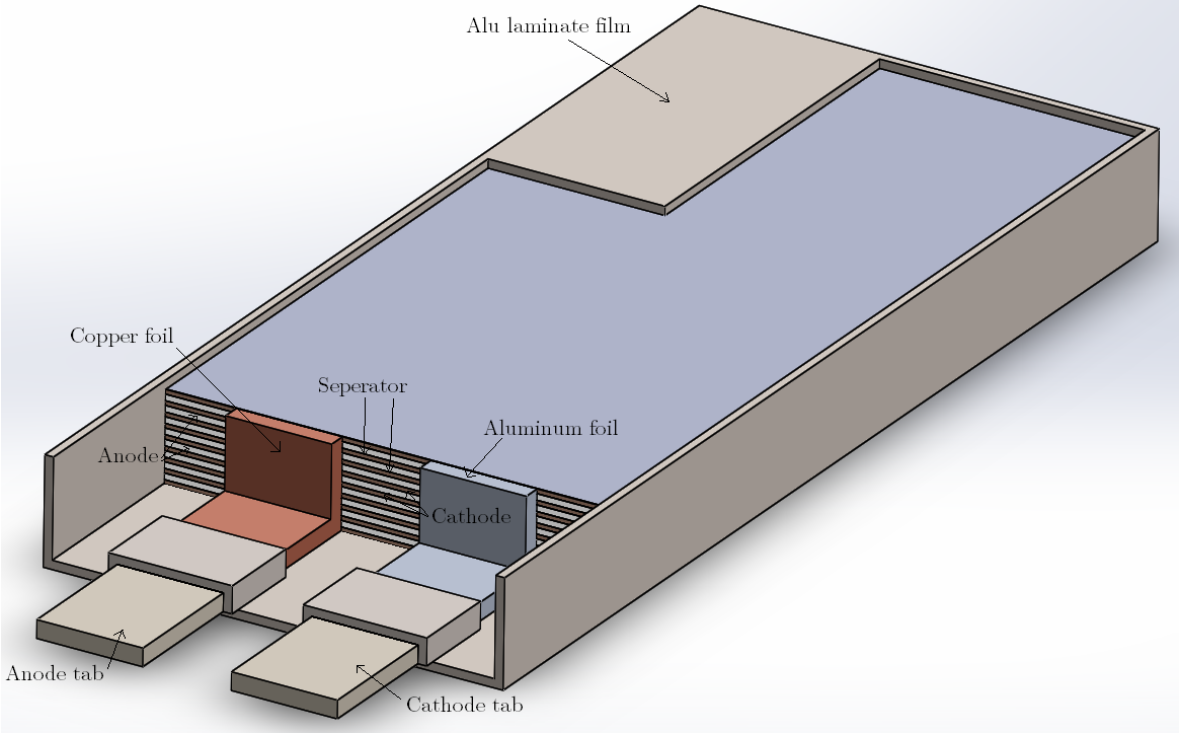

Figure 2-5: Construction of lithium – ion polymer battery overview

In addition to the SEI – layer, and the three active components mentioned above, the lithium – ion battery also contain insulators, or separators, current collectors and external parts like the cell cover / casing and poles for connection. As shown in Figure 2-5, the typical lithium – ion – polymer cell is constructed in layers, with the electrodes opposite one another, separated by the separator. The separator's

task is, as its name would suggest, physically separating the electrodes. Typical separator materials are polypropylene, or polyethylene, and the important qualities for a separator are electrical insulation, minimal electrolyte/ionic resistance, physical strength and chemical resistance.

2.5.3. Specifications

Data in Table 2-8 is gathered from [12], [14], [9] and from product portfolio of Panasonic [15], Dow Kokam [16], Samsung (appendix I), Melasta (appendix H), Valence [17], Gaia [18] and A123 systems [19].

	Lithium – Ion
Energy – density [Wh/L]	< 320
Spesific energy [Wh/kg]	< 265
Spesific power [W/kg]	< 3000
Maintenance	Nei
Investment cost [$/kWh]	500-600
Cyclic lifespan	> 2000 (100 %) > 3000 (80%) > 5000 (50%) >2000
Temperature sensitivity	< 60
Efficiency	< 92 % @ 1 C < 99% @ $\frac{1}{4}$ C
Internal Resistance mΩ	> 1-3 mΩ
Self-discharge	<5% per month

Table 2-8: Specifications of lithium – ion batteries.

2.5.4. Summary

The advantages and disadvantages of the lithium – ion batteries are summarized in Table 2-9.

Advantages	Disadvantages
Superior specific energy	Safety
Elevated specific power	Shelf life span
Design-flexibility	Elevated degradation rates when exposed to heat
Low self – discharge rates	Cost
Life span, cycles	

Table 2-9: Summary of lithium – Ion characteristics

2.6. Comparison of the relevant energy storage technologies

The data in Table 2-10 is visualized in Figure 2-6 and show why the automotive industry have turned their focus from lead – acid and nickel based batteries and intensified the investments in lithium battery research and development. Already the lithium – ion batteries are superior to nickel or lead based batteries in terms of weight and volume, life span and efficiency. The super – capacitor has outstanding specific power, efficiency and life span, but due to restrictions in energy storage they are unsuited as the lone storage method for automotive applications. However, the super – capacitor has complementary qualities to the lithium – ion batteries, and hybrid systems with the two are in development.

	Lithium	Super - capacitor	Ni/MH	NiCd	Lead Acid	
					VRLA	Flooded
Energy - density [Wh/L]	< 320	10	< 160	< 150	100	80
Specific energy [Wh/kg]	< 265	< 6	< 80	< 60	40	30
Specific power [W/kg]	< 3000	< 7000	< 1600	< 150	500	500
Investment cost [$/kWh]	< 500	< 2400	< 364	< 540	120	65
Life span, cycles	2000	> 1 000 000	< 1000	> 1200	200	> 1200
Internal impedance [mΩ]	< 0.2	< 0.29	< 30	> 17	> 25	> 25
Efficiency [%]	<96	97	<95	n/a	n/a	n/a
Self discharge [% / month]	<5	n/a	<15	n/a	n/a	n/a

Table 2-10: Comparison of the different energy storage technologies reviewed in chapter 2.

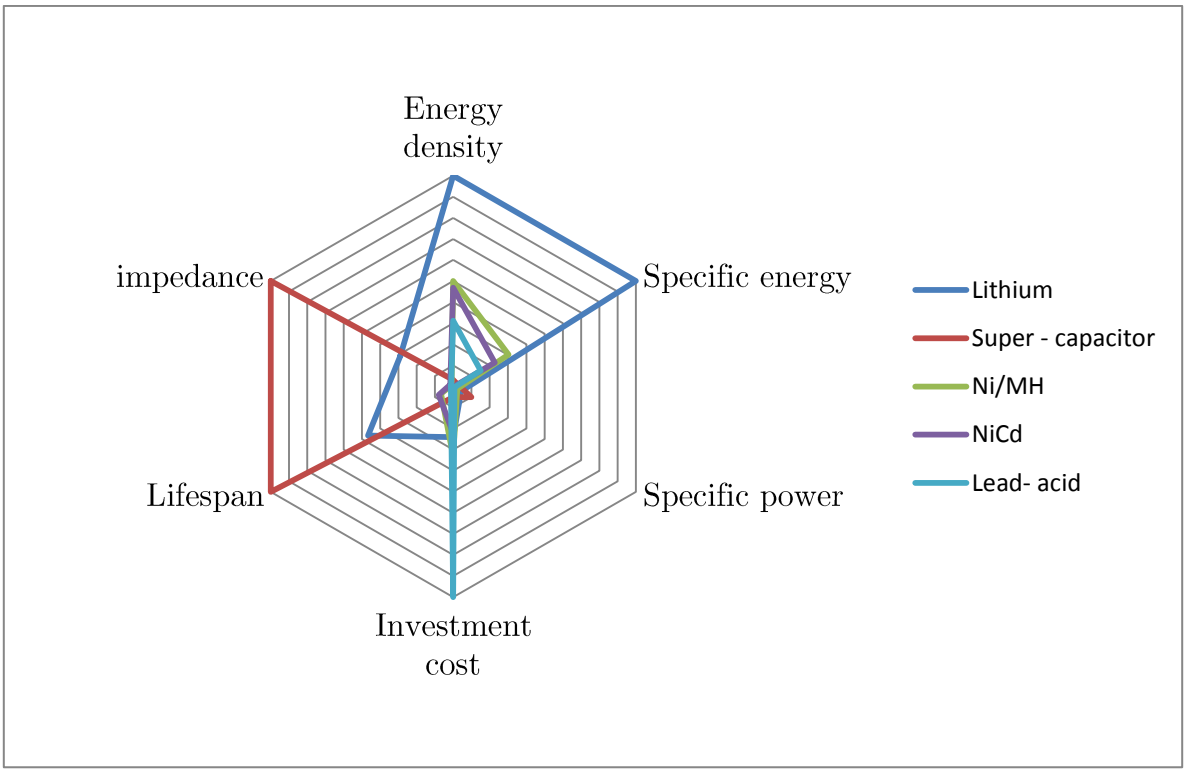

Figure 2-6: Comparison of different energy storage technologies for automotive application

2.7. Positive electrode – material for lithium – ion batteries

2.7.1. General

There are vast possibilities in combining different materials to design a battery with given specifications. Using different lithium compounds as the positive electrode material can give great flexibility in the design the battery for certain important parameters. Unfortunately, there is no choice that suits all applications, and using a material for high specific energy means that compromises have to be made on other important parameters. In example, a stationary power energy battery for a micro-grid will favor life-span and price whilst specific energy can be sacrificed. In a racecar, weight and volume is of the essence, whilst price and life – span can be on the other end of the compromise.

In the modern market, the more prominent materials available are lithium cobalt – based ($LiCoO_2$ / LCO), lithium iron – phosphorus ($LifePO_4$ / LFP), lithium manganese – oxides ($LiMn_2O_4$ / LMO), lithium cobalt aluminum ($LiNiCoAlO_2$ / NCA) and combinations of the above ($LiNiMnCoO_2$ / NMC).

2.7.2. $LiCoO_2$ – LCO

LCO batteries were the first of the battery – types attended to in this chapter to emerge into the market [1]. They are still typically used in cell phones and other portable electrical devices due to the elevated specific energy and energy density [14]. The first LCO batteries had poor current carrying capabilities both at charging and discharging, but these limitations have been drastically improved in recent years. Disadvantages of the modern LCO batteries are the relatively poor life – span and the instability when exposed to elevated temperatures. However, they present another grand advantage for voltage sensitive equipment as they hold a stable and elevated voltage – plateau during discharge compared to batteries designed with other positive electrode materials [1]. In operation, this means that a battery system built up from LCO batteries can maintain voltage and thus reduce current and in turn heat dissipation [1].

2.7.3. $LiMn_2O_4$ - LMO

The characteristic qualities of the cells designed with positive electrode based on manganese and cobalt are in many ways similar [20]. In example they also apply a high voltage plateau during discharge and elevated energy density and specific energy. The inclusion of manganese increase safety aspects, but life – span in terms of both cycle – life and shelf life is also poor [21]. The lowered stability in high – temperature environments is also a drawback for the LMO batteries.

2.7.4. $LiNiCoAlO_2$ – NCA

To better the safety aspects of LCO based cells researches developed cells with one or two added transitional metal – oxides on the positive electrode. One of the more prominent of these is the batteries with $LiNiCoAlO_2$, known as NCA. The batteries have lower voltage when fully charged, which make them more forgiving in case of overvoltage. Traditionally they also have better life – span both in terms of cycles and shelf life. These qualities make the batteries suitable for the automotive industry [22].

2.7.5. $LiNiMnCoO_2$ – NMC

The other nickel – based battery that has gained recognition is the NMC battery. They have been described as a hybrid between LMO and NCA. The inclusion of manganese ensures high energy density, but comes at the cost of an elevated self-discharge rate [12]. In later years, the NMC batteries have been gaining ground and are the favored choice for many high end application, among many being the chosen energy storage battery in the first ever full electric ferry constructed by Siemens AS.

The batteries also present elevated life – span and are beneficial in terms of weight and volume. Investment cost is elevated.

2.7.6. $LiFePO_4$ – LFP

To further increase safety and stability in lithium – ion batteries scientists chose to move away from the metal-oxide - electrode and look to materials based on phosphorus – compounds as the positive electrode material [22]. These compounds have stronger bonds than the oxides, which in turn reduces the amount of energy released in case of overcharge [22]. LFP – batteries have prolonged shelf life and exceptional cycle life. As the safest option, the LFP – technology also present poorer qualities in weight and volume.

2.7.7. Comparison of batteries with different positive electrode compounds

The numbers used in this section are based on numbers found in datasheet acquired from market – leading battery – producers. It has been attempted to find cells suitable for automotive applications for all different chemistries for proper comparison. From Table 2-11 it is evident that none of the battery cells achieve better specs on all points than all its competitors. This counts especially for specific energy and specific power which often comes at the expense of one another. This is due to many factors, the more prominent of which being the size of the current collector adjacent to the electrode.

Cell type and Producer	*Capacity [mAh]*	*Nom. voltage [V]*	*Energy-density [Wh/L]*	*Specific energy [Wh/kg]*	*Specific power (Cont.) [W/kg]*	*Number of cycles*	*Internal impedance [mΩ]*	*Charge Time [h]*
NMC – EIG (Pouch – 5C) [23]	20000	3,7	370,0	174,0	870,6	>95% = 1000	3	*2 - rec.*
NMC - Dow Kokam (Pouch – 5C) [16]	25000	3,7	286,2	154,0	770,8	>80% = 7000	1,2	n/a
LFP - A123 (Pouch – 18C) [19]	19600	3,3	247,0	131,0	2400,0	>90% = 3000	3	n/a
LFP - Valence (Cylindrical – 4C) [17]	2500	3,2	227,0	101,0	1012,7	>90% = 2000	n/a	0,25-max.
NCA - Gaia (cylindrical – 20C) [18]	7500	3,6	207,0	84,0	1687,5	>85% = 1000	1,2	0,25-max.
LCO - Panasonic (Pouch – 1C) [15]	3280	3,7	435,0	199,0	397,9	>85% = 500	n/a	n/a
LCO - Melasta (Pouch – 8C) (Appendix H)	7000	3,7	434,7	191,9	1534,8	>87% = 500	2	0,5 - max.
LMO - Samsung (Cylindrical - 1C) (Appendix I)	2850	3,7	150,5	216,7	216,7	>90% = 500	45	3 rec.
LMO - Hitachi (cylindrical – 11 C) [24]	4400	3,7	138,9	61,8	3000,0	n/a	1.5	n/a

Table 2-11: Comparison cell data from various manufacturers using different cathode materials.

The more suitable cells from Table 2-11 are visualized for comparison in Figure 2-7. Analyzing the comparison between the different cells it is evident that the cells are designed for special purposes and that compromises are made on certain qualities to accommodate for more energy, more power or better cycle – life. Samsung's cylindrical LMO cells have the highest specific energy, whilst energy density and specific power is severely reduced. Hitachi's 11 C cell based on the same material has outstanding specific power, but in terms of energy per weight it falls short. As the energy storage system for an electric car needs to carry substantial amounts of energy to increase range, handle elevated power – burst and offer good service life the versatile cells designed using NMC and LFP technology stand out as good options. For a prototype race - car application, cycle life can be compromised to accommodate for higher energy. Since the tests performed in this master thesis are focused on design for this niche market, the LCO and NMC cells are considered as very interesting options.

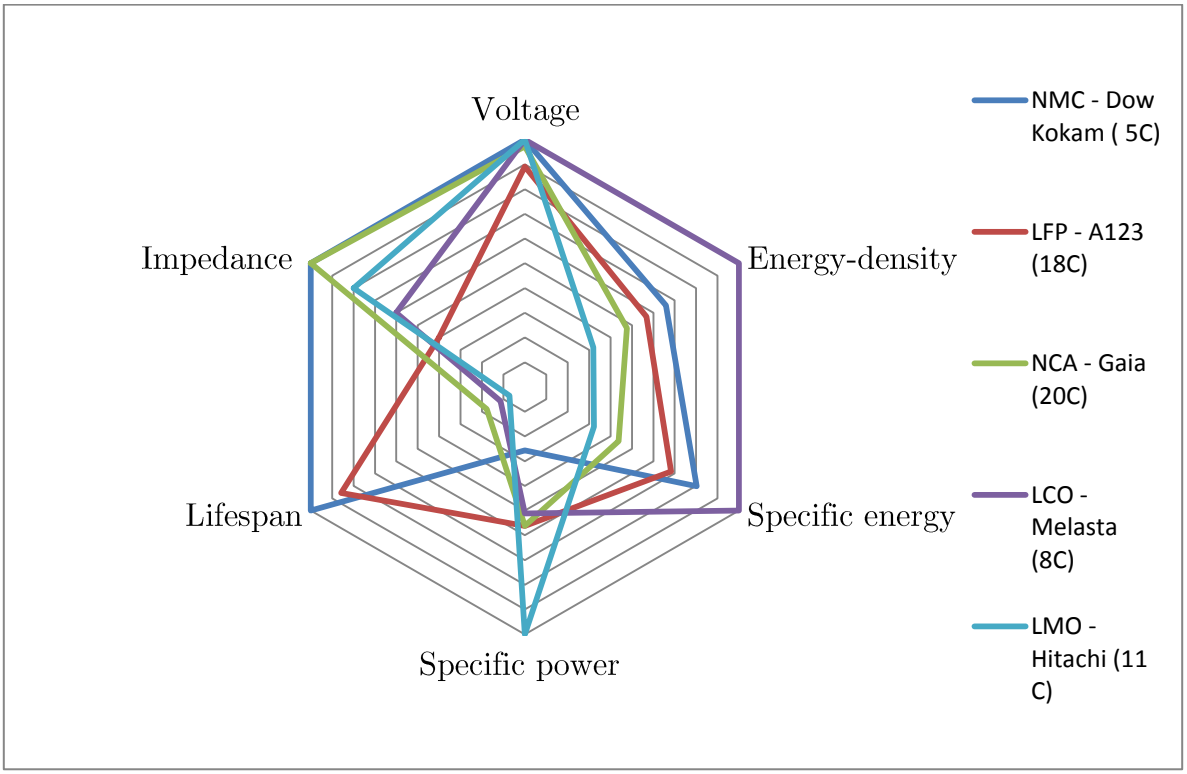

Figure 2-7: Visual comparison of the characteristics of example cells applying different cathode materials.

2.8. Anode materials for lithium – ion batteries

The majority of all commercial lithium – ion battery cells applies graphite as the base material for the anode. As mentioned in chapter 2.5, a SEI – layer is formed between the negative electrode and the electrolyte during the formation of the cell when it receives its first charge. This layer breaks down at about 110 degrees Celsius and starts an uncontrollable reaction between the electrolyte and the negative electrode. Depending on the thermal qualities of the battery and the positive electrode material the excess heat from this reaction can destabilize the positive electrode as well and cause a fire [22]. Lithium – titanium is a feasible alternative to the graphite anode. It operates at lower voltages, where the lithium ions are stable relative to the electrolyte. The SEI layer is never formed or needed, and the heating problem at the negative electrode is eliminated. Another grand advantage for the titanium – based batteries is their ability to accept charge, allowing rapid charging. Although cells with a titanium – based anode show successful performance results, they come at an elevated price and lowered specific energy [1], [20].

2.9. Safety aspects related to lithium - ion batteries

2.9.1. General

Safety is a general term used to describe the risk involved with use and storage of energy. The risk involves how well the battery handles abuse, the probability of unwanted situations arising and the consequence if such a situation should occur. Abuse implies overcharge, over - discharge, subjecting batteries to currents exceeding its capability, short circuiting and mechanical stress. In this section, the different aspects of safety for different types of lithium – ion batteries are discussed.

The more salient risk involving lithium – ion batteries is that the electrolyte is based on flammable organic compounds instead of water – based electrolytes like the other relevant batteries. This implies that the only external element the battery needs to catch on fire is heat energy. In other words, a lithium – ion battery fire is independent of its surroundings and cannot be put out in any other way than reducing temperature. The section is based on [20] and [25].

2.9.2. Overcharge

Overcharging a battery implies that a cell is charged at a voltage level superior to its designed specifications. If current is not stepped down to accommodate for the rising voltage at the end of charging, the voltage will continue to rise with the SOC. For the lithium metal-oxide based cells this means charging the cell to 4.2-4.3

V or higher, whilst for phosphorus – based lithium – cells, 3.8 V or higher. When subjected to overcharging there is a risk that the charged positive electrode reacts with the electrolyte, in turn developing gasses and pressure builds up within the cell. Modern lithium – cells should have an integrated safety valve to release the gasses and stabilize pressure to avoid a possible explosion. In that case, the extremely flammable gasses are ventilated to the surroundings, causing a hazardous situation. Some electrode – materials are more stable than others, and there are major differences to how the different cells respond to overcharge. However, no matter what electrode material is used, the battery will be broken if the valve is opened. Figure 2-8 show temperature – development caused by overcharge based on different compounds used as positive electrode – material. The tests performed in [25] interestingly enough show that some of the more thermally stable cells have the lowest tolerance for overcharge.

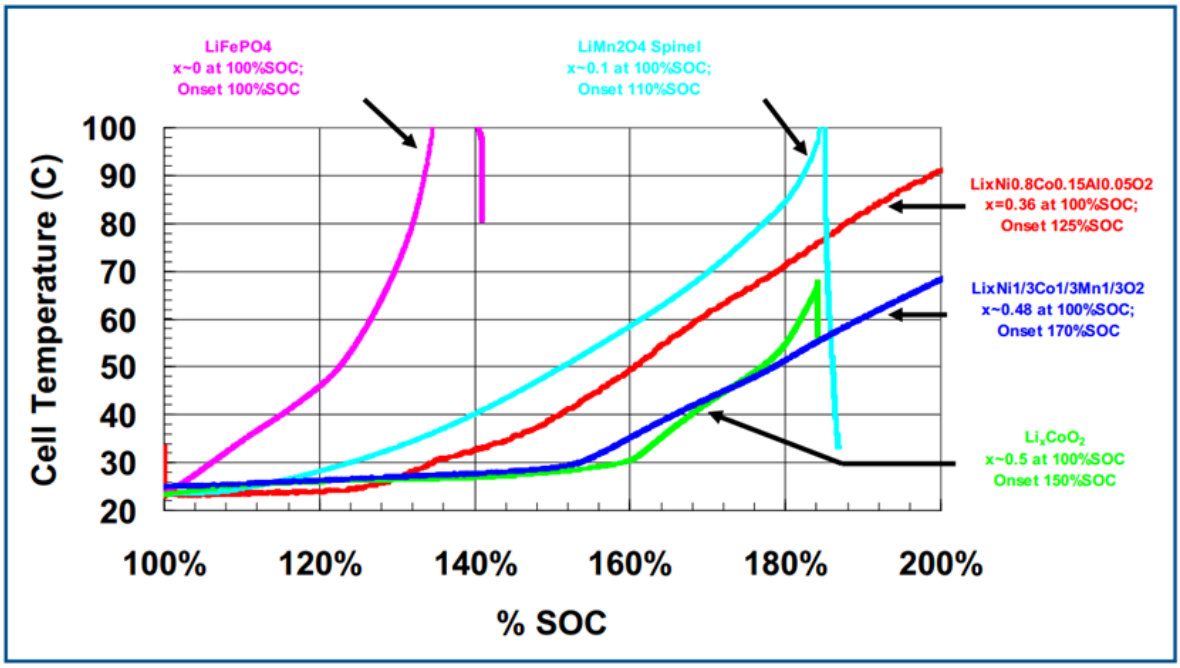

Figure 2-8: Heat output during overcharge for different cathode oxide chemistries. There is a noticeable output when final lithium is removed from the cathode. Figure is from [34].

2.9.3. Over – discharge

If lithium – ion cells are discharged to a voltage level below its rated state, i.e. < 3.0 V for a LCO cell, the metal in the current collectors, typically copper, can start to dissolve in the electrolyte. This leads to more free ions in the electrolyte and thus increases the conductivity of the electrolyte and in turn causes the self – discharge rate of the cell to increase. If charging is commenced after an undercharge situation has occurred, the ions can precipitate within the cell. Since

this reaction is not homogeneous, the metal can create a conductive bridge between electrodes and cause an internal short circuit. Therefore, a cell subjected to undercharge should be deposited and not reused [25].

2.9.4. Overcurrent

If a cell is subjected to a current exceeding its C-rate during discharge the cell is no longer able to accommodate lithium – ions fast enough between the intercalating layers in the electrode structure, potentially causing finely divided lithium – powder within the cell that may become electronically isolated from the anode [20]. This is known as lithium plating. Due to reduced amount of lithium ions in the electrolyte, an irreversible capacity – loss follows overcurrent. As with precipitated ions in the electrolyte, the lithium – powder can create dendrites growing from the anode through the separator, possibly causing an internal short circuit. These risks are present both at charging and discharging.

2.9.5. Operation at low temperature

The reaction rate of a chemical reaction varies with temperature. This phenomenon is known as Arrhenius law. At low temperatures, the conversion rate of the active chemicals within the cell decreases. This leads to a reduced ability to insert lithium ions in the intercalation layers of the cell, reducing the current carrying capability of the cell. At low temperatures, the risk is related to overcurrent situation as the limits for maximum charge or discharge current are lowered.

2.9.6. Operation at elevated temperatures

As with operation at low temperatures, the problems relative to elevated temperatures are traced back to Arrhenius' law. Reaction rates in the cell increase at elevated temperatures, causing more heat to be released from the reaction. Operating it high temperatures can lead to thermal runaway [25], where the cell spins out of thermal control through an increasing exothermal reaction.

2.9.7. Thermal stability

If the heat produced in the cell is not dissipated, the temperature will continue to rise due to sustained exothermic reactions [25]. The temperature rise in a battery cell is characterized in three stages; Stage 1 – onset, stage 2 – acceleration and stage 3 – thermal runaway. At stage two, the rapid heat release is a result of increased electrolyte reduction at the anode and the continuous breakdown of the SEI – layer. These reactions depend on the active materials and the state of charge. Additional heating causes the cell to enter stage 3, thermal runaway, which cause temperature to rise rapidly and flame or rapid disassembly may follow. The

runaway temperature is a function of cell size, cell design and materials in the cell, and thus varies from 130 °C to well over 200 °C.

In Doughty and Roth's discussion of lithium battery safety [25] several different tests are performed on various cells to study the thermal stability of cells designed with different positive electrode materials. Differential scanning calorimetry, Accelerating rate calorimetry and thermal ramp tests are used to study the behavior of the cells in stressed thermal situations. Only the test results are discussed here, not the methods.

LCO is the most reactive and has poorer thermal stability than the cells based on other positive electrode materials referred to in this thesis. Tests from [25] show that LCO has higher self-heating at elevated temperatures. $LiCoO_2$ decomposes at elevated temperature to produce oxygen that reacts exothermically with organic materials within the cell. Figure 2-9 shows that the onset temperature of the cells with other positive electrode materials is higher and that their maximum self – heating rates are lower.

All the metal-oxide batteries decompose and generate oxygen at some stage. The $LiFePO_4$ – cells do not, even when fully decomposed at high temperatures. The higher onset temperature of LFP and LMO show that they are more resistant to thermal abuse, and the reduced peak of self – heating make LFP –cells the safest in the lithium - ion market at present [25].

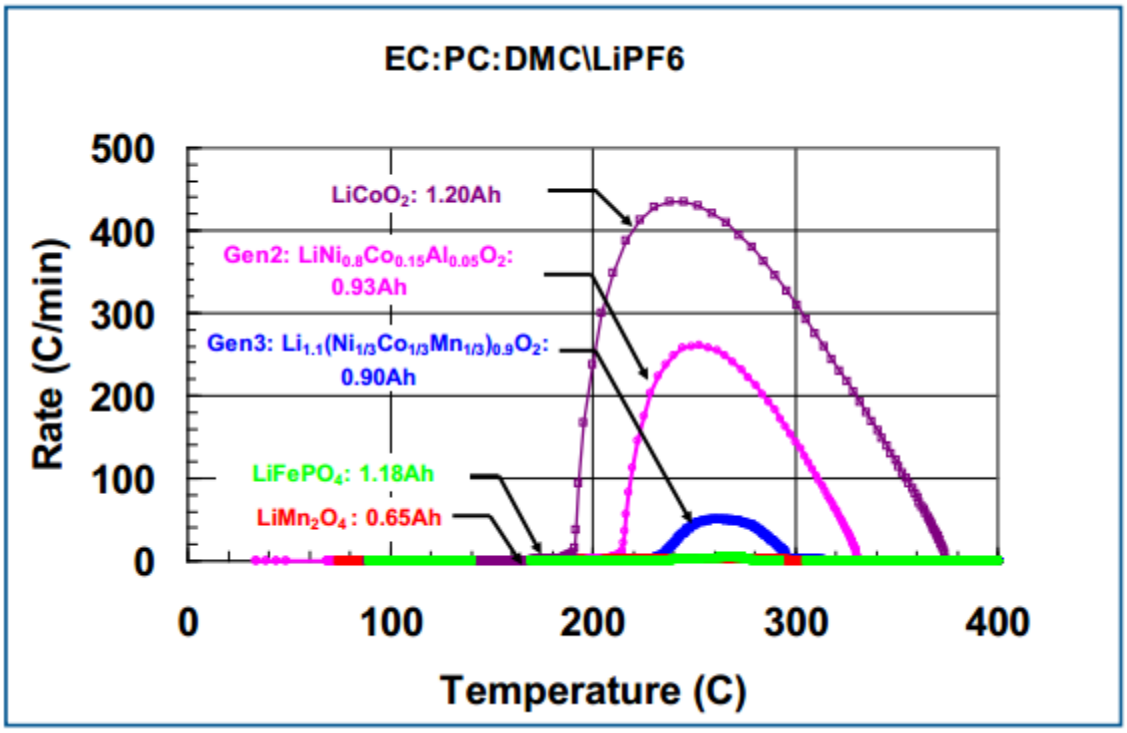

Figure 2-9: Self heating rate of cells measured by accelerated rate calometry. Improved cathode stability results in higher thermal runaway temperature and reduced peak heating rate [34]. The second axis shows the self-heating rate in degrees Celsius per minute.

2.10. Peukert's Law

Theory presented in this section is based on publications [26], [27]and [28].

Peukert's law, shown in equation(2.6), was presented by German scientist W. Peukert's in 1897 and expresses the capacity of a battery in terms of the rate at which it is discharged. As the discharge current increases, the available capacity in the battery decreases. Peukert's equation was developed for lead – acid batteries at constant discharge rates, but many scientists have attempted to adapt the equation to other battery types and variable discharge currents. However, these techniques have been shown to produce different and sometimes confusing results regarding state of charge of a battery.

$$C_{n1} = C_n \left(\frac{I_n}{I_{n1}}\right)^{pc-1} \tag{2.6}$$

C_{rated} and I_{rated} is the nominal capacity and current of the battery. C_{new} describes the actual capacity in Ah at given constant current rate I_{new}. A Peukert's coefficient of 1, for example, means that the available capacity is not dependent on

the discharge current rate. For lead acid batteries, the Peukert's coefficient is typically between 1.1 and 1.3. To calculate the Peukert's coefficient for a constant current discharge, equation (2.7) can be derived.

$$\ln(C_{new}) = \ln(C_{rated}(\frac{I_{rated}}{I_{new}}))(Pc-1)$$
$$Pc = \frac{\ln(C_{new}) - \ln(C_{rated})}{\ln(\frac{I_{rated}}{I_{new}})} - 1 \quad (2.7)$$

As presented in [28], one way to model Peukert's effect in lithium batteries when subjected to a variable current is to split the load into finite time elements and model the current for each time element as a constant current with an effective current as shown above.

$$I_{effective} = I(\frac{I}{I_{nominal}})^{pc-1}$$
$$C_{dch,effective} = \sum(I_{effective}\Delta t) \quad (2.8)$$

I is the actual current in the time-step, and I_{rated} is the nominal current for which the nominal capacity is given by the manufacturer. The effectively discharged capacity is then calculated by numerical integration of this effective current over time. The unused capacity after a full discharge at a high variable current can then be found by comparing the effective capacity to the nominal capacity, as shown in equation(2.9).

$$C_{remaining} = C_{nominal} - C_{dch,effective} \quad (2.9)$$

When applying Peukert's law to a lithium battery, the Arrhenius effect should also be taken into account as battery performance can increase significantly with temperature.

2.11.Cyclic lifespan of lithium – ion batteries

2.11.1. Introduction

During the life of a lithium cell, several physical phenomena contribute to degradation of the cells performance. The degradation mechanisms can cause internal resistance to increase, capacity fade and reduced ability to carry elevated currents. Extensive lithium plating or dissolved metal from the current collectors pose a danger of internal short – circuit in the battery. The degradation of a battery is most noticeably recognized in capacity decrease. Due to the risk of

internal short circuit and the unpredictability of the battery's behavior below a certain point, manufacturers advice users to dispose of the battery when it has degraded below a certain percentage of the initial capacity. Many manufacturers set this value to 80 %. Several aspects can alter the rate of degradation. There are still uncertainties surrounding the subject. The following sections are based on experimental tests performed on lithium – ion cells for EV industry.

2.11.2. Depth of discharge

For the telecommunications Energy Conference in 2006, IEEE authors T. Guena and P. Leblanc published a paper presenting an evaluation of how the depth of discharge affects cycle life of lithium polymer batteries [29]. The paper concludes that reducing the depth of discharge drastically increases the cycle life of lithium – ion- polymer batteries. Some of their important results are presented in Figure 2-10.

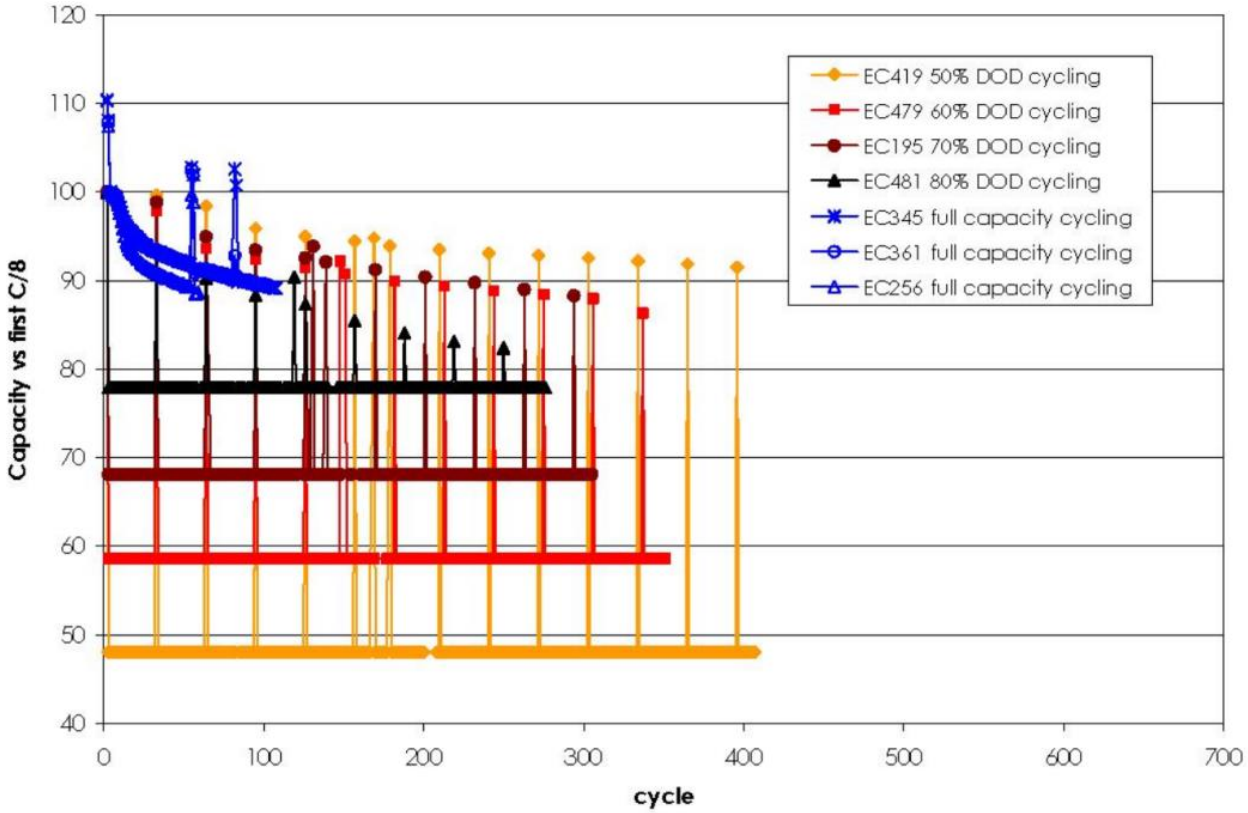

Figure 2-10: Capacity fade at various DOD for lithium batteries. From [29]. Tested lithium – ion polymer batteries are of the same capacity and chemistry.

By extrapolating the test results Guena and Leblanc (2009) also predict expected life time for the tested batteries at 50% - 100 % DOD. The results clearly support that reducing the DOD increases cycle life.

One way of recognizing that a battery is becoming unsafe to use, is by measuring the current efficiency of the battery.] [29] Also attends to the efficiency of the battery at different DOD for cyclic lifespan evaluation. Low efficiencies are usually associated with the formation of dendrites, which can become the limiting factor of the battery if they are not kept under control. Tests show that the current efficiency drastically decreases when cycling at elevated DOD. This corresponds to the capacity fade at similar conditions, as dendrites are formed from precipitated lithium ions in the electrolyte. Figure 2-11 show the current efficiency development during battery life when cycled at 60% compared to cycling over 100% of the rated capacity of the battery.

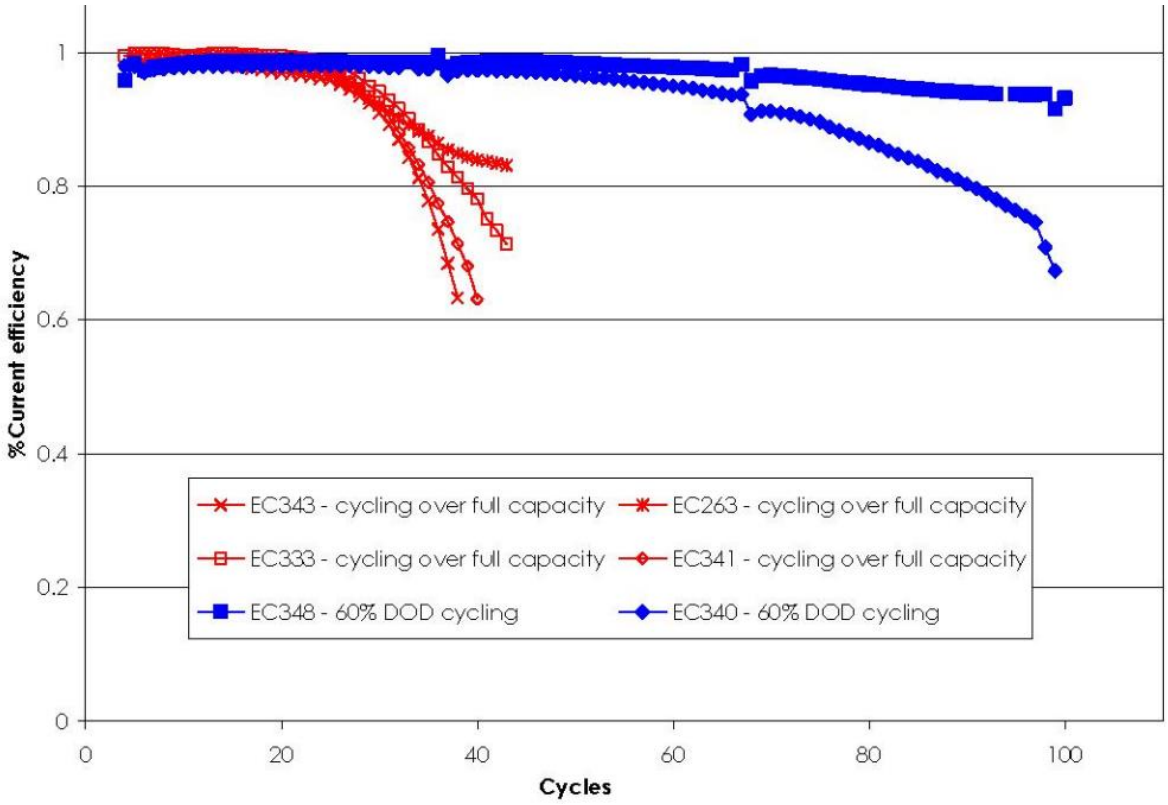

Figure 2-11: Tests results from [29] cycling batteries over full capacity and at 60% DOD.

The master thesis written by Jens Groot at Chalmers University, Sweden, focuses on battery cycle evaluation for hybrid busses [30]. Tests are separated into 5 different load situations, where three are based on hybrid (cycle A and B) or plug-in hybrid (cycle E) load situation over a relatively narrow SOC. The remaining two cells are subjected to constant current, one over a 17 % SOC region (cycle D) and the other a full DOD (cycle C). Results from the experimental work show that the

impact of the various ageing mechanisms is far more moderate at a narrow SOC region than when cycling the battery in a wider SOC region.

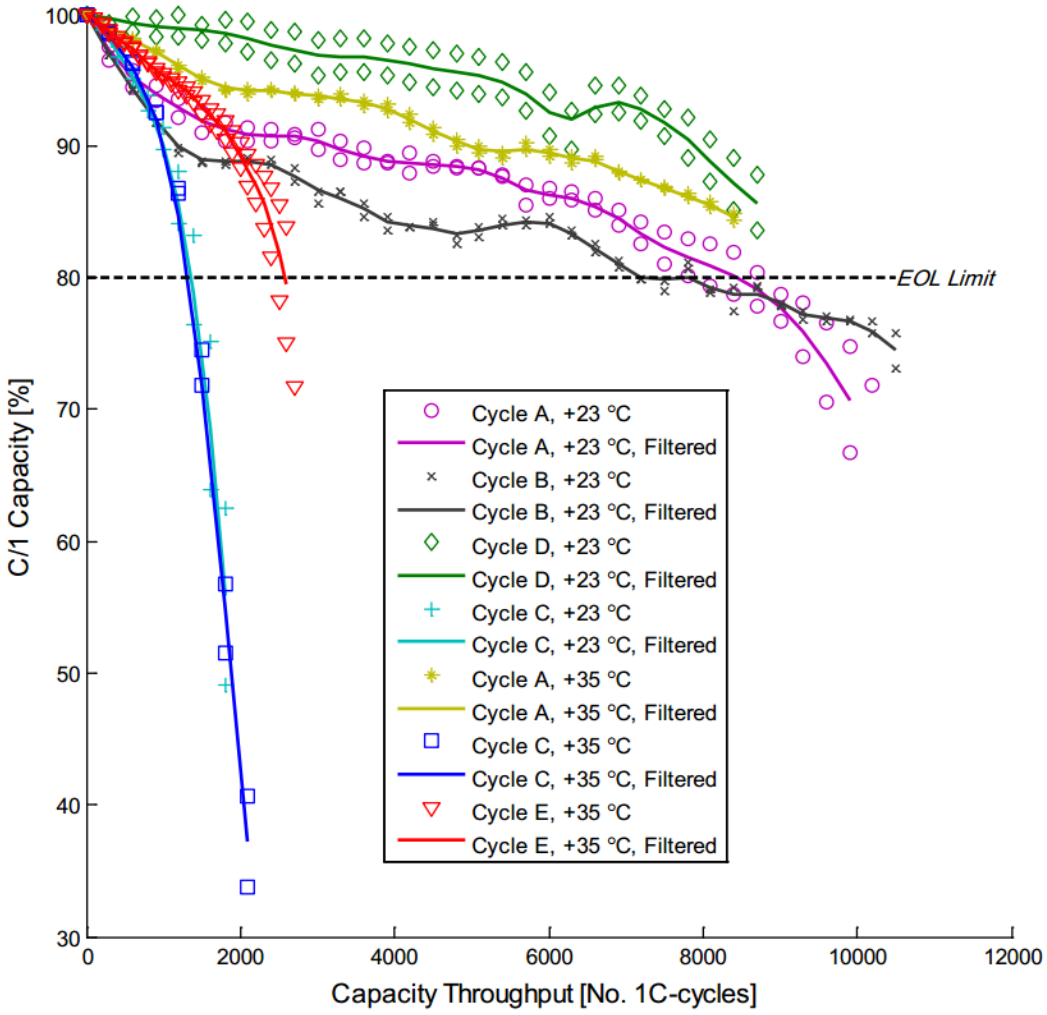

Figure 2-12: Cyclic lifespan during various discharge conditions. Cycle A and B are based on HEV load situation, cycle E on PHEV From [30].

2.11.3. Discharge current

From manufacturer performance data given for the specific cells used to design the tractive system accumulator for this master thesis, it is evident that discharge current is a crucial parameter to predict lithium battery cycle life. Figure 2-13 and Figure 2-14 show the manufacturer data for 100% DOD discharge at 1C and 8C, which is the cells maximum rating.

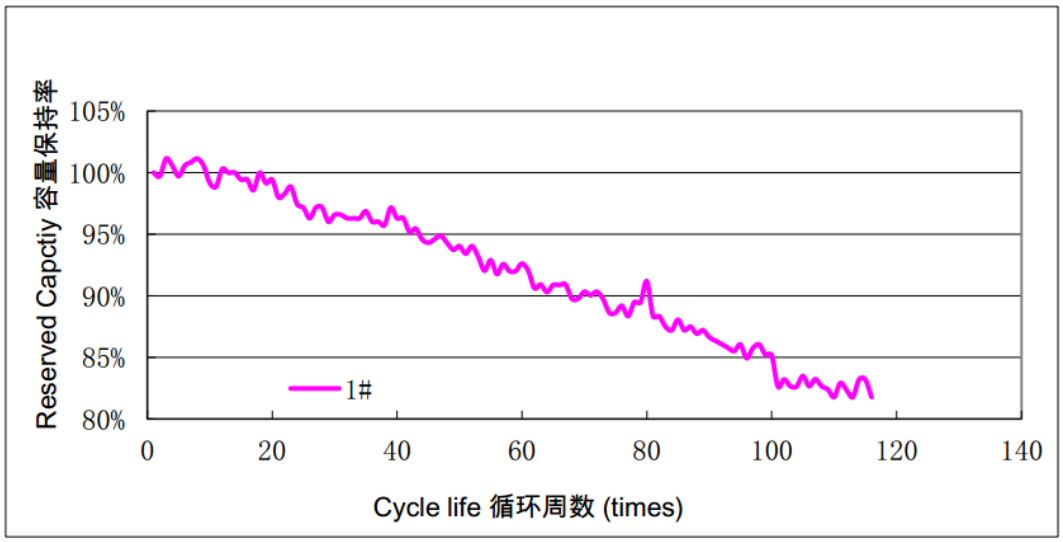

Figure 2-13: 8 C discharge, 100 DOD, charge to 4.2 V and 0.05 C current. Figure from performance data provided by manufacturer.

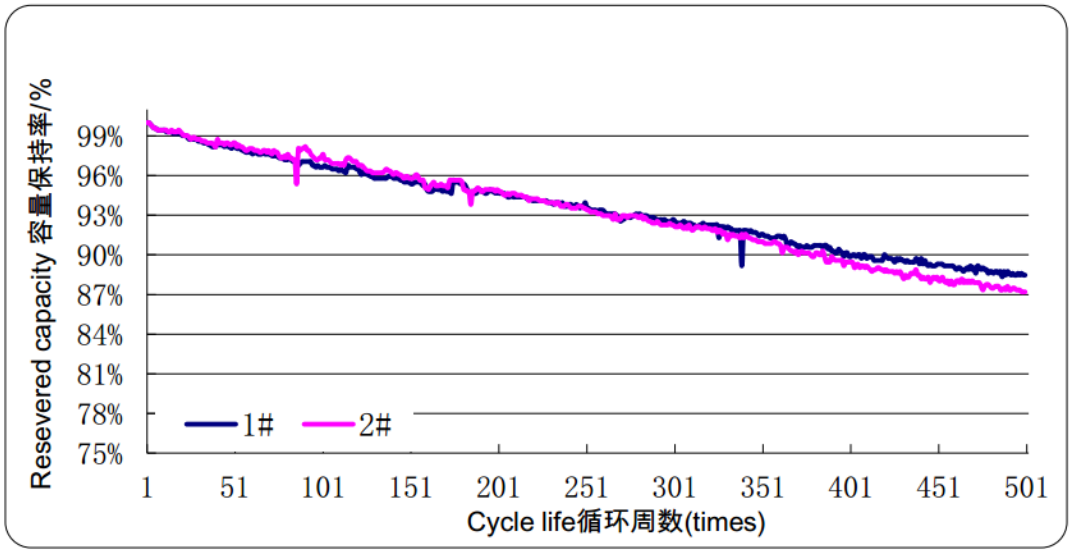

Figure 2-14: 1C discharge, 100% DOD. Charge to 4.2 V and 0.05 C current. Figure from performance data provided by manufacturer.

Experimental results from [2] indicate that alternating the discharge rates at very low discharge currents, here comparing 0.5 C to 1 C, only show a negligible deviation in battery cycle life.

Interestingly, tests using a pulsating load curve at 100 DOD jumping from 0.5 C to 1 C and 0 C gave better cycle life. Conclusions from the work indicate that this is because the battery is given a rest time in between discharging, allowing the

battery to remain closer to a stable electrochemical equilibrium [2]. A phenomenon to be closer examined later in this thesis report.

2.11.4. Charge current

As indicated by Saeed, Rayman and White [31], increasing charging current to reduce charging time might lead to accelerated capacity fade. According to their article, this is caused by the elevated stress during intercalation of lithium ion and the likely increase of charging temperature.

2.11.5. Temperature

Operating or storing lithium - ion batteries at elevated temperatures close to the temperature rating severely decreases both shelf life and cyclic life [32]. Data from [32] show that increasing the temperature from 35 °C to 50 °C mildly affects the degradation, whilst if further increasing temperature to 65 °C the degradation of the test cells accelerate exponentially.

According to test presented in [29], cells cycled at 35 degrees Celsius show slower deterioration than the equivalent cells tested with the same load curve at 23 degrees. Due to lack of proper ventilating equipment and temperature control, this will not be possible to examine during the master thesis work.

3. Accumulator management systems

3.1. General

The accumulator management system, AMS, is the brains of the system. They come in various shapes, sizes and with different functionality and capacity, but they all share the same main objectives: Control, supervise and calculate the crucial operating parameters of the battery system [33]. Most of the accumulator management systems also have implemented an interface with the operator to facilitate troubleshooting and monitoring, but as made clear by Karnjanapiboon [34] there also ex systems that do not use this communication. For an AMS used in an electrical vehicle, a user interface is absolutely crucial as the driver needs to know the state of charge of the batteries.

The system accepts measurements of temperature, voltage and current and uses these values to calculate i.e. the state of charge and state of health. This information is then transmitted to the user/operator. Depending of the topology of the system these measurements are done by using extensive wiring throughout the battery pack, in a centralized system, or by using microchips with integrated sensors and a master board, as in a distributed system. In the distributed system, as shown in Figure 3-1, each individual cell is monitored by its own cell board. This type of system is often more expensive, but is far easier to install and in most cases result in a more organized system. The cell boards responsible for measurements on the cells are called slave boards and communicate back to the master AMS through end boards. Such a system can be built up from several banks of any number of cells, where each banks is treated individually. Figure 3-1 show one such bank. The centralized systems communicate from a central unit using wiring for temperature and voltage sensors.

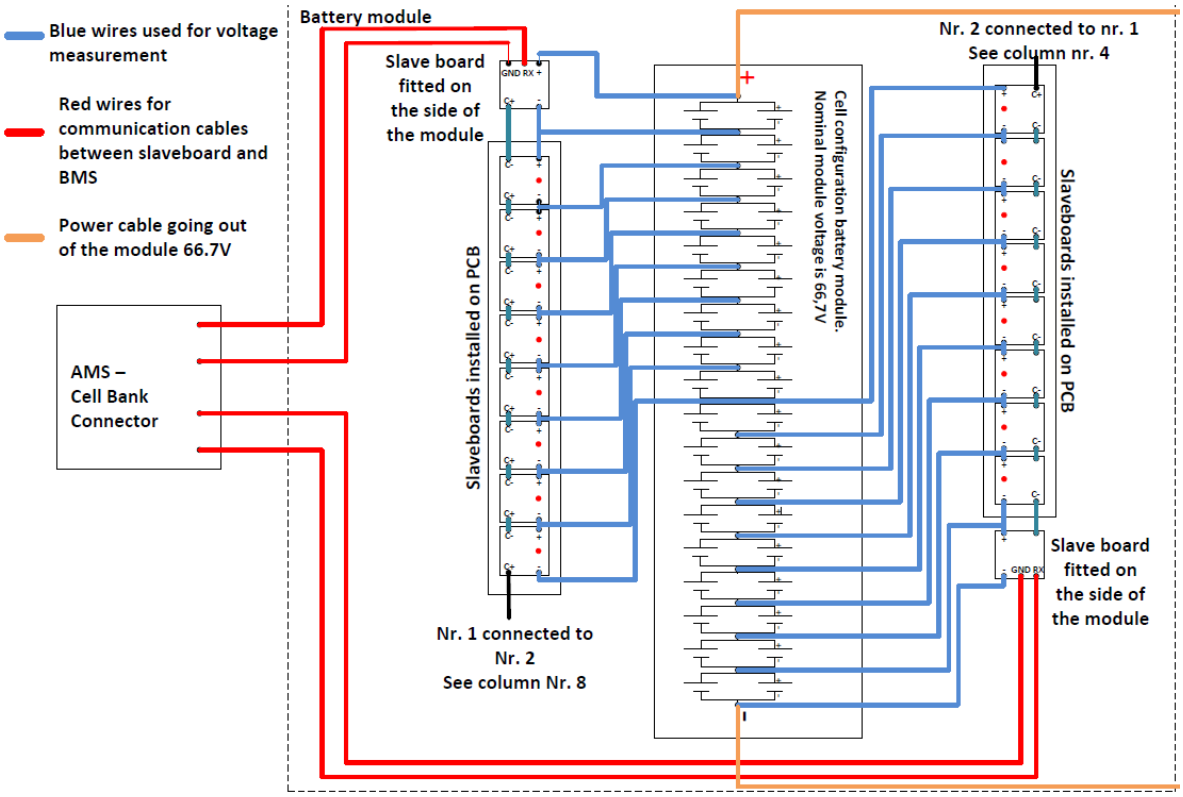

Figure 3-1: Distributed AMS configuration and cell connection.

The objective of the AMS functionality is first of all protecting the cells. When temperature, voltage or current exceed or fall under the critical values for the given cell the AMS needs to disconnect the load or source to stop charging or discharging of the cell. Some systems also implement extra safety by incorporating high and low limits close to the critical values to reduce current when the values are approaching the critical values.

In addition to its main objective, the AMS can be utilized to increase battery life-span [34]. Because of natural changes in the cells internal impedance or degradation due to use, the battery cells within a battery pack will not behave identically, especially in an older system, and voltages throughout the system will vary [35]. Since the AMS is programmed to disconnect the load / source when the weakest cell reaches the critical values, this will in turn lead to that the cells are discharged at different depths of discharge. Cell life-span in terms of cycles is highly dependent of the DOD and the weaker cell will degrade faster than the remaining cells, and cause the AMS to disconnect even faster at the next discharge. As the difference in SOC is proportional to the cell voltage, the remaining cells will still hold a certain amount of charge when disconnecting, drastically reducing the battery pack efficiency. To avoid this situation, the AMS should implement a cell balancing

function, ensuring that all cells have the same voltage. Cell balancing can be done by active balancing, passive balancing or by end of charge balancing.

3.2. Cell Balancing

3.2.1. End of charge balancing

This method of balancing is called charge shunting, and works through the control – system shunting the charging current around each cell as they become fully charged. The shunt resistor is carefully sized to shunt the charging current exactly when the fully charged cell voltage, V, is reached. If the charging current is reduced, the shunt resistor will discharge the cell. Therefore, the method can only be efficiently employed in system with known charge rates. Since lithium – ion battery cells have a very flat voltage plateau between 20%-80% SOC, this method also requires systems to fully charge the battery cells [35].

The disadvantages of this method are the requirements for large power dissipating resistors, high current switches and additional thermal management.

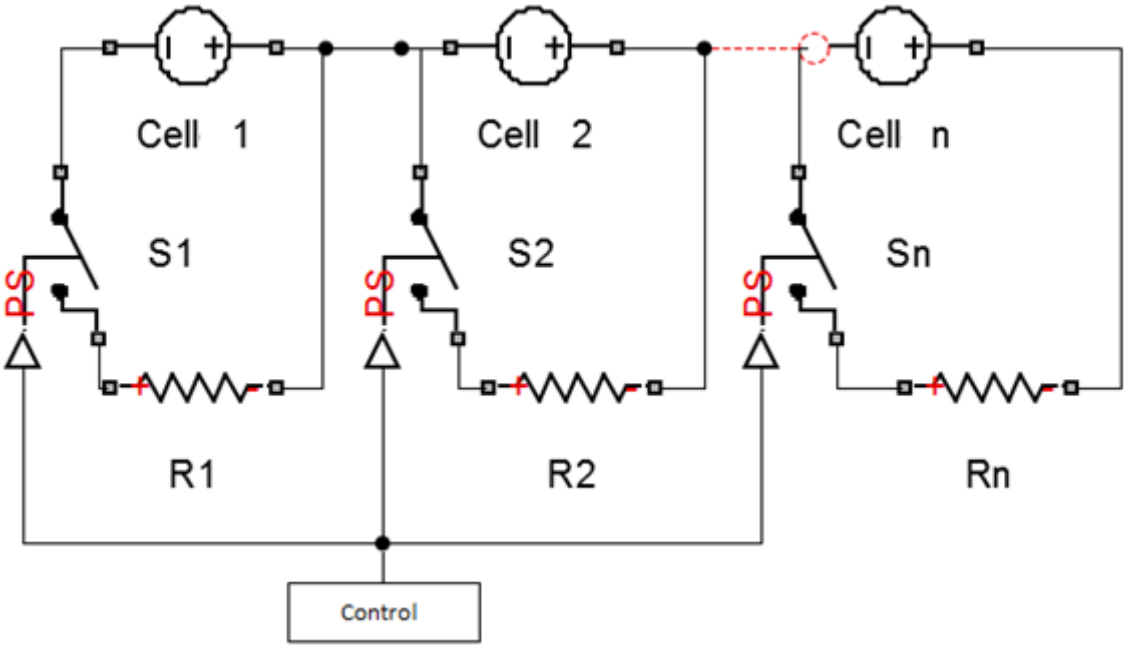

Figure 3-2: Schematic example of end of charge balancing using charge shunting.

3.2.2. Active Balancing

As opposed to the end of charge – method, active balancing is not based on dissipating, but rather moving charge from one cell to another. This is done by

either implementing an active charge – shuttling element or by employing voltage or current converters to move charge from one cell to another. The two major classifications of active cell balancing methods are charge shuttling and energy converting.

3.2.2.1. Charge shuttling

The method is also referred to as the flying capacitor charge shuttling method by Moore and Schneider [35]. By using capacitors to store the energy while the power electronics open and close selected switches to direct the flow of energy from and to the correct cells it is ensured that energy is moved from the cell with the highest voltage to the cell with the lowest voltage measured. This method requires an elevated amount of switches but reduces balancing time and losses during balancing.

As with end of charge shuttling, the method is not very efficient for batteries operating in mid – charge conditions. The larger variations in voltage occurs at "the knee" in each end of the voltage curve, over 80% or below 20%, and the balancing is far more efficient for cells being fully charged. Therefore charge shuttling balancing is more suitable for full EV application than HEV.

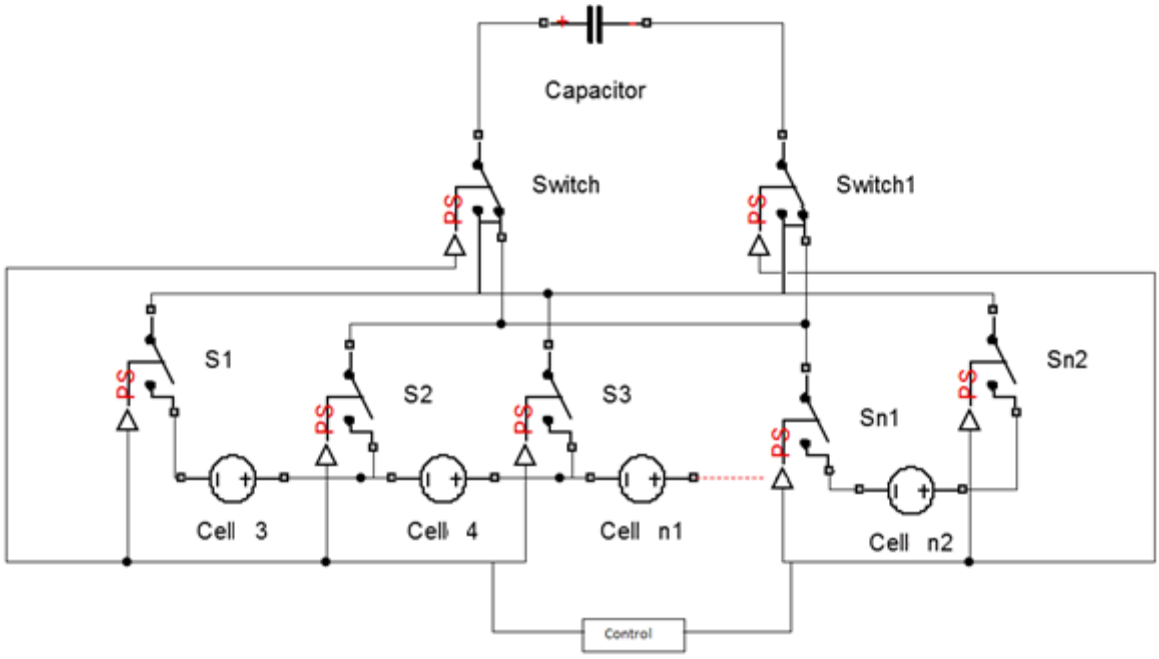

Figure 3-3: Schematic example of active balancing technique; charge shuttling.

3.2.2.2. Energy Converters

Cell balancing that utilizes inductors or transformers to move energy from a cell or a group of cells to another cell or group of cells [35]. The active cell balancing using

energy converters referred to in this section is the switched transformer method. It shares the same topology as the flying capacitor method, as shown in Figure 3-4. Current is taken from the entire stack of cells and switched into the transformer T. The transformer output is then rectified through a diode and delivered into the selected cell by the electronic control system opening and closing the switches.

The advantage of the method is that it can rapidly charge the weaker cells by removing energy from the entire pack. However, it is more complex and less efficient, due to switching and magnetic losses, than charge shuttling through a capacitor.

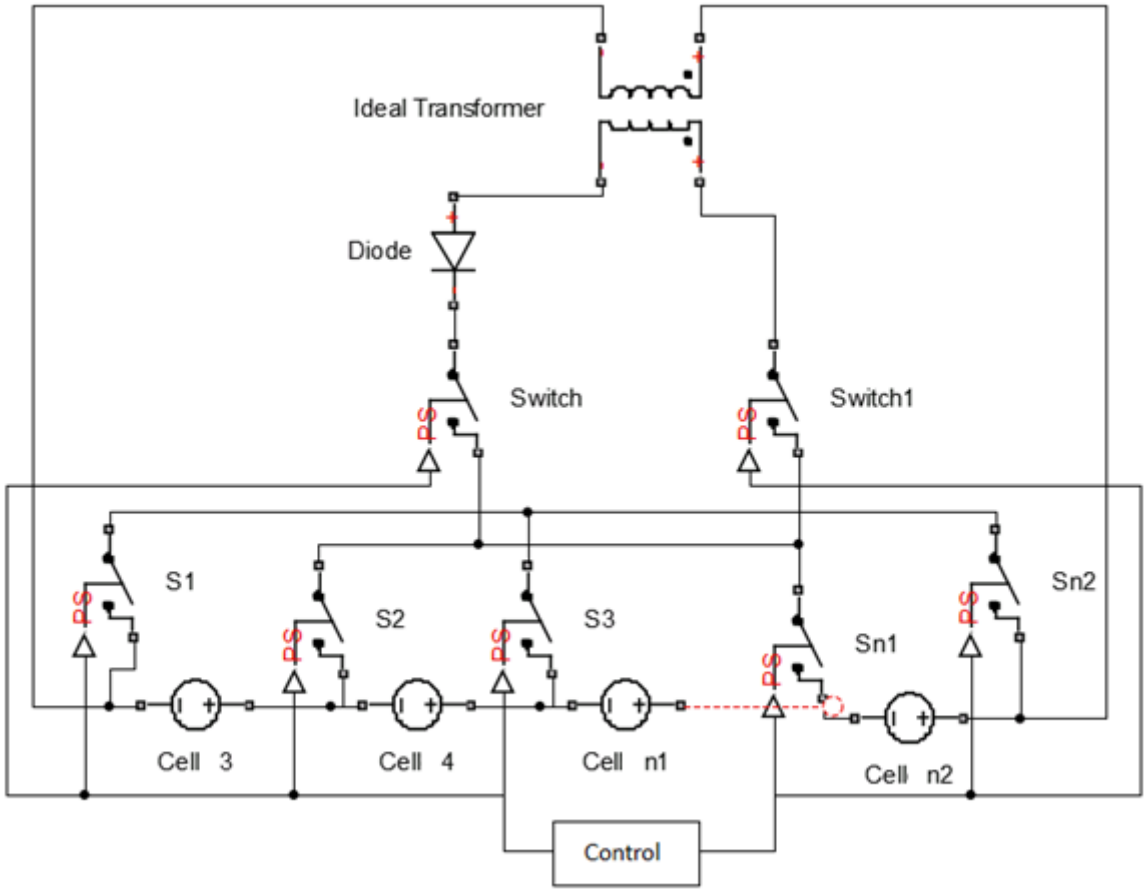

Figure 3-4: Charge shuttling active cell balancing

3.2.2.3. Passive balancing

Passive balancing is based on removing charge from cells with higher SOC through dissipation, instead of using the removed energy to charge the weaker cells. By shunting the selected cells with big resistors charge is removed from the cells until they match the voltage on the lowest cell. The topology of such a system is similar to the end of charge balancing technique, as seen in Figure 3-1, but can be

operated continuously. Passive balancing is the cheapest and easiest of the conventional cell balancing methods [35]. However, energy losses are superior when compared to the other methods featured here. The method is not dependent on larger voltage deviations between cells, and is thus more suitable for HEV application.

4. Design considerations

4.1. Introduction

When designing a battery for an electrical vehicle, there are many parameters to consider. The more important aspects of the system design that are attended to in this master thesis work is introduced in this chapter.

4.2. Cell choice for EV racing application

4.2.1. Battery capacity

To obtain the desired range for the vehicle it is necessary to estimate the battery capacity based on a realistic driving situation and system efficiency. Energy consumption of an electrical racecar is elevated compared to a normal EV, due to extremely steep speed profile requiring frequent acceleration. By obtaining a simulated load curve for a racing profile through the optimumLap software, Simulink has been used to approximate the needed capacity. This is further attended to in chapter 0.

Motor efficiency is given from motor supplier at varying torque and rpm. Based on this data, the losses in the motor can be approximated.

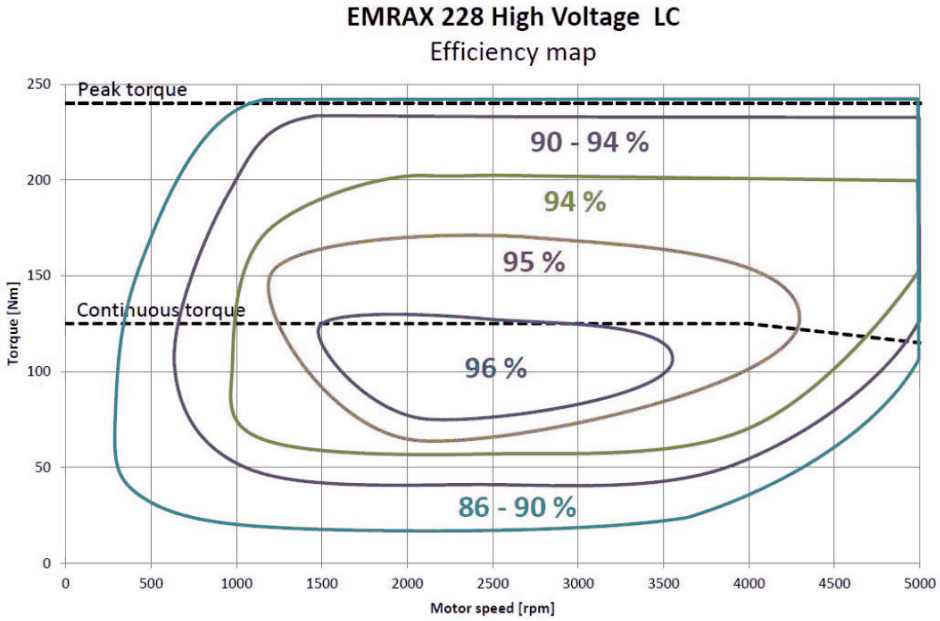

Figure 4-1: Efficiency map for the Emrax 228 motor from Enstroj. **[36]**.

4.2.2. Configuration

The configuration of the cells in a battery system is dependent on several factors. Size of the battery cells, motor and inverter rating and capability of removing heat from the electrical system are all important aspects. Heat generated in the electrical system is caused by the joule losses and are exponentially proportional to the current flowing through a conductor, as given in equation(4.1). Scaling up the cooling system leads to increased weight and volume either by using larger radiators for water – cooling or larger fans and LV – battery. It is therefore desirable to keep heating down without sacrificing power.

$$P = R \cdot i^2 \tag{4.1}$$

Employing a configuration with several parallel strings of cells reduces the current through each cell and also provides redundancy if one cell should fail or deteriorate faster than its counterparts. Cells that deteriorate will experience reduced concentration of free lithium – ions in the electrolyte and hence a rising internal impedance, as discussed in chapter 2.11. From conventional circuit theory it is known that more current will pass through the element with the lower resistance in a parallel connection. An increased impedance in one cell will cause a higher concentration of charge transferring through the healthier cells in the parallel – connection, reducing the burden on the already weaker cell.

The competition rules at FSAE events limit the voltage of the tractive system accumulator to 600 V. Combining the motor and inverter choice with the advantages of using parallel – connected elements and an increased system voltage, cells are connected with 144 series connected elements with 2 parallel cells. This configuration is typically referred to as 144S2P.

4.2.3. Current rating

Increasing the current carrying capability of a battery cell implies, among other factors, increasing the cross sectional area of the current collectors leading current from the electrodes to the battery tabs. These current collectors are typically aluminum for the positive electrode [47], while copper or nickel are typical materials for the negative electrode. The metals are heavy and implement extra weight to the cell design.

To keep cell weight at a minimum it is therefore desirable to dimension the cells for a realistic driving experience, ensuring that the cells do not overheat or deteriorate in normal use whilst avoiding adding extra weight through over dimensioning.

As discussed in chapter 2.11, the discharge current is an important parameter with regards to the battery cyclic lifespan.

4.2.4. Cell chemistry

For a prototype racecar, weight and volume is of the outmost importance. During the thesis work only two accumulators are built, allowing the team to check every cell thoroughly before and during installation. The safety terms is therefore demoted to the far end of the compromise when choosing battery technology and cell design. Cycle – life span and cost are other factors that can be sacrificed to achieve superior energy density and specific energy and power. As seen in Table 2-10 in chapter 2.6, lithium – ion batteries are considered the best solution when trying to meet the requirements posed by an electric racecar.

From the lithium – ion market analysis performed and presented in chapter 2.7, the NMC, LFP and LCO batteries stand out as good alternatives. Cells from suppliers EIG, Dow Kokam, A123 and Melasta were considered for the prototype racing accumulator system.

4.3. Electromagnetic interference

According to [37], the main source of electromagnetic interference in electrical vehicles is the power converter installed between the energy source and the motor. As the tractive system battery system is absolutely dependent on a flawless communication, the need for shielding the battery system from electromagnetic interference is evaluated. Shielding both AC and DC bus cables as well as communication – cables are obvious measures for reducing the impact of EMI. In addition, the possibility and effect of installing a faraday cage in the carbon – fiber molded battery casing to further shield the communications-system and the voltage sensing wires in the battery is discussed.

Designing an efficient system for EMI – shielding requires attention to several factors, most importantly the source of interference, the environment surrounding the source and the distance between the source and the receiver [38]. If the shielded circuit is operating in near field, the field characteristics are determined by the source, whilst if the circuit is operated in the far field, the field characteristics are determined by the transmission medium. The circuit is defined as in the "near – field", or induction – field, if it is operated within the distance of the interference wavelength divided by 2π, as shown in equation (4.1), where d is the distance from the source.

$$d = \frac{\lambda}{2\pi} \tag{4.2}$$

Conductive enclosures, like a faraday cage, can be used to shield sensitive circuits. The efficiency of the conductive shielding is dependent on the loss due to reflection of the interference wave, and the loss due to absorption of the wave within the conductive material. The reflection depends upon the type of interference, whilst the amount of absorption loss is not, and is the same for near – field and far field interference and electric or magnetic interference.

The loss of the magnetic interference wave due to reflection depends on the material, here described by its permeability, μ_r, in Henry per meter, the conductivity σ_r, given in Siemens per meter, and the frequency, f. Equation (4.3) describes the loss due to reflection [38].

$$R_m = 14.6 + 10\log_{10}[\frac{fr^2\sigma_r}{\mu_r}] \tag{4.3}$$

Here, r is the radius from the main source of interference. Equation (4.4) is obtained as the wave attenuation due to absorption [38].

$$A(dB) = 3.34t\sqrt{\sigma_r\mu_r f} \tag{4.4}$$

Parameter t is the thickness of the material.

Due to the skin effect, the reflection losses for plane waves in the far field decreases with increasing frequency, as opposed to the absorption losses, where losses increase with frequency because of the increased skin depth [38]. For high frequency interference signals high conductivity materials such as aluminum can provide adequate shielding, whilst at low frequencies both reflection and absorption losses to magnetic fields is low, making it hard to shield from low frequency magnetic interference. For this purpose, low reluctance materials provide the best shielding as they provide a magnetic shunt path that diverts the magnetic field away from the protected circuit.

Calculating the shielding efficiency of a circular hole in a conductive enclosure can be performed from equation (4.5).

$$S_{efficiency} = 20\log_{10}(\frac{\lambda}{2\cdot L}) \tag{4.5}$$

If additional shielding due to absorption is needed, a faraday cage can be designed and molded into the carbon – fiber structure of the battery casing. From equation (4.6) it is evident that shielding efficiency of a faraday cage increase with reduced diameter of the mesh. A rule of thumb for design of faraday cages is that mesh size

should be no larger than 1/20 of the wavelength of the interference. The wavelength can be found through equation 3.6, and the corresponding mesh size is found from equation 3.7.

$$W_{mesh} = \frac{\lambda_{interference}}{20}$$
$$\lambda_{interference} = \frac{C}{f_{interference}} \tag{4.6}$$

Giving

$$W_{mesh} = \frac{C}{20 \cdot f_{interference}} \tag{4.7}$$

C is the speed of the magnetic wave, assumed to be equal to the speed of light.

4.4. Safety systems

An electric vehicle is a potentially dangerous installation as it is exposed to a lot of mechanical stress that can lead to loose connections or damaged isolation. To minimize the risk of hazardous incidents, automated systems that will discover and act on faults at an early stage have to be implemented in the system design. The following safety measures are considered during the design process of the work.

- A tractive system master switch with a lock out tag function. It should not be possible to energize the tractive system when the switch is turned off.
- Three emergency shutdown buttons for manual shutdown of the tractive system. One placed in the cockpit, allowing the driver to shut down, and one on each side of the vehicle.
- Two high voltage relays that can isolate each accumulator pole from the tractive system.
- A series connected main fuse to protect the whole system against overcurrent.
- Insulation monitoring system to ensure good insulation between ground potential and the high voltage system.
- Accumulator management system, AMS, as elaborated in chapter 0.
- Brake over travel switch, BOTS, to shut down the tractive system if the specified brake pedal position is exceeded. If pressure drops in the brake system, brake over travel is possible and can thus indicate a leakage of brake fluid.
- Brake system plausibility device (BSPD), to sense if the brake and accelerator is enabled at the same time. If used for more than 500ms the tractive system should shut down.

- High voltage disconnects to isolate the accumulator from the remaining tractive system. Installed for redundancy in case of welded contacts in the AIRs.
- Inertia switch, or crash sensor, to isolate the shutdown circuit in case of a crash.

All these components should be incorporated in a system where a signal from any one of these components opens the accumulator isolation relays.

It is important that all components have insulation rated for the maximum system voltage and that components carrying tractive system current is dimensioned for load during the endurance race.

As with the battery system, weight and volume are crucial parameters in the prototype racecar in development. During the design process, focus is set at acquiring or producing the lightest and smallest components available, without compromising the functionality of the system.

4.5. Charging system

As the charging system is separated from the vehicle, the weight constraints are far more relaxed. Testing facilities made available for the team restricts charging at <4kW and therefore limiting the charger design and the charge time. Price is also of grand importance when designing the charging system.

To accommodate safe charging, the charger should be protected with a system interlock placed in the HV – string. A manual emergency shutdown button is also considered necessary. As the installed AMS already holds all the needed parameters for safe operation of the batteries, the charger modules should implement CAN communication between the charger and the AMS. In this manner, the AMS can signal the charger when the desired voltage is reached, so that the charger can reduce output current. This accommodates saturation charging as the current can be gradually reduced as maximum voltage is reached.

5. Design tools and simulations

5.1. Introduction

As the first step in the master thesis work, theoretical models are used to evaluate the various design considerations mentioned in chapter 0. In this chapter the models are explained and some of the results of the model work are presented.

5.2. Configuration of a load curve

Both to dimension the accumulator capacity and the system components and for running relevant tests on the batteries, an estimated worst case load curve is deemed necessary. By using OptimumLap software from OptimumG it is possible to obtain simulated load situations for configurable racing situation. The software is calibrated for a vehicle with similar parameters to the relevant racecar. OptimumLap output is based on optimal conditions and professional drivers, and the output has been confirmed by other users to be highly exaggerated. Because of this, the software is only used to obtain the profile of the load situation during one lap at a relevant track.

When the load – curve profile is acquired it is subjected to manual modifications based on data obtained from FSAE competition results. The results from the best electrical teams during the formula student competition in Hockenheim 2013 are given in Table 5-1. The average power found from these results is 16.34 kW. From equation (5.1) the efficiency score is calculated, where the amount of regenerated energy is approximated based on the drivetrain solutions published by the racing teams. Delft University are using NAV motors, allowing for a more efficient kinetic energy recovery system, and data show that they have regenerated approximately 1 kWh of energy during the endurance event.

$$S = P_{measured} - 0.9 \cdot P_{regenerated} \tag{5.1}$$

University	Time. [s]	Efficiency score [kWh]	Regenerated [kWh]	Total energy [Wh]	Avg. power [kW]
Delft	1367	5,071	1	6,971	18,36
ETH	1387	6,055	0,7	7,385	19,17
Hannover	1507	6,572	0,7	7,902	18,88
Amberg	1545	5,987	0,7	7,317	17,05
Dresden	1555	4,839	0,7	6,169	14,28
Zwickau	1559	3,885	0,7	5,215	12,04
Karlsruhe	1565	4,918	0,7	6,248	14,37

Table 5-1: FSAE 2013 endurance event results, used to estimate average power.

The load curve during one lap of 1.1 kilometers based on the curve topology of Hockenheimring extracted from OptimumLap software is visualized in Figure 5-1. The average power from this load curve is 44.7 kW, which is far superior to what is considered realistic based on previous results using similar cars. Since the load curve is to be used for capacity evaluation, battery cycle life and battery efficiency, making conservative approximations adds a safety margin to the design work. The load curve is manually modified whilst maintaining the load profile, to an average power of 26.9 kW and a peak power of 85 kW. The final load curve is shown in Figure 5-2.

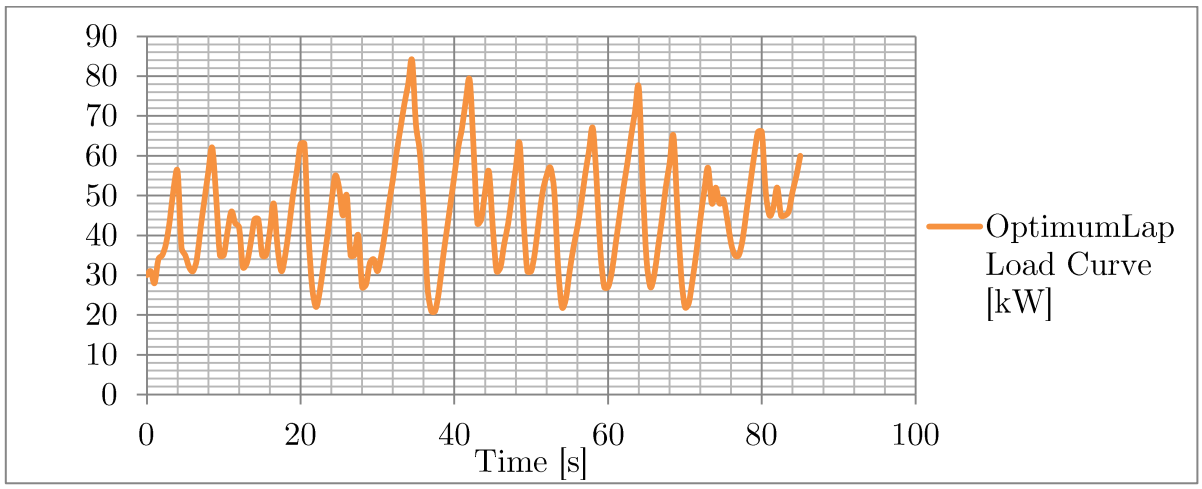

Figure 5-1: Load curve corresponding to one lap in Hockenheimring FSAE competition 2013, from OptimumLap software. Secondary axis is given in [kW]

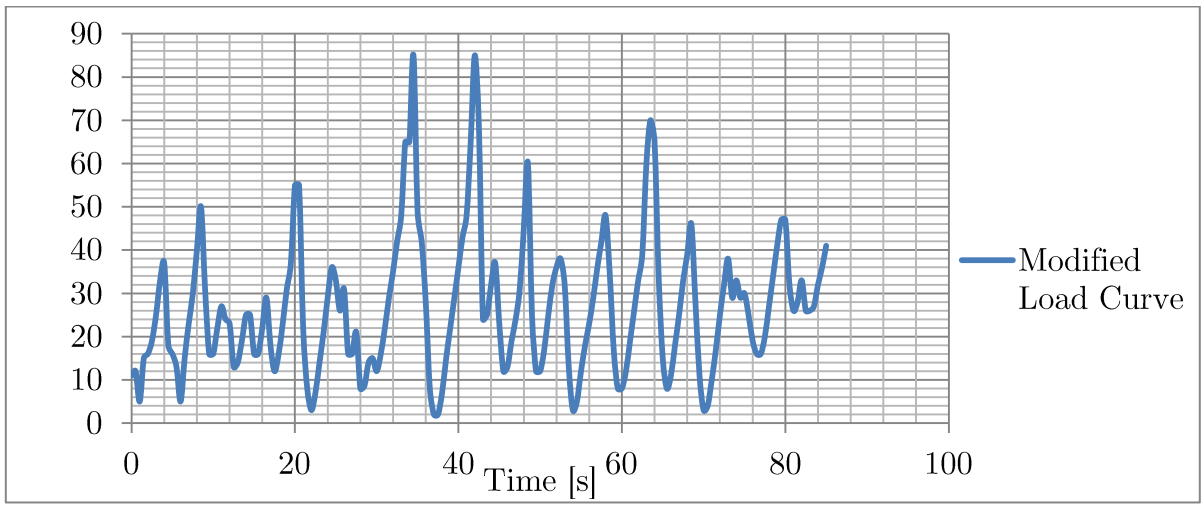

Figure 5-2: Manually modified load curve based on the profile from Figure 5-1 and the average power found from Table 5-1. Secondary axis is given in [kW].

5.3. Simulink

5.3.1. Introduction

Using Matlab program addition Simulink, a system model representing the battery behavior is utilized to evaluate battery performance in the tractive system. The load is represented by a controlled current source with reversed polarity compared to the lithium battery. This simplifies the model configuration and severely reduces computation time compared to using motor and inverter models, which is very time-consuming to correctly model.

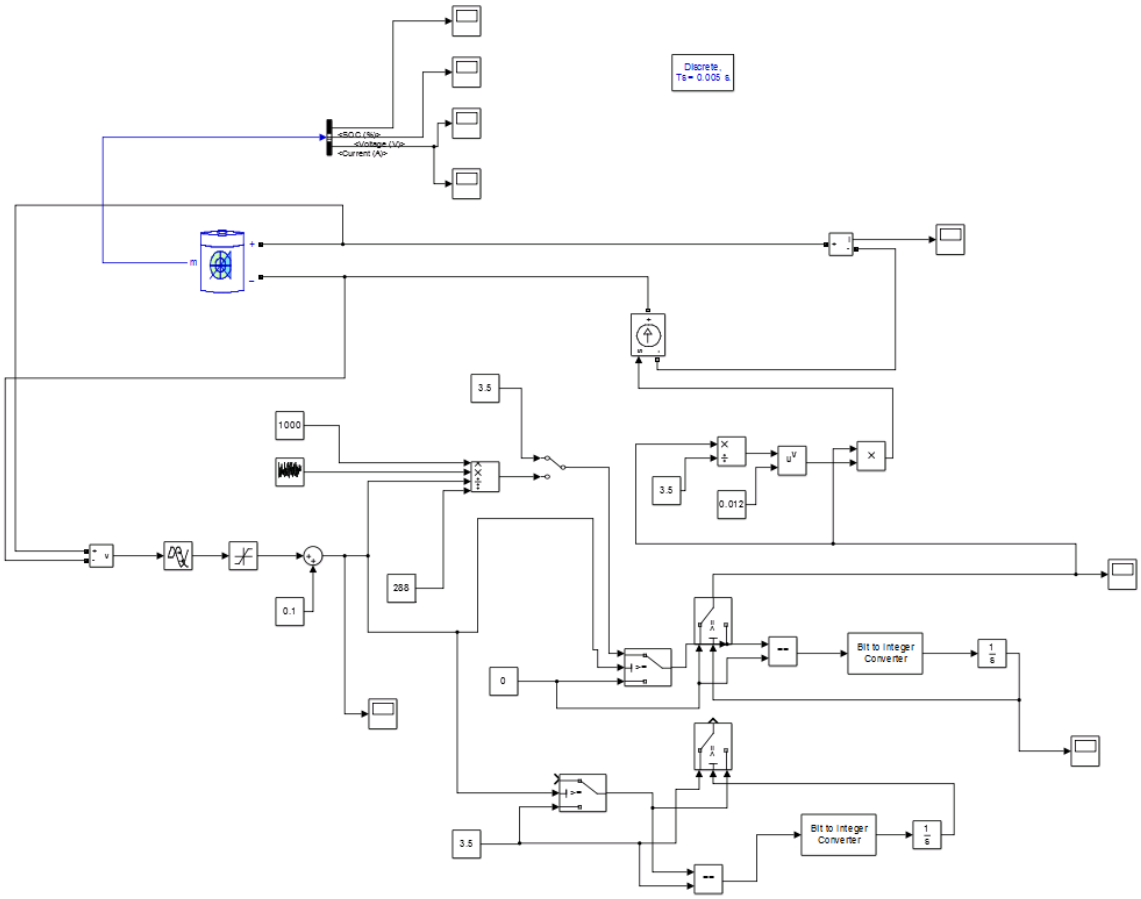

Figure 5-3: Configured Simulink model used in the master thesis work

The Simulink addition to Matlab contains a Lithium – Ion battery in its library. In this master thesis work, the configuration of this block and the validity of the block for simulation of a racecar tractive system is evaluated. The more important model assumptions that are made within the lithium ion block are:

- No Peukert's effect
- No self-discharge rate

- No memory effect

In order to represent the tractive system battery as precise as possible, the lithium – Ion battery block is configured to fit the cell characteristics. As lithium – Ion cells behave differently, it is deemed necessary to perform tests on the specific cell to properly evaluate the integrity of the model. An elaboration of the model configuration is presented in appendix A.

5.3.2. Evaluating remaining capacity

When the battery is subjected to elevated currents, it responds with a voltage drop. The magnitude of the drop is strictly dependent on the configuration of the exponential zones in the Simulink block. To evaluate the remaining energy at the end of the simulation period, the model is expanded to measure how much capacity is left at 0.5C after cut – off voltage is reached for the first time. In Figure 5-4, the model extension is highlighted with a surrounding red line. As the voltage drops to cut – off voltage, the model will switch of the initial load and discharge the remaining capacity with 0.5 C.

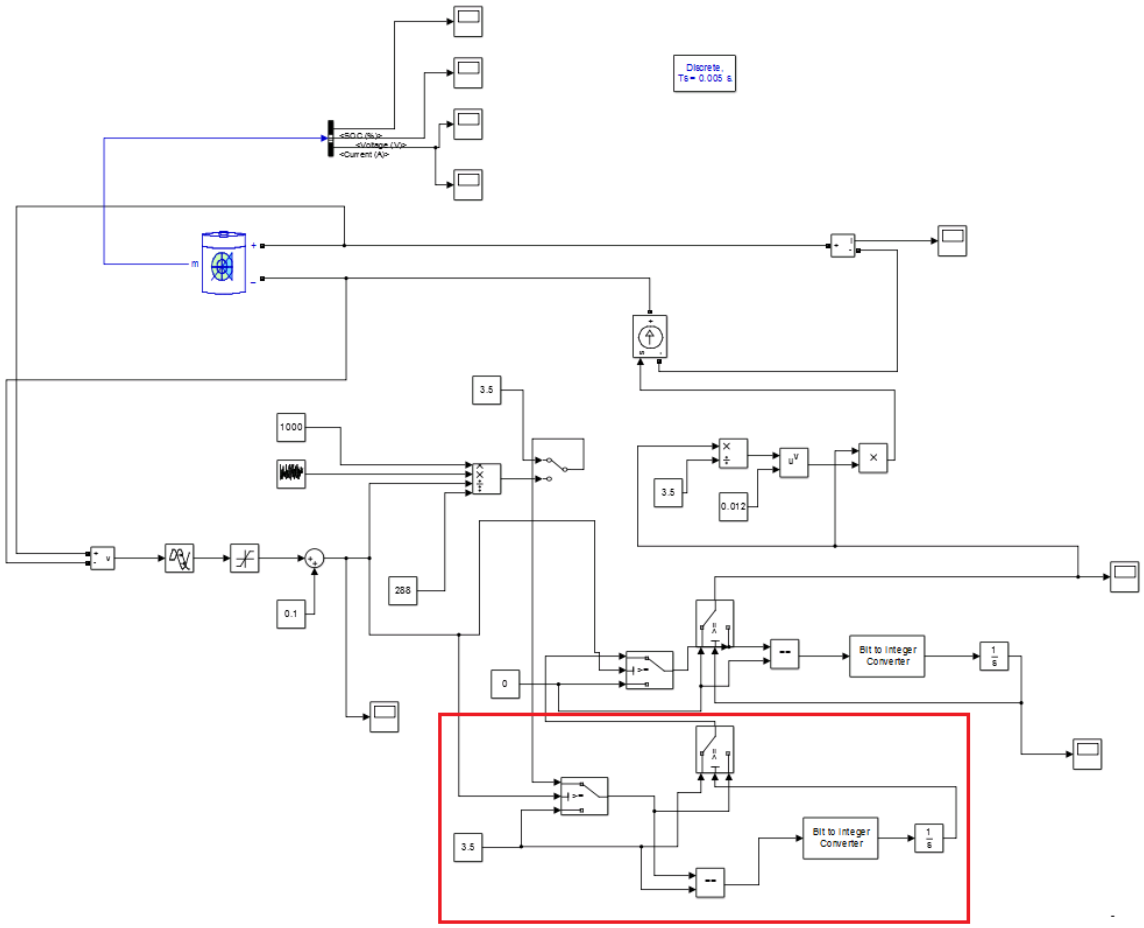

Figure 5-4: Simulink model extension to evaluate remaining energy in the battery block when cycling with elevated constant current.

These results are necessary both to evaluate the need of modifying the block – configuration and to properly model Peukert's effect using the Simulink software.

5.3.3. Modelling Peukert's effect

As the Simulink block does not account for Peukert's effect, a model extension is developed to attend to the losses connected to elevated currents. The original current signal calculated from the voltage over the battery and the predefined power is routed through several blocks that convert the current to the effective current found from Peukuert's equation. Such a setup models a variable load profile as short time-lapses where current is constant, as shown in equation (2.8). The effective current is then used to discharge the battery, while the original current is extracted to the Matlab workspace for parameter evaluation.

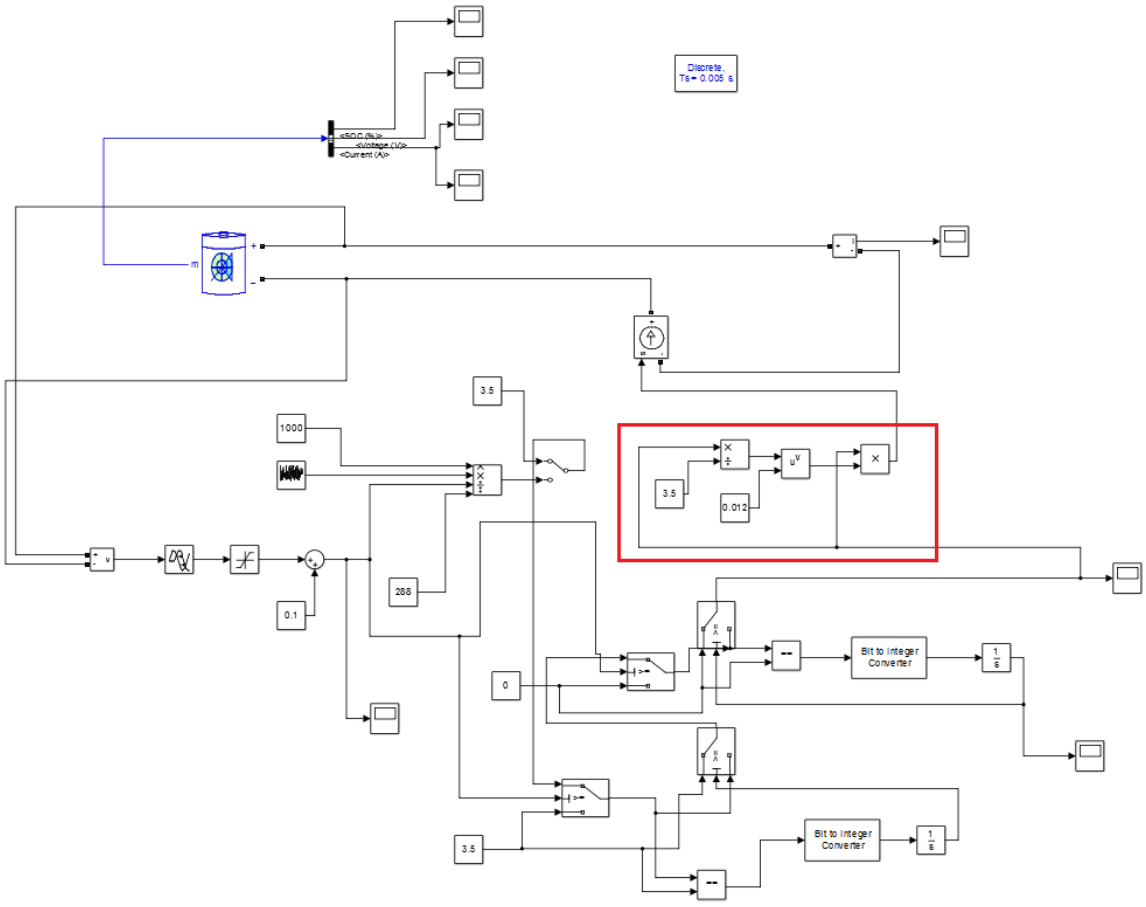

Figure 5-5: Simulink model with extension for Peukert's effect. Extension highlighted in red. In this figure, the extension for evaluation remaining energy in the model is disconnected.

5.4. Matlab

The Simulink model returns a number of values from the scope blocks in the model to the Matlab workspace as arrays. Consequently, the arrays are used by a Matlab script developed for this master thesis to interpret the results of the simulations. The scripts can be seen in appendix C. Basic power and energy calculations are performed by the script, as shown in equation(5.2), where energy and capacity is found based on current and voltage. As the simulation time - step is in the range of $5x10^{-4}$ no linearization techniques are considered necessary to make the results more accurate.

$$P = UI$$
$$Energy = \sum_{n=t_0}^{t_{end}} \sum_{t=t_n}^{t_{n+1}} P(t) \qquad (5.2)$$
$$Capacity = \sum_{n=t_0}^{t_{end}} \sum_{t=t_n}^{t_{n+1}} I(t)$$

The user interface of the program returns the important simulation data, like capacity, energy, average power and simulation time.

Matlab is also used to analyze the results from experimental tests B and C, presented in chapter 8.3 and 8.4. Data from the tests is stored as text files, and the developed script is written to extract the desired data and present it as matrixes in the Matlab workspace. The full code can be seen in appendix B.

5.5. Solidworks 2013

As system integration is a crucial part of the engineering task exercised in this master thesis, CAD software is utilized to model the complete system. The designed accumulator system is visualized in Figure 5-6 as an example of the use of Solidworks 2013 software.

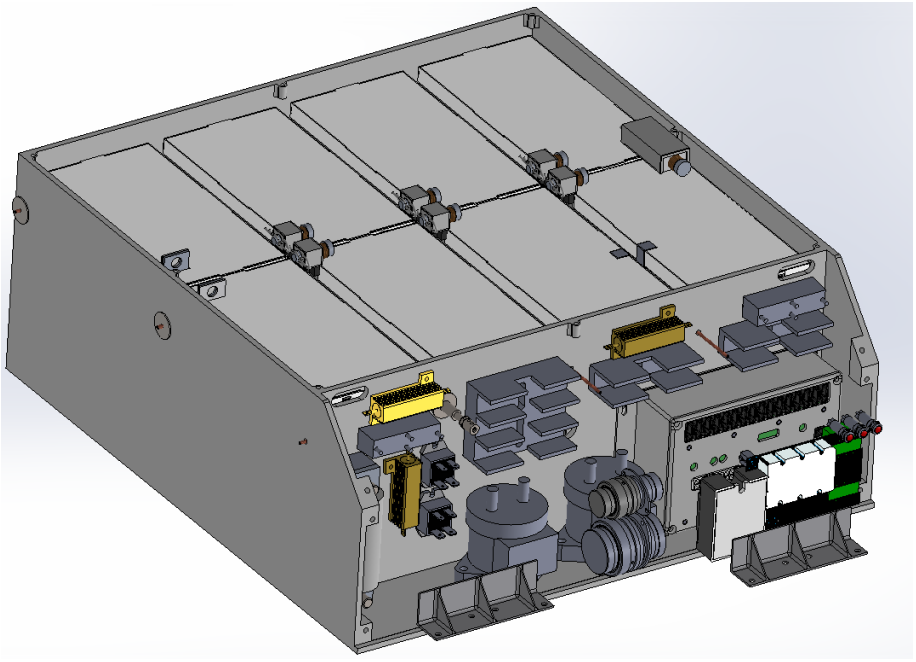

Figure 5-6: Tractive system accumulator CAD – rendering.

The complete tractive design system is further integrated into the complete race-car, as shown in Figure 5-7, where the HVD and TSMP are illuminated for graphical purposes.

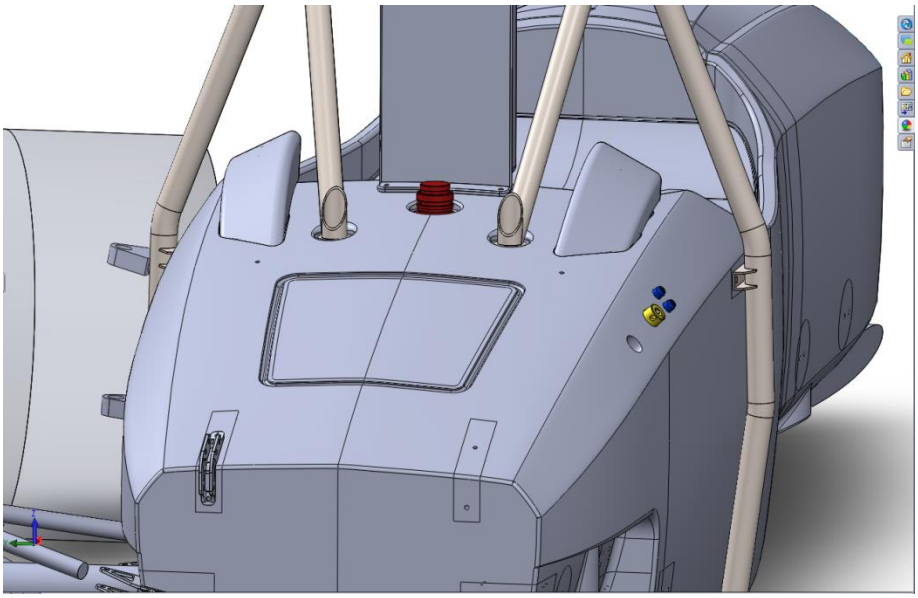

Figure 5-7: CAD – rendering of HVD and TSMP integration.

6. System description

6.1. Introduction

Figure 6-1 shows the topology of the designed tractive system with all major parts. Cables connected to the 600 V system are highlighted with orange. The cables connecting the 12V power supply are marked with black. This chapter will briefly explain how the tractive system works.

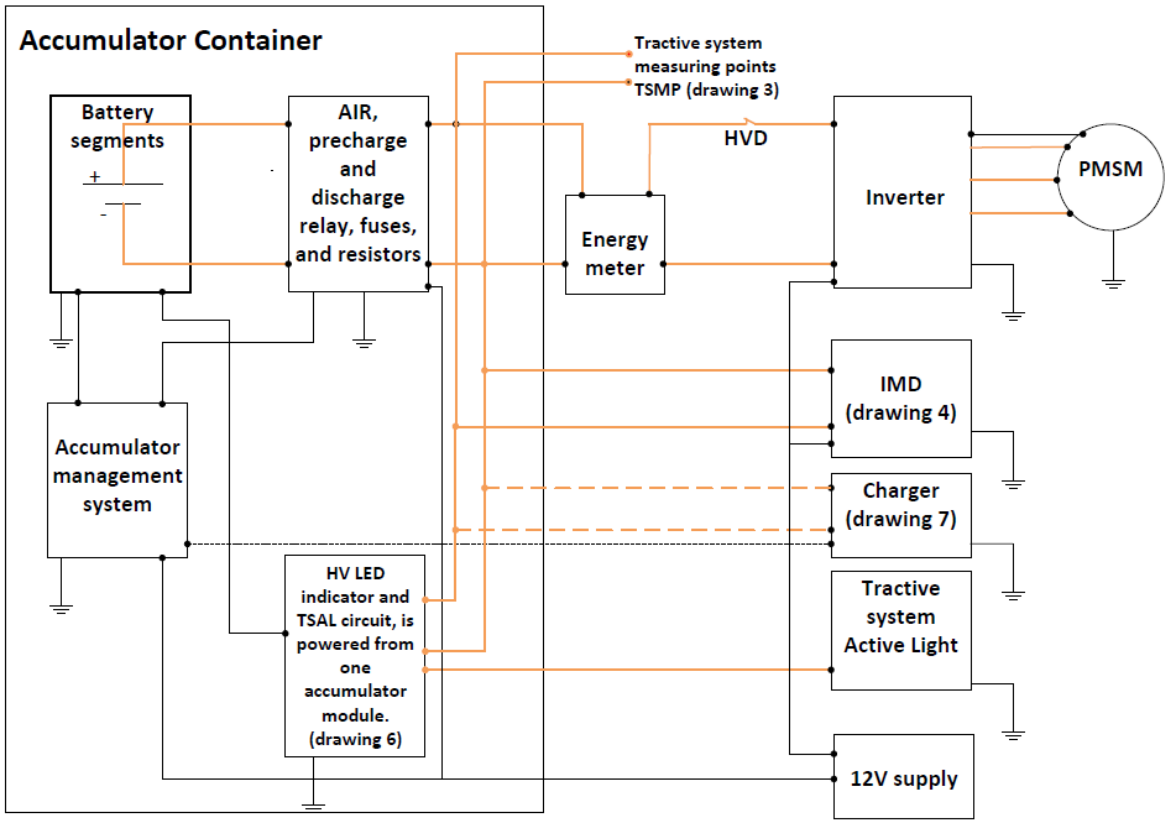

Figure 6-1: Overview schematics of the tractive system.

6.2. Accumulator system design

The accumulator is separated in eight identical segments. Each segment is encased with a firewall casing constructed with a 0.8 mm thick glass mat polyester material. Quick release connections, described in chapter 6.5.2.3, connect the segments. A rigid carbon fiber casing is molded to hold the battery – segments inside the vehicle. On the inside of this casing, 0.18 mm nomex paper is molded in with the carbon fiber to protect personnel and equipment from a fire. The safety circuit is connected in the same casing, but is separated from the batteries with a carbon fiber wall covered in nomex. The AMS cell boards, further elaborated in chapter 6.4.4, are placed on a specially designed PCB and taped to the side of the

segment casing wall. Thermal paste is used on the cell wall to ensure direct thermal contact between temperature sensors in the AMS and the LCO cells. All cell boards are powered through sense – wires connected to a battery element, consisting of two parallel connected batteries. A total of 16 mid – boards and two end boards are connected to each segment, creating an individual AMS bank. All eight banks are connected directly to the AMS master. The PCB with soldered sensing wires prior to installation is shown in Figure 6-2. One complete module with electrical connections and sensing wire connected can be seen in Figure 6-3.

The complete accumulator system can be seen in Figure 5-6, and the AMS schematics are found in and Figure 3-1.

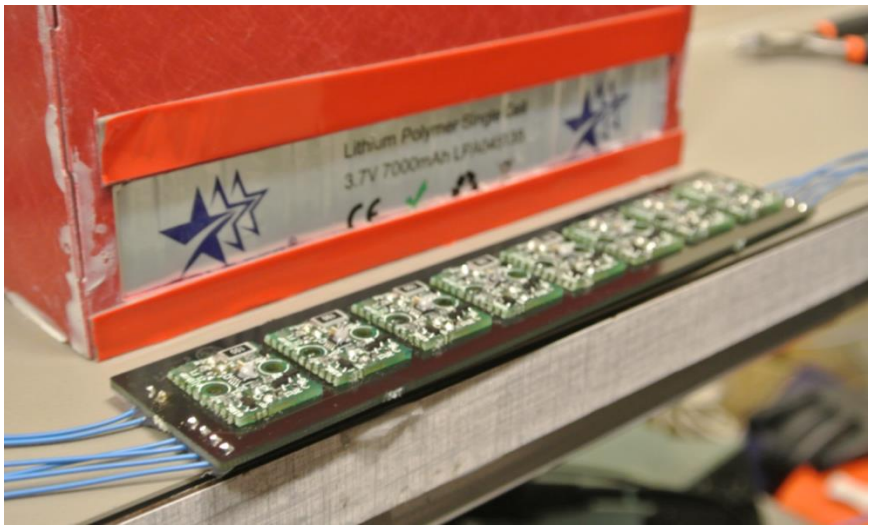

Figure 6-2: AMS cell boards prior to installation on its respective module.

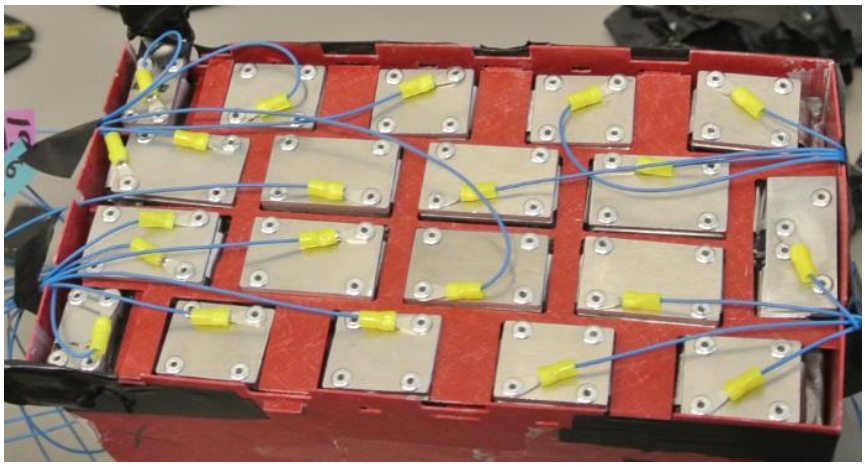

Figure 6-3: Overview of electrical connection in one battery module with sensing wires connected with a cable lug and pop rivets.

6.3. System overview

The connection of the 600V circuit with the accumulator battery segments, AIRs, discharge- and pre-charge circuits, IMD voltage sensing, TSMS, inverter and motor is described in Figure 6-4. When the tractive system is activated the negative AIR (-K2), pre-charge relay (-K3) and the discharge relay (K4, and K5) will be energized. The inverter capacitors are subsequently charged trough the pre-charge resistor to minimum 90% of the accumulator voltage. At this point the engine control unit, ECU, closes K1 through K12 and clears the fully energized drivetrain for normal operation.

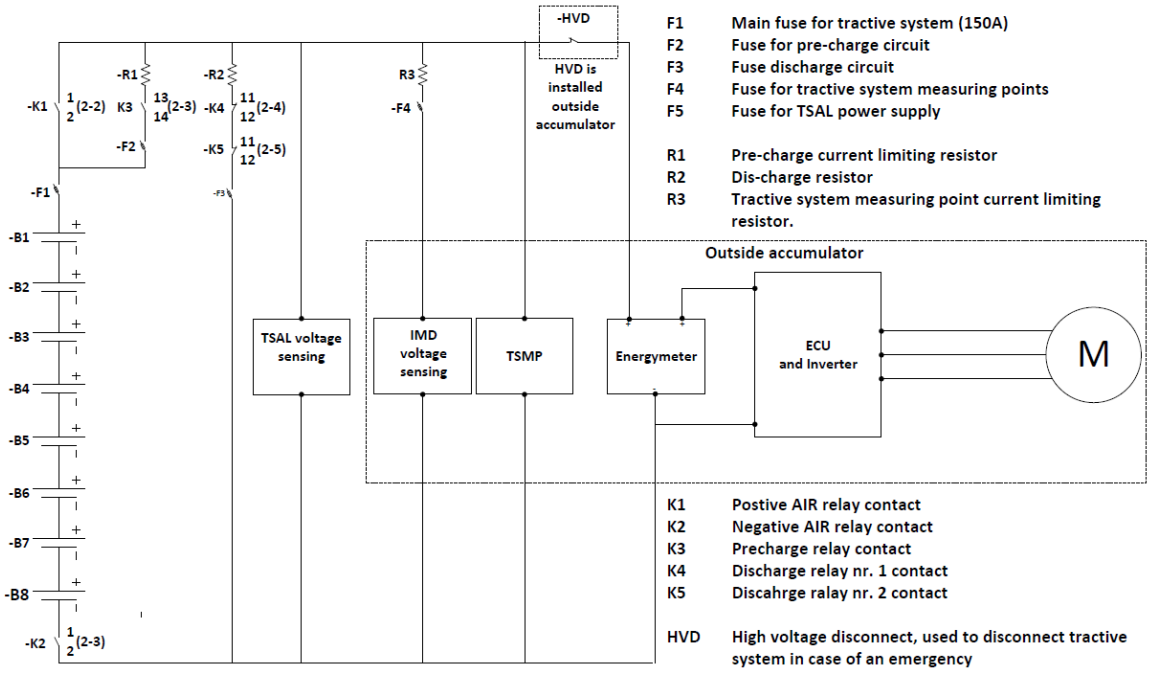

Figure 6-4: Schematics describing the 600 V circuit.

6.4. Safety systems

Both because of the safety concern regarding the accumulator and the elevated voltage levels in the tractive system, flawless operation of the safety system are absolute necessities. Typical faults that could arise are loose connection, ground faults, low insulation levels, short circuits and mechanical damage due to strain or crash. The following chapter describes the complete safety system. Schematics describing the shutdown circuit are presented in Figure 6-5. Software protection within the ECU and inverter that are not directly connected to the shutdown circuit will not be discussed.

The integration of the relevant components mentioned throughout this chapter is described in Figure 6-4 and Figure 6-5, and all components discussed can be found in these figures.

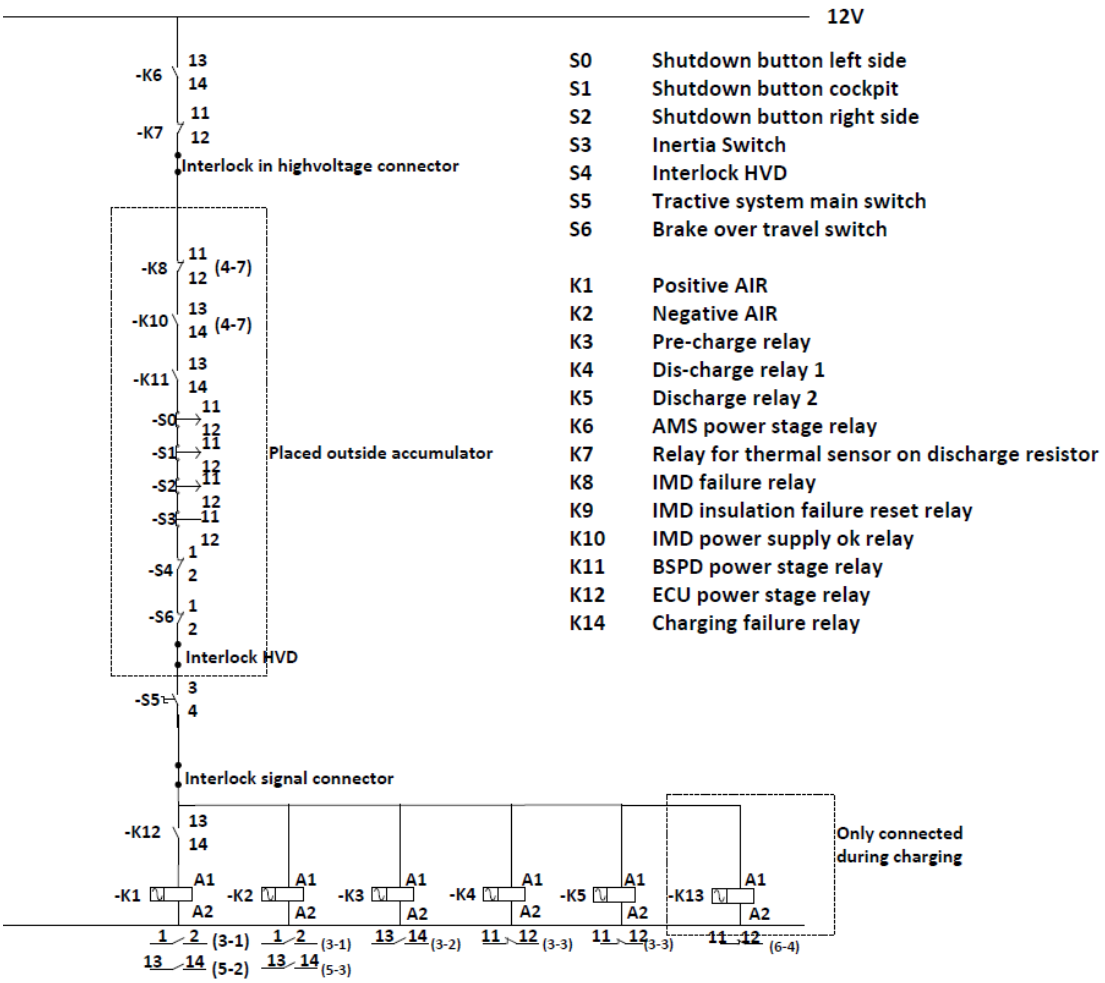

Figure 6-5: Schematics of the shutdown circuit.

6.4.1. Fuses

The vehicle is equipped with fuses to protect the system components from continuous overload and short circuit. As fuses are installed to protect a circuit from overcurrent, the fuse rated current should be lower than the current rating for the other components in the circuit. The vehicle is equipped with 4 high voltage fuses; one 150A main fuse, and three 0,5A fuses for pre-charge, dis-charge, and IMD voltage sensing circuit.

6.4.2. Insulation monitoring device

The insulation monitoring device, IMD, continuously monitors the insulation level between the insulated HV-conductors and vehicle ground. Its main function is to

protect driver or service personnel from electric shock due to ground faults. If the insulation resistance drops below 350 kΩ the device activates the shutdown circuit through the IMD power stage relay K9.

Bender emobility's IMD model A-isometer IR155-3203 is the chosen component to perform this task. It is specially designed for unearthed DC drive systems in electrical vehicles. The IMD generates a pulsed voltage that is superimposed on the system voltage to measure the system insulation. [39]

6.4.3. Relays

The high voltage system is equipped with high voltage relays that isolate the accumulator from the drivetrain, enable pre-charge circuit and dis-charge circuit.

6.4.3.1. Accumulator insulation relays (AIR)

There are two 600V relays installed in the high voltage link between the accumulator and the drivetrain to be able to electrically isolate the accumulator poles from the vehicle. Two relays are installed for redundancy; if one of the relays should fail the other will still be able to isolate the accumulator. The relays are dimensioned to be able to break currents superior to the rated system current to reduce the probability of welded contacts in the relays. Inverter and motor cannot be energized before both AIRs are closed.

6.4.3.2. Pre-charge relay

The pre-charge relay together with the current limiting resistor, R1, is installed to reduce the inrush current when the inverter is energized. When the inverter voltage reaches 90% of the accumulator voltage the ECU relay close the positive AIR through K12 -13,14, and the inverter is ready to energize the engine. Figure 6-6 and Figure 6-7 present the estimated voltage rise and current fall during pre-charge. The plots are derived from the formula (6.1) and (6.2).

Pre – charge voltage	600 VDC
Inverter capacitance	500 µF
Pre – charge resistor	1500 Ω

Table 6-1: System parameters for calculations of pre-charge circuit behavior.

$$V_{Pre-charge} = V_0 \cdot (1 - e^{-\frac{t}{R_{pre-charge}}}) \quad (6.1)$$

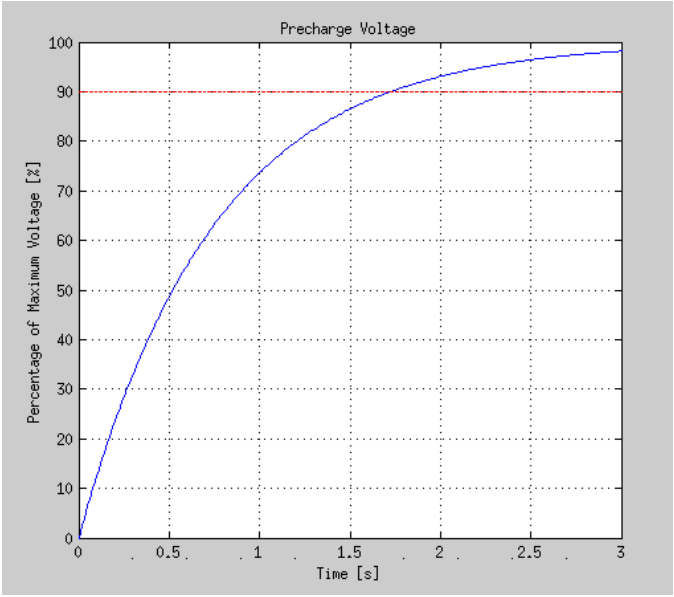

Figure 6-6: Inverter voltage rise during pre – charge.

$$I_{\text{Pre-charge}} = \frac{V_0 - V_{pre-charge}}{R_{pre-charge}} \tag{6.2}$$

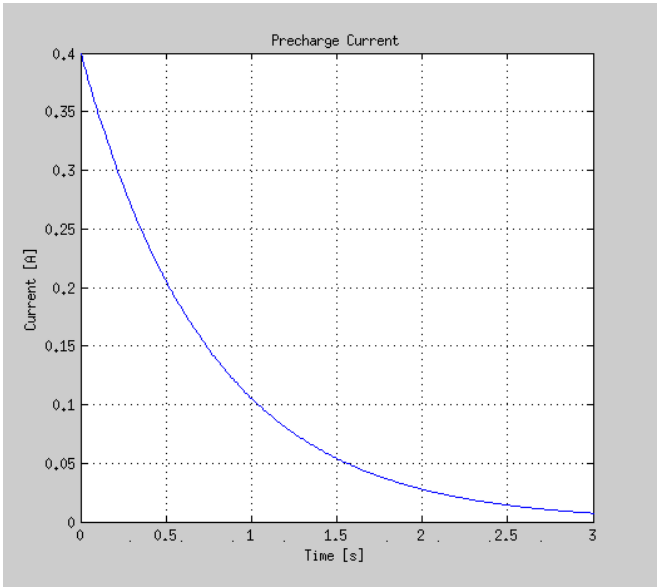

Figure 6-7: Current development in pre-charge circuit during pre – charge.

6.4.3.3. Discharge relay

The discharge relay connects the inverter input to a 1.5 kΩ resistor when the shutdown circuit is opened. Energy stored in the inverter capacitors are then dissipated in the discharge resistor, R2. Within a time – frame of <5 s from opening the AIRs, the tractive system voltage will drop below 40VDC. Since

resistor (R3) can burn out if exposed for prolonged periods of time, two relays with normally closed contacts are chosen for the discharge circuit for redundancy. R3 is also equipped with a temperature sensor and a relay that will open the shutdown circuit if the resistor reaches a critical value Figure 6-8 and Figure 6-9 shows the estimated voltage and current development during discharge circuit operation. [40]

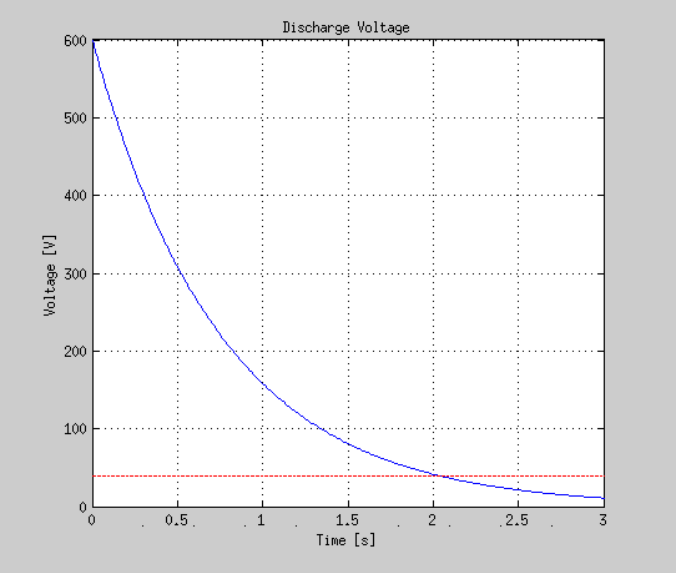

Figure 6-8: Voltage development in the vehicle side of the tractive system during discharge circuit operation

The voltage plot in Figure 6-8 is found through equation (6.3).

Initial tractive system voltage	600 VDC
Inverter capacitance	500 µF
Discharge resistor resistance	1500 Ω

Table 6-2: System parameters used to calculate the discharge circuit behavior during operation

$$V_L = V_0 \cdot e^{-\frac{t}{R_{discharge} C_{inverter}}} \tag{6.3}$$

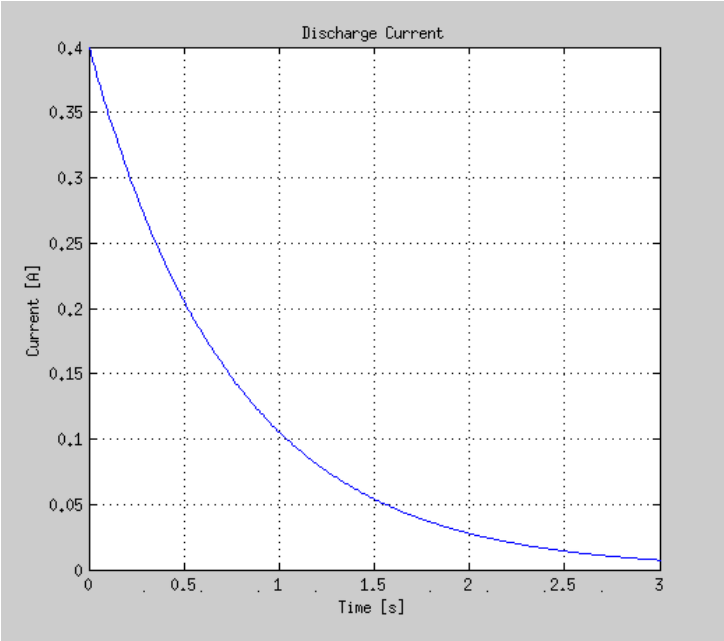

Figure 6-9: Current development in the discharge circuit during discharge operation

The current plot in figure Figure 6-9 is obtained from equation (6.4).

$$I_{discharge} = \frac{V_{discharge}}{R_{discharge}} \tag{6.4}$$

6.4.4. Accumulator management system

The accumulator management system monitors voltage, current and temperature in all battery segments. If the AMS detects critical cell temperatures, cell voltages or power consumption the AMS will go into fault mode and open the shutdown circuit through the AMS power stage relay, K6. From manufacturer "Elithion", the lithiumate pro accumulator management system is selected for the designed accumulator system. The Lithiumate pro supports up to 256 cells. As explained in chapter 4.2.2, the system will employ a 144s2p configuration, requiring voltage measurements of 144 cells. In chapter 3.2, the common cell balancing techniques are elaborated. Given that the system will have plenty of rest time in between charge – cycles, passive balancing is the favored balancing concept. Using passive balancing also reduces the complexity and thus the weight and sources of errors in the system. Through resistors placed on each cell board, the AMS automatically dissipates energy from the cells with elevated SOC when balancing is activated. Integrating the AMS with the rest of the communication system in the car requires CAN compatibility, which is supported by the lithiumate pro. Applying the distributed system from Elithion allows 18 temperature measurements on each

segment, adding up to a total of 44.4 % of all cell temperatures being continuously monitored by the AMS.

6.4.5.Brake system plausibility device

Brake system plausibility device (BSPD) detects if the brake pedal and the accelerator are used at the same time. The BSPD compares the brake pressure signal and the current flowing to the motor. If the brake and accelerator is used at the same time for more than 5ms, the BSPD will open power stage relay, K11. The relay is locked and will not open before the 12V GLVM switch is power cycled.

6.4.6.Brake over travel switch

Brake over travel switch (BOTS) is located behind the brake pedal as shown in Figure 6-10. A leakage in the brake system will lead to reduced pressure and brake pedal will easily be pushed far enough to activate the BOTS, the shutdown circuit opens through power stage relay S6

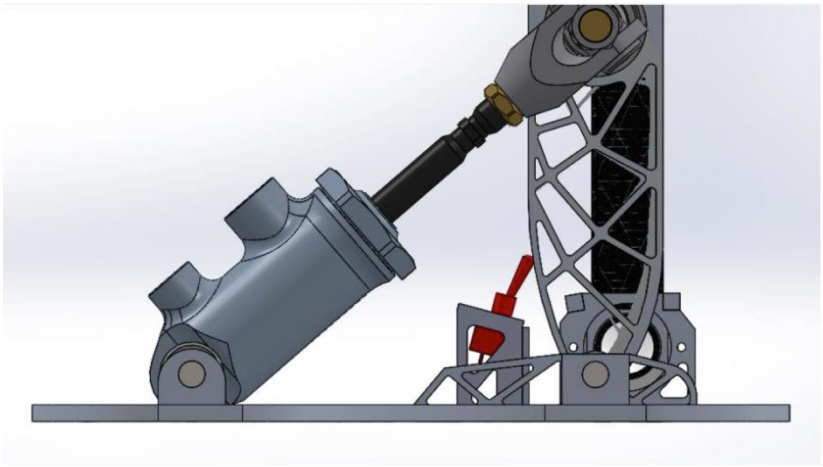

Figure 6-10: CAD – rendering of the position of the brake over – travel switch. BSPD highlighted in red.

6.4.7.Inertia switch

The crash sensor, or inertia switch, opens the shutdown circuit when a deceleration force superior to 25g for 10ms or 6g for 60ms is detected. It is connected to the shutdown circuit through power stage relay S3. The switch is delivered by Sensata Technologies and is calibrated for EV application.

6.4.8.Emergency switches

The shutdown circuit is equipped with three shutdown buttons. The switches can be seen as S0, S1 and S2 in Figure 6-5.

6.4.9. High voltage disconnect

High voltage disconnect, HVD, is a safety switch that disconnect the high voltage system directly through manual operation. The switch will be used if the AIRs contacts get stuck and do not open when signaled. The HVD is made out of two high voltage contacts where one is short-circuited with a bus bar and molded into polyurethane with elevated dielectric strength. The HVD is also equipped with an interlock that opens the shutdown circuit. Figure 6-11 show images from the current capability testing and molding process of the HVD construction.

Figure 6-11: Current capability test of the HVD and molding process.

6.4.10. Tractive system main switch

Tractive system main switch, TSMS, is a toggle switch installed on the side of the car. The TSMS and the grounded low voltage master switch, GLVMS, must be enabled to energize the drivetrain.

6.4.11. Tractive system active light

Tractive system active light, TSAL, is mounted on the top of the main hoop. Its function is to illuminate with a pulsating red light that blinks whenever the tractive system is energized. The TSAL is designed to illuminate when there is more than 40V on the vehicle side of the AIRS or whenever the AIRS are closed. The TSAL circuit is self-energized and functional even when the 12V supply is turned off. In other words, it will signal voltage outside the battery-pack if the AIRs contacts are stuck and 12V system is off.

6.5. Electrical connections

6.5.1. Introduction

Using the 144S2P configuration, a total of 152 DC bus bars are designed to transfer electrical load between the cells and out to the vehicle side of the tractive system. Concepts with ultrasonic and laser welding were considered, but due to lack of equipment they were dismissed. Two feasible concepts were further evaluated during the theoretical modelling phase of the master thesis work; welded connections and pressure based connections. Using equation (6.5) to find resistance in Ω/m for different designs, Table 6-3 and Table 6-4 are developed to compare theoretical system losses, losses based on measurements on prototype connections and weight calculations.

$$R = \rho \frac{l}{A} \tag{6.5}$$

Battery cells provided by the manufacturer have pure aluminum tabs, thus requiring bimetal transfer if copper bus bars are used. Because of the potential problems with transfers between aluminum and copper, and the added weight caused by the increased density of copper, only aluminum connections are considered.

6.5.2. Cell connections

6.5.2.1. Welded connections

Welded aluminum connections concept is visualized in **Figure 6-12**.

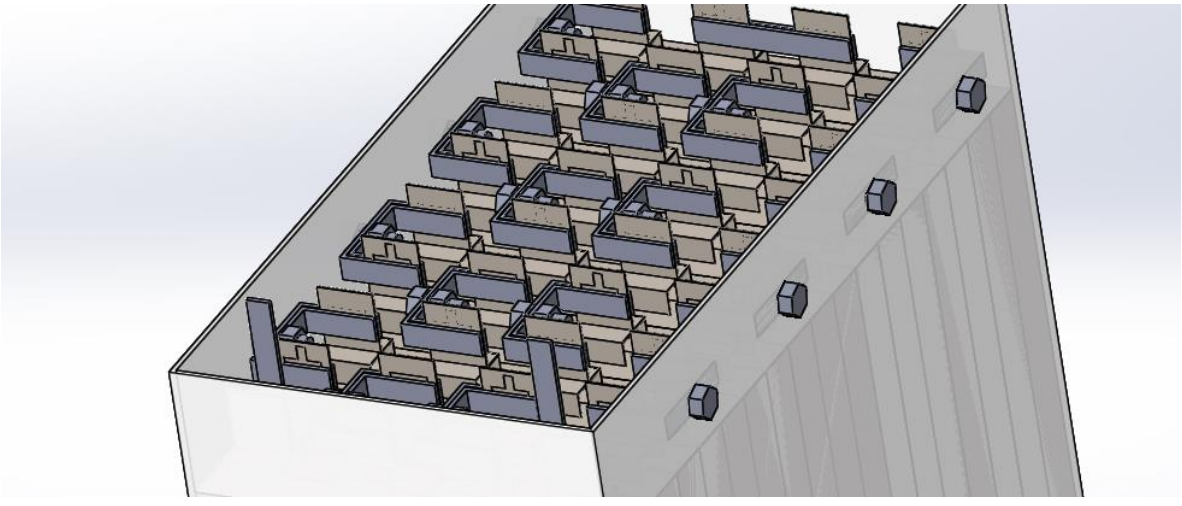

Figure 6-12: CAD Rendering of welded electrical connections in one battery segment.

Due to practical difficulties of welding the 0.2 mm aluminum tabs to the aluminum bus bars, prototype connections were only obtained for bus bars with dimensions 14mm x 2mm. Table 6-3 show the theoretical modelling of the losses calculated for the 144S2P battery system using the specified concept for connections. Density of aluminum is specified according to equation(6.6), and resistivity is defined according to equation(6.7). The length of each bus bar is 42mm.

$$P_{alu} = 2.7[g/cm^3] \tag{6.6}$$

$$\rho = 2.82 \cdot 10^{-8}[\Omega/m] \tag{6.7}$$

To account for temperature difference in connections, equation (6.8) is used to linearly approximate the resistance change relative to the temperature [49].

$$R_t = R_{t_0} + [c_0 \cdot (T - T_0)] \cdot R_{t_0} \tag{6.8}$$

C_0 is the temperature coefficient for aluminum, here defined from as 0.0038 [k^{-1}].

			20 °C		60 °C		Test Result	
Height [mm]	Thickness [mm]	Weight [g]	Theoretical resistance [Ω]	Voltage drop pack @160A [%]	Theoretical resistance [mΩ]	Voltage drop @160A [%]	Connection resistance [mΩ]	Voltage drop @160 A [%]
14	3	609.64	0.0036	0.11 %	4,2	0.13 %	n/a	n/a
	2	406.43	0.0054	0.16 %	6,3	0.19 %	75.5	2.27 %
	2	406.43	0.0054	0.16 %	6,3	0.19 %	95,7	2.87 %
10	3	435.46	0.0051	0.15 %	5,9	0.18 %	n/a	n/a
	2	290.30	0.0076	0.23 %	8,8	0.26 %	n/a	n/a
	1	145.15	0.0152	0.46 %	17,6	0.53 %	n/a	n/a
5	3	217.73	0.0101	0.30 %	11,8	0.35 %	n/a	n/a
	2	154.22	0.0152	0.46 %	17,6	0.53 %	n/a	n/a
	1	72.58	0.0303	0.91 %	35,3	1.06 %	n/a	n/a

Table 6-3: Calculations and test results for welded aluminum bus bars.

The deviation between test results and theoretical modelling is due to the connection resistance between battery tab and aluminum bus bar. Theoretical modelling does not account for the transition between parts.

6.5.2.2. Pressure – based connections.

The second concept is based on using two aluminum bus bars held together with pop – rivets to obtain pressure in the area between tabs, as seen in Figure 6-13. Table 6-4 presents the more important results from the theoretical modelling of the pressure – based connections. Type A rivets have diameter 2.4 mm and the type B rivets have 4 mm. Larger rivets are not compatible in the design due to the tab orientation on the cells.

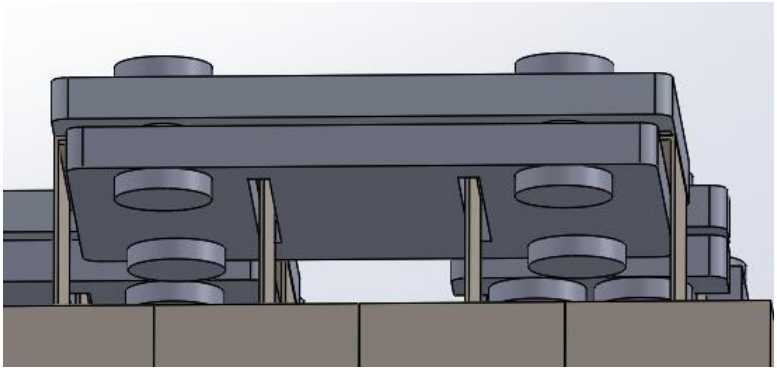

Figure 6-13: CAD – rendering of pressure based concept

				20 °C		Test results	
Width [mm]	Rivet type	Thickness [mm]	Weight [g]	Theoretical resistance [mΩ]	Voltage drop pack @160A [%]	Connection resistance [mΩ]	Voltage drop @160 A [%]
20.0 mm	-	5.0 mm	1728.0	1,1	0.03 %	-	
	A	4.0 mm	1382.4	1,4	0.04 %	41,792	1.26 %
	B	4.0 mm	1382.4	1,4	0.04 %	98,72	2.96 %
	A	2.0 mm	656.6	2,7	0.08 %	80,672	2.42 %
	B	2.0 mm	691.2	2,7	0.08 %	68,224	2.05 %

Table 6-4: Theoretical modelling of connection losses for pressure based aluminum bus bars.

6.5.2.3. Quick release connections

To allow battery segments to be disconnected without the use of tools, quick release connections are designed based on a spring system with positive locking. The connections can be seen in figure 5-15, and the theoretical modelling compared to measured results of the aluminum bus bar is presented in Table 6-5. Three different connectors were designed for system integration. Measurements are performed on the connector with the lowest cross – sectional area using an average current of 70 A. Voltage drop over the connection is logged over current. The experimental results represent the average voltage drop recorded during the tests. The isolation is 3D – printed and washers are made of MICA – material.

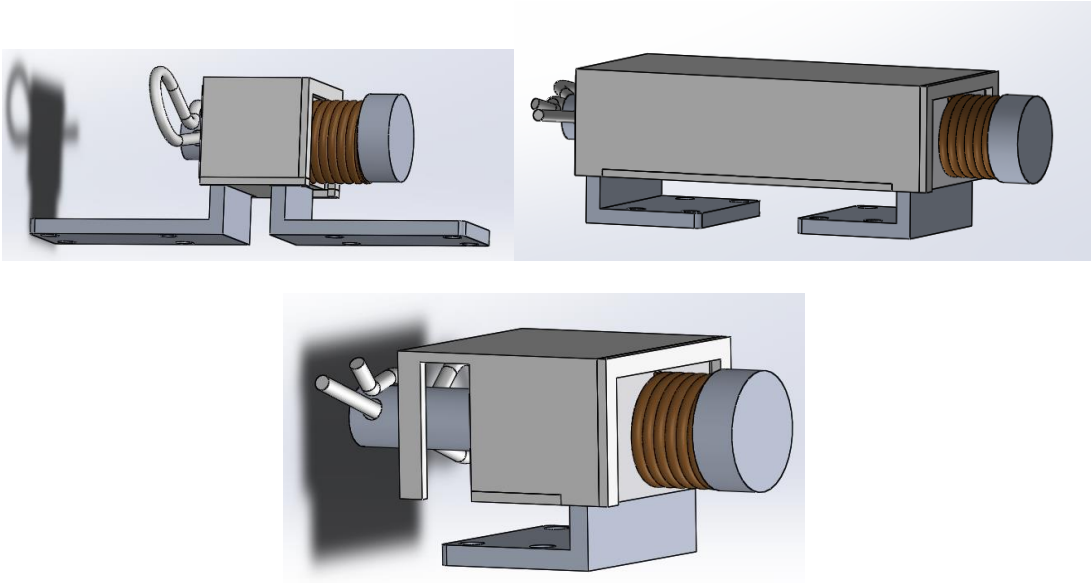

Figure 6-14: Designed quick release connections for separation of battery segments.

As seen in Table 6-5, the connection resistance is elevated compared to the theoretical model. The deviation is assumed to because of the transition between aluminum bus bars in the connection point.

Theoretical				Measured		
Type	Cross section [mm2]	Length [mm]	Theoretical resistance [mΩ]	Avg. Current [A]	Avg. Voltage drop [mV]	Resistance [mΩ]
A	116,41	6,6	0,0016	69,4	111,3	1,603746
B	183,38	43,3	0,0067	69,9	103,9	1,486409
C	214,98	10	0,0013	68,4	94,7	1,384503

Table 6-5: Theoretical modelling of quick release connectors

6.6. Charging system

The charging system is based on two 3 kW EV power charger modules delivered by Eltek Valere [41]. This provides a total of 6 kW at a maximum DC voltage of 720 VDC. In order to reduce temperature development, heat sinks are produced and attached to the modules. As the modules communicate through CAN with the AMS, safety of the batteries is ensured through the AMS critical value configuration. In addition, the modules have built in temperature and current sensors protecting the modules from overload. To allow manual start / stop and emergency shutdown, the modules are coupled through an emergency switch and a start / stop button. The full system is described in Figure 6-15.

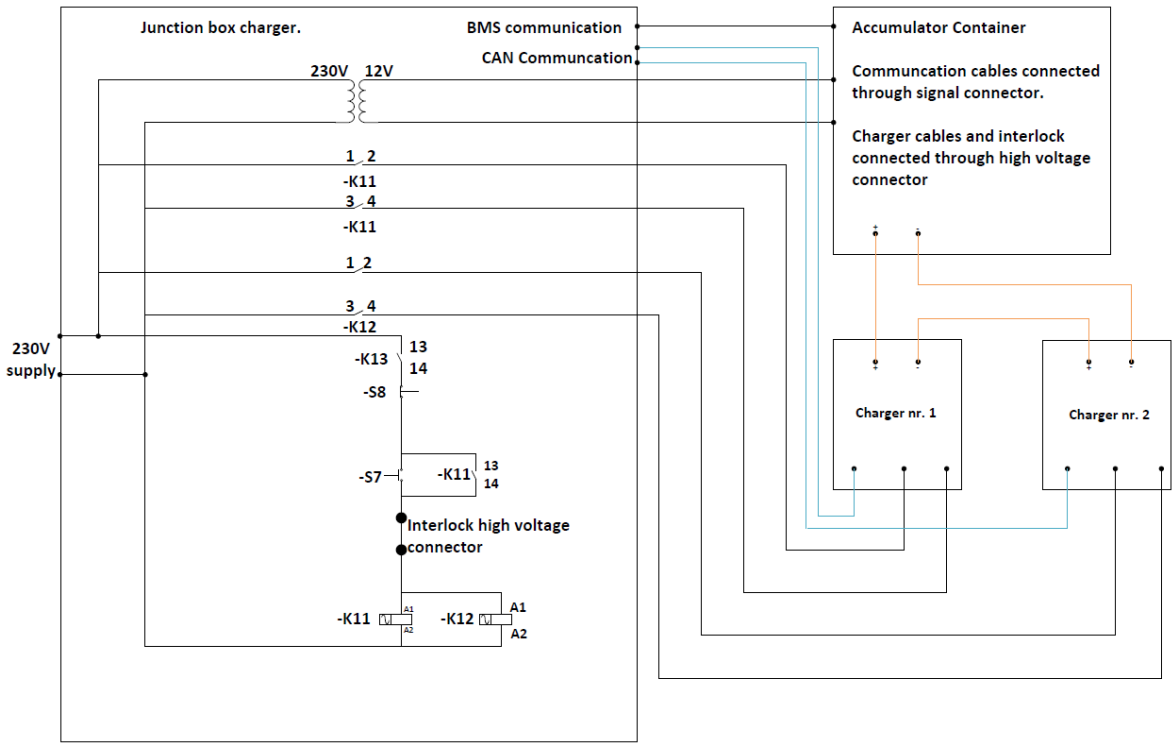

Figure 6-15: Schematics showing the charging system design.

7. Experimental - Tractive system tests

7.1. Full-scale testing of tractive system in water brake

Prior to installation in vehicle the system was thoroughly tested in a water brake at Department of Energy and Process Engineering, NTNU. This provided an opportunity to evaluate the complete system with elevated loads in a controlled environment where fewer factors could influence the test result. Running the system in the water brake facilitates detection of faults and design weakness compared to a complete system integrated in the vehicle. Repairs and improvements are also much easier to do.

The main goals for the water brake tests were:

- Functional testing
- Test of accumulator performance and liability
- Tune ECU regulator in order to reduce in car tuning.
- Getting familiar with the system and look for possible improvements and weakness in the design.
- Test system efficiency by measuring voltage, current and compare them it with rpm and torque measurement done by the water brake.
- Monitor accumulator temperature
- Observe the system with IR camera during operation looking for spots that develops heat.

Figure 7-1: Setup of accumulator during water – brake testing.

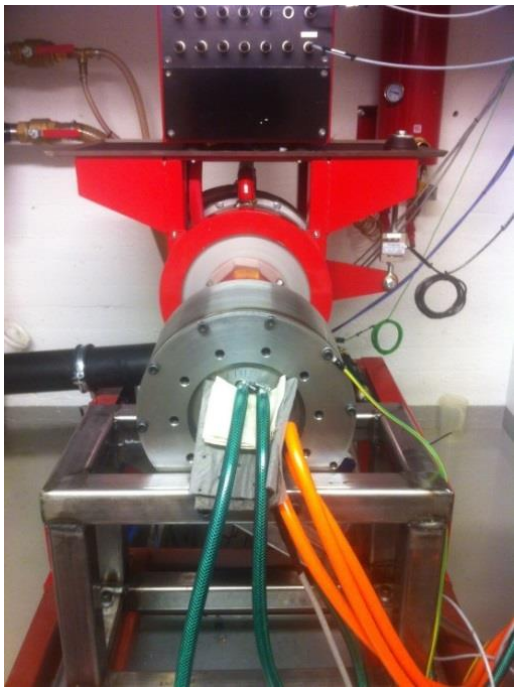

Figure 7-2: Setup of motor and water brake

7.1.1. Test setup

A simple schematic of the water brake setup is shown in Figure 7-3 with accumulator, inverter, PMSM and water brake. Two temperature sensors were placed inside one of battery modules to verify that the temperatures measured by the AMS temperature are within satisfactory accuracy. Voltage and current measurement were enabled at the DC-side of the inverter. For system evaluation, it would have been preferable to measure current and voltage on the AC-side of the inverter to, enabling analysis of inverter losses. However, the inverter produces harmonic distorted waveforms and it is only possible to measure with extensive measurement programs. Because of this, the inverter losses are planned for theoretical evaluation with motor and water brake data.

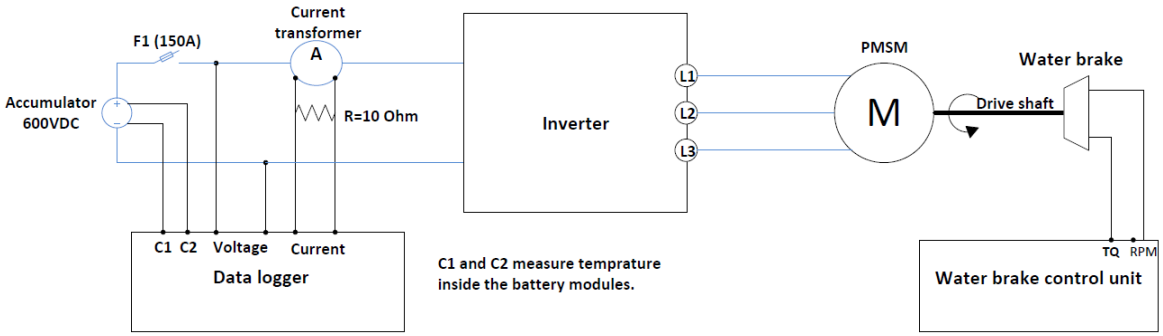

Figure 7-3: Test setup in water brake

7.1.1.1. Apparatus used for current and voltage measurements:

Temperature, voltage and current measurements were done with Agilient data logger with Agilient Benchlink software. Sampling time was set to one per second. General information about the data logger can be seen in Table 7-1. The logger records sampled data as csv-files that can be imported and processed in Microsoft excel.

Fabricant	Modell	Serial number	Sampling time	Software used to program the logger	Maximum voltage
Agilient	34972A	MY49003558	1/s	Agilient Benchlink Data logger 3. Version 4.3	300 V

Table 7-1: Description of data – logging equipment used during the water brake tests.

From Table 7-1 the maximum rated voltage of the apparatus is 300V. To measure the accumulator voltage (up to 600VDC), differential voltage probes were installed. Probe from Tektronix was used, which is designed for voltage levels up to 1000VDC or 1000VAC rms. The probes were set on transition from input to output from 500 to 1, this was also done in the logger program so that the correct values were directly displayed. Table 7-2 systematically describe the probe's general data.

Fabricant	Modell	Serial Number	Voltage type	Maximum voltage
Tektronix	P5200A	CO20651	AC and DC	1,000V RMS (1/500 position for connections above 130V rms)

Table 7-2: Description of voltage probe used to capture data from water brake tests

Current transformer from LEM was used to generate a current equivalent signal. The ratio of the transformer is 1/2000. With a 10Ω resistance connected over the transformer output, the current flowing in the tractive system is found through equation (7.1)

$$V_2 = \frac{V_1}{2000} \tag{7.1}$$

Current flowing in the tractive system (I_{TS}) is found by using the transformer output voltage (V_2) equation (7.2):

$$I_{TS} = \frac{V_1}{R} = \frac{V_2 \bullet 2000}{R} = \frac{V_2 \bullet 2000}{10} = V_2 \bullet 200 \qquad (7.2)$$

In data logger software the measurement multiplied with factor of 200 to get the actual current value directly displayed. General transformer data can be seen in Table 7-3.

Fabricant	Modell	Type	Voltage type	Maximum Current	Ratio	Ratio with 10 Ohm resistance
LEM	Current module	Trafo Shunt	AC and DC	300A	1/2000	200A/V

Table 7-3: Description of transformer used in the measurement circuit during the water brake tests.

7.1.1.2. Water brake setup

A water brake of model XS-211 from Stuska Dynamometers, Table 7-4, is used and is specially designed for testing of engines. Figure 7-4 shows a simplified model of the water brake setup. Load pump P-1 pumps water from T-1 to T-2 through the water brake W-1 that works against P-1. The PMSM is connected. P-3 pumps the water back to T-1 when water level in T-2 reaches a certain level.

The load pump is frequency controlled by a Mitsubishi E700 frequency converter. During testing the developed load pump - torque will be increased step by step, to make sure that the motor regulator is able to follow and increase the torque developed by the motor M-3. Tuning of the regulator was in important part of the tests.

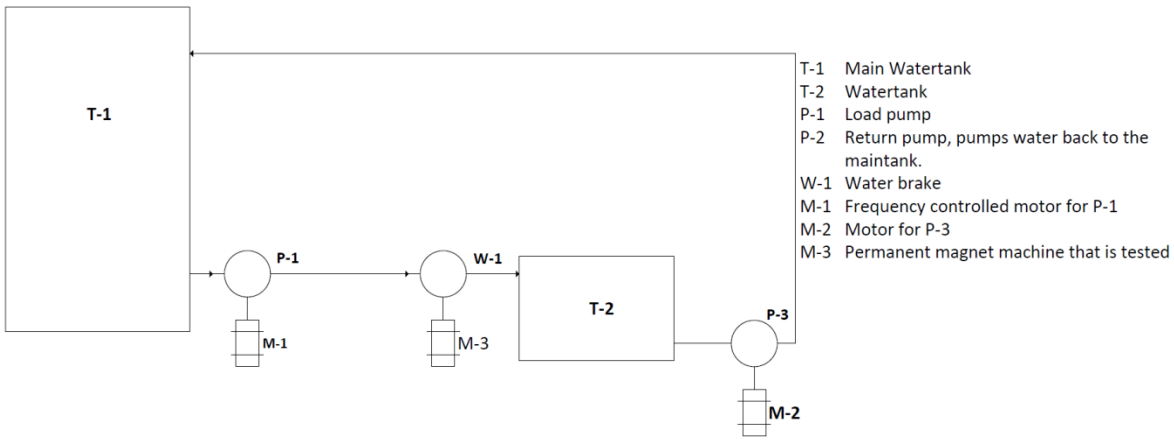

Figure 7-4: Schematics of water brake test setup

Labview software from National Instruments is used to control the frequency converter and to collect the test result. They are saved as TDMS-files and can be imported to Excel for further analyses.

Figure 7-5: Torque sensor measuring torque developed by the PM-machine M-3

Figure 7-6: Speed sensor that measures the speed of the water brake drive shaft.

General water brake data is found in

Fabricant	Modell	Maximum Shaft speed	Maximum power	Controlled by
Stuska Dynamomteres	XS-211	9000 RPM	1600hp ≈100kW	Labview from NI

Table 7-4: Description of water brake used during laboratory testing.

Power is given by torque (τ) and angular velocity (ω)

$$P = \tau \cdot \omega \tag{7.3}$$

Shaft speed is given Hz (1/s) by Labview and has to be converted to ω (rad/s):

$$1Hz = 2\pi \frac{rad}{s} \tag{7.4}$$

Power transferred from the PM machine to the water brake is given by:

$$P = \tau \cdot \omega = \tau \cdot 2\pi \cdot v_{Hz} = Nm \cdot 2\pi \cdot \frac{rad}{s} = watt \tag{7.5}$$

7.1.1.3. Electromagnetic interference

To evaluate the need for additional shielding in the tractive system battery, it is necessary to map the magnetic interference from the drivetrain. According to theory in chapter 4.3 the main source of electromagnetic interference is the power converter. As the first step in the EMI – testing, this assumption is evaluated by running the system with, and without activating the switching modules, or the IGBTs, in the inverter and measuring the electromagnetic radiation. The setup of the tractive system is according to figure 6.1.

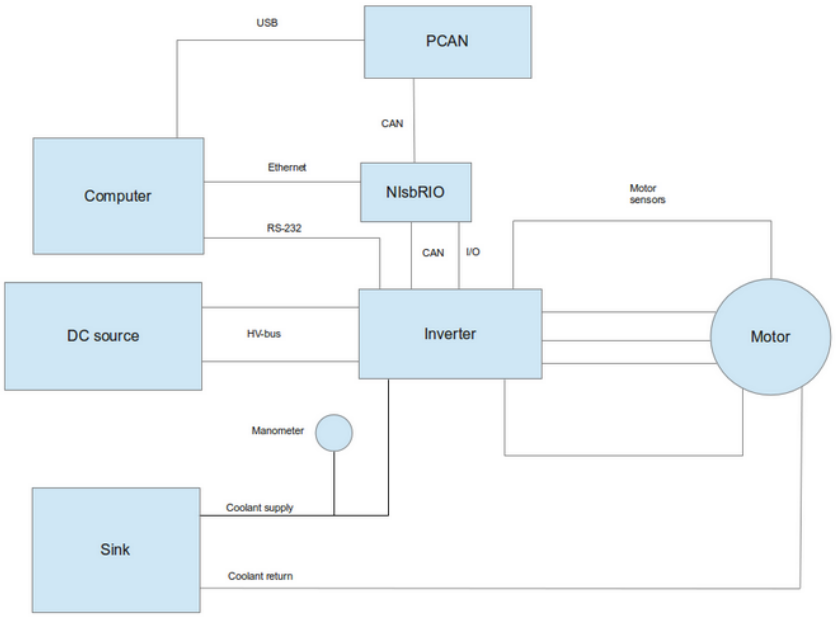

Figure 7-7: Test – setup of electromagnetic interference testing.

To receive the interference, an EMC – antenna of model EMCO Model-3141 is used and placed in a distance from the inverter corresponding to its position in car. To log and analyze the data from the antenna, a spectrum analyzer of model Anritsu MS2721A is connected. The complete setup is attached in figure 6.2.

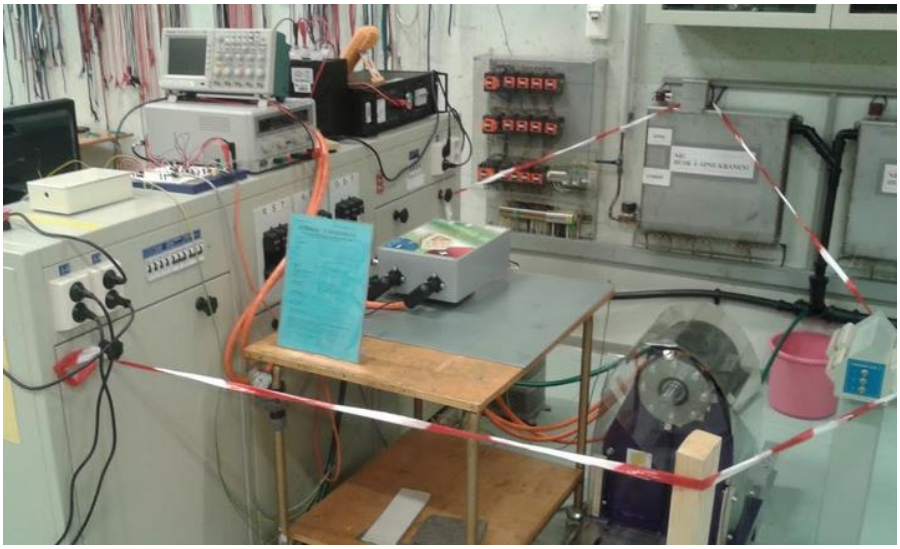

Figure 7-8: Test setup of electromagnetic interference tests.

The second step in the test procedure is evaluating at what frequency the interference is strongest. This is further explained later in the master thesis report.

8. Experimental – Battery evaluation tests

8.1. Introduction

To evaluate and verify the theoretical models, the battery cells are subjected to experimental testing. In this section, the battery theory from chapter 2 is put to the test with three specific focus areas. Test A attends to the current carrying capability of cells with different C – ratings, test B attends to the coherence of the Simulink model and battery behavior at elevated current loads, while test C focuses on cyclic lifespan of LCO batteries.

The data obtained from the battery tests B and C are processed using both excel and Matlab. The data stored from the Maccor series 4200 test - system is stored in .txt – files and read through the Matlab script attached in appendix B. Data is then plotted through Microsoft Excel or directly from Matlab.

8.2. Test A: C – rating evaluation

To obtain an optimal relation between specific energy, performance in terms of cell voltage and developed heat in the battery system, tests were performed on batteries with the same chemistry and structure, but different C – ratings. The test cells are compared in Table 8-1.

Model	LPB042126 (Cell A)	LPA245135 (Cell B)
Nominal Voltage	3,7 V	3,7
Max Cont. current	91,5 A (15 C)	56 A (8C)
Max pulse current	122 A (< 2 sec)	90 A (<2 sec)
Specific energy	167,185 Wh / kg	190,44 Wh / kg
Energy density	361,56 Wh / l	452,02 Wh / l

Table 8-1: Comparison of test – cells for C – rating evaluation tests.

The test setup is built up by three series – connected battery cells connected to a battery tester system from Forex, as presented in Table 8-2.

Brand	Forex
Model	Tester 12V420A
Voltage	12 V
Current	Continuous: 160 A Max: 420 A
Communication	RS232

Table 8-2: Battery tester used during laboratory testing A.

As accumulator voltage will be in the range 432 V – 600 V during operation, there is a potential problem in regards to using cells with 90 A pulse current rating. When accumulator voltage drops under 472.2 V, the battery can no longer supply 85 kW to the motor without exceeding the datasheet values for pulse current discharge. This corresponds to a cell voltage 3.28 V per cell. The main purpose of this test is therefore to obtain an equivalent electrical resistance of the cells when subjected to elevated DC currents.

The cells were tested using two basic load situations.

	Topology	Current
Test A-1	Pulse discharge	60 – 120 A
Test A-2	Continuous	Avg. 30 A

Table 8-3: Description of load situations applied during test A.

The main purpose of test A-1 is to measure the voltage drop of the cell during pulses of elevated currents up to 90A and duration of 2 seconds. Using the recorded voltage drop and current, an equivalent internal resistance can be modelled and further used to evaluate the use of cells rated for lower discharge currents in a 144S2P battery system supplying 85 kW of burst power. The purpose of test A-2 is to evaluate the developed heat in the battery when applying a constant current representing average current during an endurance race at full power.

Figure 8-1: Forex battery tester used for Test A

Figure 8-2: Connection of battery cells during tests A-1 and A-2.

8.3. Test B: Charge time and Battery efficiency

8.3.1. Introduction

As explained in chapter 2.10, the capacity of an electrochemical cell is dependent on the discharge current to which it is subjected. This relation is explained by Peukert's law. For some batteries this phenomenon can reduce the actual available capacity significantly compared to the capacity at rated current. The Simulink library block used to dimension the battery system does not account for the Peukert's effect, thus introducing an inaccuracy in the dimensioning tool developed for this master thesis work. To evaluate the implications of the Peukert's effect in the lithium – ion – polymer batteries chosen, tests subjecting the batteries to elevated constant currents are set up and analyzed. The Peukert's coefficient found through these tests is implemented in another load setup, where the capacity during a racing situation load curve is evaluated.

Charging time is strictly dependent on the design of the battery and the charging situation. Batteries designed with elevated C – ratings will complete saturation charge quicker than batteries designed for low drain. The charge time is a crucial factor for electrical vehicles and is evaluated using the same test set up. Several different charging set ups are evaluated with focus on total charging time and available capacity. As described in chapter 2.11 the depth of discharge has a significant impact on the cyclic lifespan. Altering the DOD can be done by cutting the discharge current prior to battery depletion, or by stopping the charge at a SOC < 100 %. This last aspect is evaluated in this test B-1, together with the charge current. All tests in this section are operated with the Maccor battery – testing equipment, Series 4200, described in Table 8-5.

As the Maccor battery – tester is the property of SINTEF Materials and Chemistry, only four channels could be made available. This limits the maximum test – current to 60 A, thus resulting in the simulated load curve needing further modification. To adapt the load curve to the test-restrictions, all power peaks corresponding to a pack drain of > 60 kW are modified down to 60 kW. The new variable load curves are described in Table 8-4.

	Load curve B	Load curve A
Avg. power	26.924 kW	26.400 kW
Avg. current @ V_{nom}	50.570 A	49.587 A
Avg. current for single cell @V_{nom}	25.285 A	24.793 A

Table 8-4: Description of modifications on load curve to adapt load to test – equipment.

Figure 8-3: Maccor series 4200 testing equipment used during tests B and C.

Current per channel [A]	Max. system current [A]	Min. voltage [V]	Voltage range [V]	Max. charge power [kW]	Max. discharge power [kW]	Min. step time [µs]
15	240	-2	-2 to + 8	2,4	2,4	10

Table 8-5: Maccor series 4200 battery – testing equipment description.

Cell type B is used during all tests in both test section B and C.

8.3.2. Test B-1: Evaluating charge conditions

Theory from chapter 2.11 indicates that reducing the voltage stress on the electrodes of the battery increase cyclic lifespan. Also reducing the starting SOC of the battery can have a positive impact on the cycle life. To evaluate the difference in available capacity at various relevant charging situations, tests are performed at charging situations described in Table 8-6, at discharge condition 3.0 V @0.5 C.

Test	Charge current [A]	Charge Voltage [V]	Saturation charge
B1-1	1 C	4.2	<0.35A
B1-2	1 C	4.2	No
B1-3	1 C	4.1	<0.35A
B1-4	1 C	4.1	No
B1-5	0.5 C	4.2	<0.35A

Table 8-6: Charging efficiency and time evaluation. Test situations overview.

8.3.3. Test B-2: Battery efficiency

To properly evaluate the LCO – cells correspondence to Peukert's law, several tests using constant discharge current over 100% DOD at different current ratings within the battery's C – rate are applied. Table 8-7 presents an overview of the test situations.

Test	Discharge current [A]	Cut - off Voltage [V]
B2-1	0.5 C	3.0
B2-2	1 C	3.0
B2-3	2 C	3.0
B2-4	3 C	3.0
B2-5	4 C	3.0
B2-6	6 C	3.0
B2-7	8 C	3.0
B2-8	Load- Curve A	3.0

Table 8-7: Battery efficiency tests, load situations overview

8.4. Test C: Battery cycle life test

8.4.1. Introduction

Estimating the battery life for an EV battery system depends on many factors, as attended to in chapter 2.11. However, as the EV battery – system is subjected to a load situation that stands out from normal use of lithium batteries, some factors are still unmapped and the effects of which are hard to predict. In these tests the implications of operating the battery in a variable load situation are evaluated. Data from [35] indicate that allowing the battery resting time during discharge positively affects cyclic lifespan. As the majority of the discharge cycles the EV – battery system are performed in a testing environment, the cells will not be continuously discharged to 100% DOD. Instead, the cells are discharged with prolonged resting time in between cycles. The second set of cyclic lifespan tests will attend to the natural rest time experienced by the battery when the EV is at a standstill.

8.4.2. Test situations

Two test situations are set up to evaluate the effect of the variable load curve and natural breaks during discharging of the lithium – ion battery. As the simulated load curve is lap - based, a rest time of 30s is introduced after each lap, corresponding to a pause of 30s after 85s discharging.

Test	Cell	Charge current	Charge Voltage [V]	Load description	Discharge voltage [V]
C-1	C1	0.5 C	4.2	Load curve A	3.0 V
C-2	C2	0.5 C	4.2	Load curve A, 20s rest every 85s	3.0 V

Table 8-8: Test situation description for test C-1 and C-2

As the voltage drop over the cell at elevated currents can be substantial, it is likely that there is still significant amount of charge in the battery still remaining when it first drops to 3.0 V. As comparison to the 100 % DOD performance tests supplied by the manufacturer is important for this analysis, the voltage is checked at 0.5 C discharge current to ensure that the cell is discharged at a DOD equal to the performance tests received from the manufacturer. The test set up for test C2 is visualized in the flow chart in Figure 8-4.

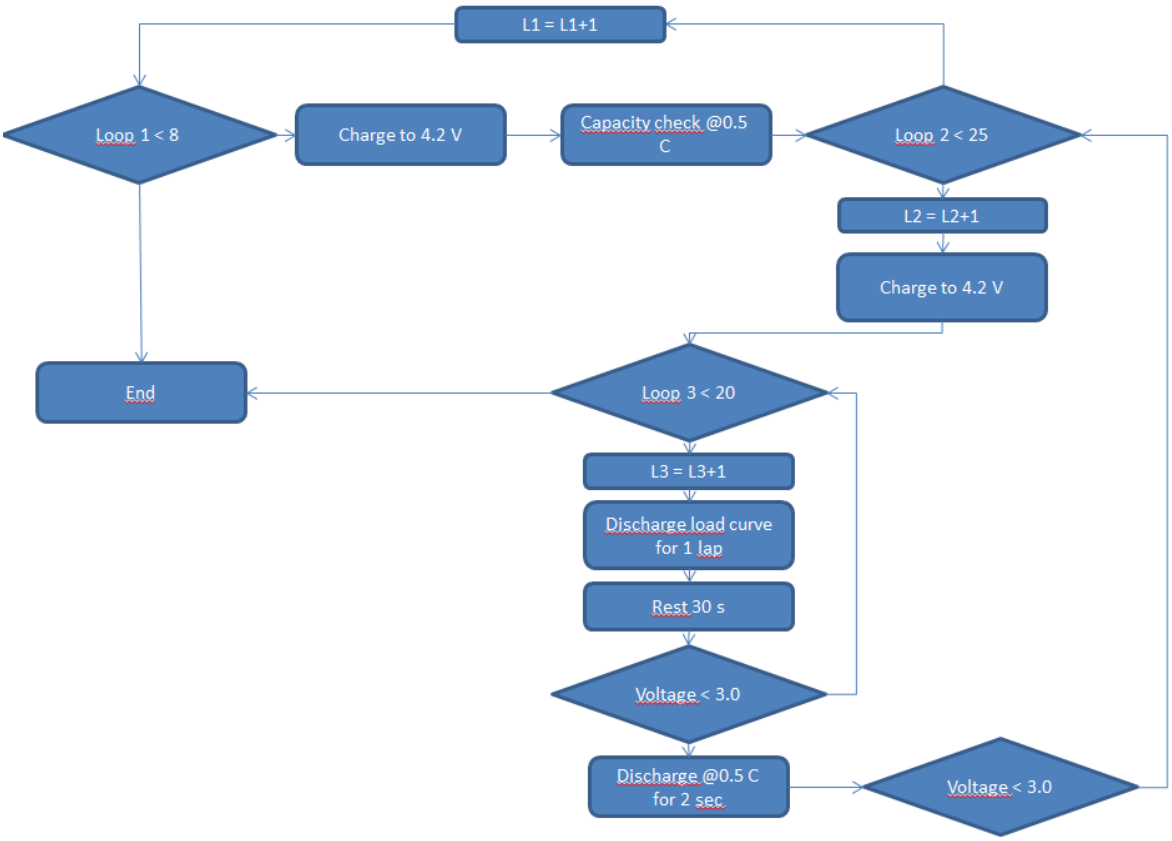

Figure 8-4: Flow chart explaining the test setup cyclic lifespan test, C-2.

9. Results – Battery cell testing and simulations

9.1. Single cell laboratory tests

9.1.1. Test A: C – rating evaluation

9.1.1.1. Test A-1: Pulse discharging

The recorded current pulse from one of the tests performed is visualized in Figure 9-1. Voltage curve from the same test is shown in Figure 9-2.

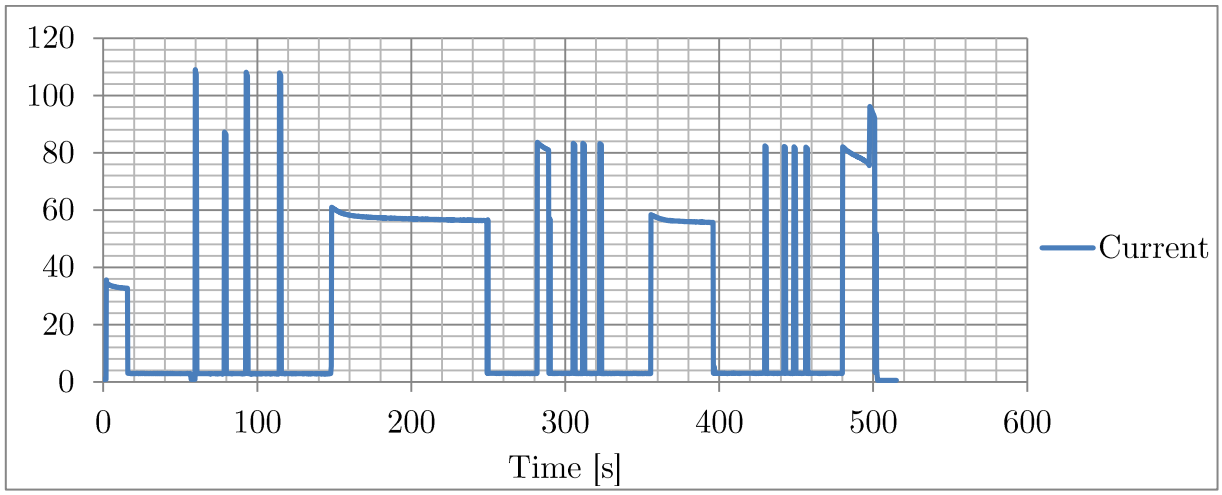

Figure 9-1: Current over time plot from test A-1: Elevated current pulses on cell type A. Secondary axis given in [A]

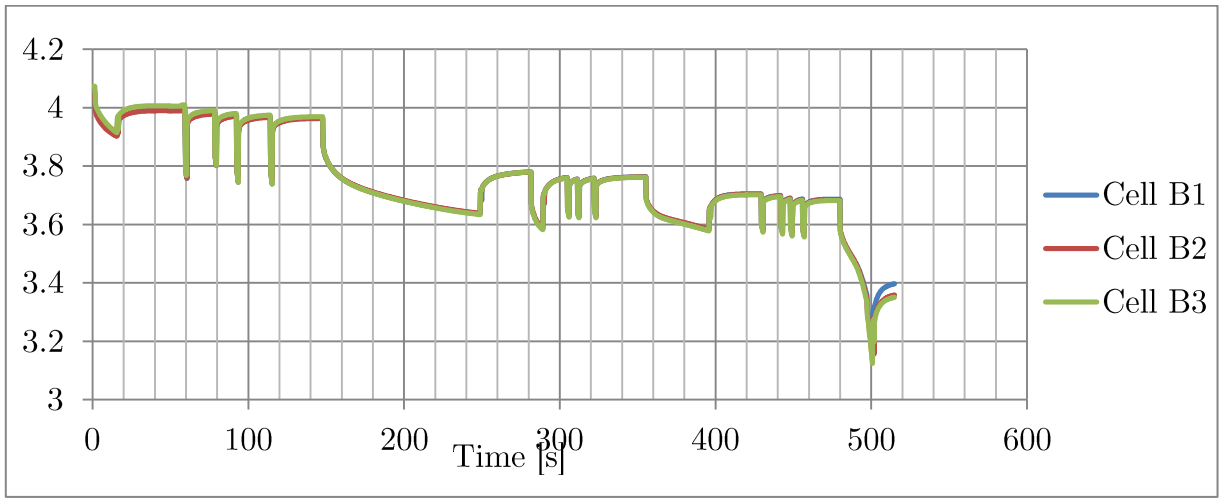

Figure 9-2: Voltage over time plot for one of the tests performed during test A-1. Cells B1, B2 and B3 are evaluated. Secondary axis given in [A]

The complete results can be found in appendix D. Voltage drop for a representative selection of the test results is summarized in Figure 9-3 and the corresponding average electrical resistance found is presented in Table 9-1.

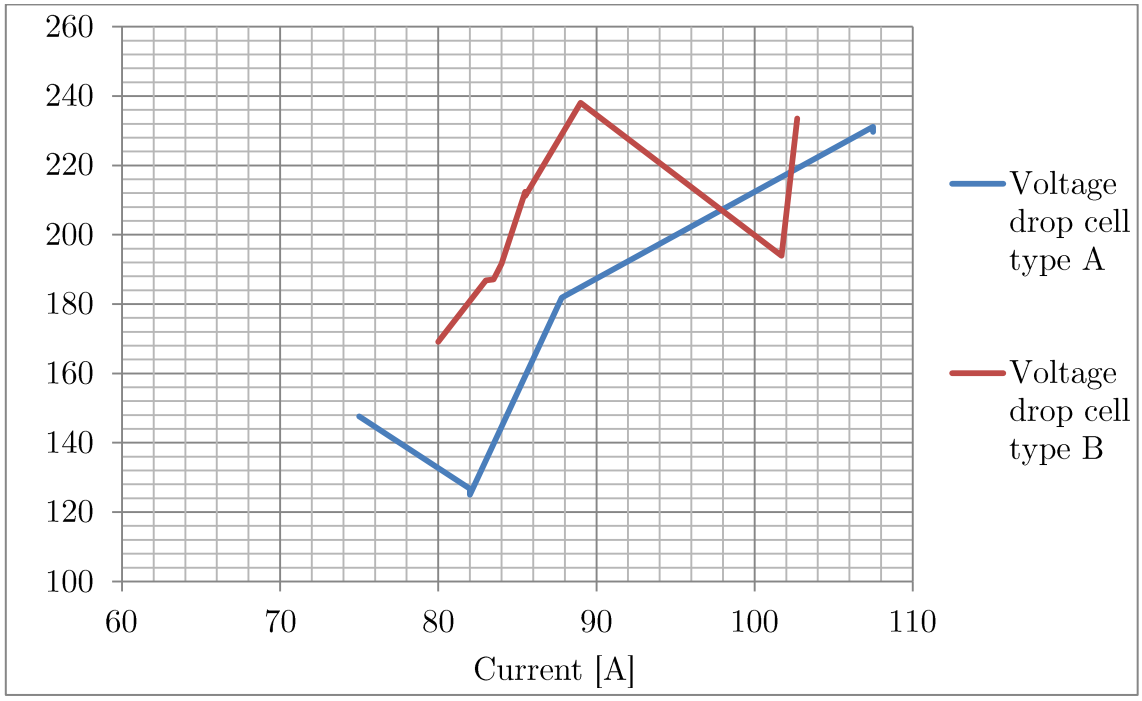

Figure 9-3: Voltage drop for current pulses with various magnitudes. Duration of current pulses is 2s. Secondary axis given in [mV]

	Average equivalent internal resistance $[m\Omega]$
Cell A	1.899
Cell B	2.230

Table 9-1: Calculated electrical resistance based on current step response of the battery cells of type 1 and 2

9.1.1.2. Test A-2: Temperature during constant current discharge

Cells are subjected to a constant current. The recorded current and temperature from one of the tests performed are visualized in Figure 9-4 and Figure 9-5.

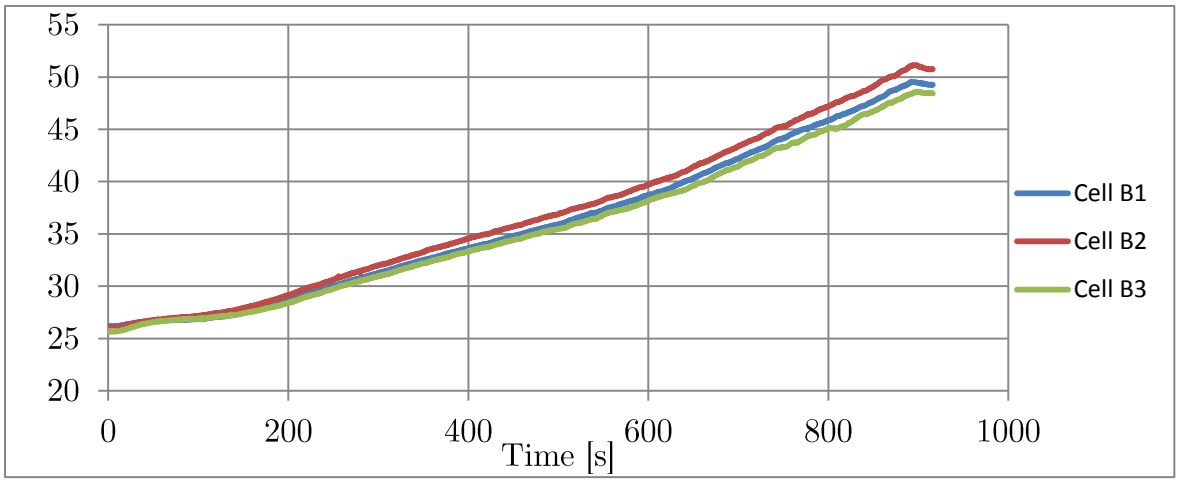

Figure 9-4: Temperature development over time during test A-2. Secondary axis is given in [°C]

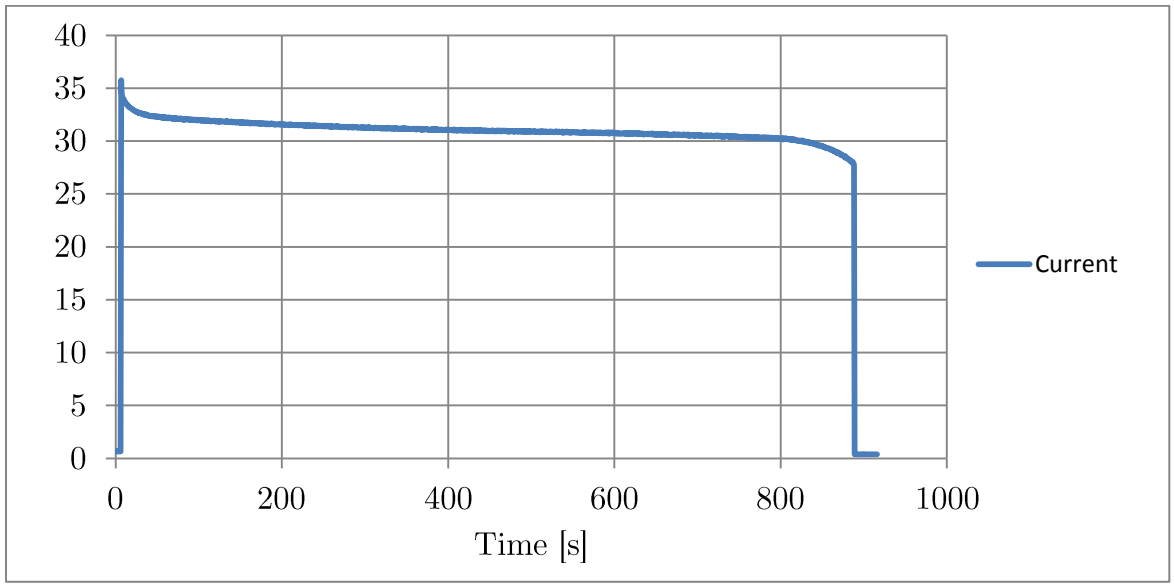

Figure 9-5: Current over time during test A-2. Secondary axis given in [A].

The results presented in Table 9-2 show the calculated heat dissipation based on both real – time data and average current. In order to compare the performance, a parameter based on temperature per energy and time is defined as shown in equation(7.6). Complete results can be found in appendix E.

$$\kappa = \frac{\Delta T}{\Delta t \cdot J_{tot}} \tag{7.6}$$

Cell type	Avg. Temp Increase [K/(min x kJ)]
B	1.3655
A	1.7336

Table 9-2: Summary of results from test A-2, temperature increase during constant current discharge.

9.1.1.3. Test A-3: Temperature during variable load discharging.

Based on the results from test A-2, further temperature testing is performed on cell B. Temperature is monitored during 100% DOD discharge using the variable load curve from chapter 5.2. Figure 9-6 and excerpt of these tests and illustrate how the temperature, voltage and current developed with time during test -A3. For comparison, a continuous discharge from test A-2 is plotted in the figure, following the variable load discharge and one charge cycle.

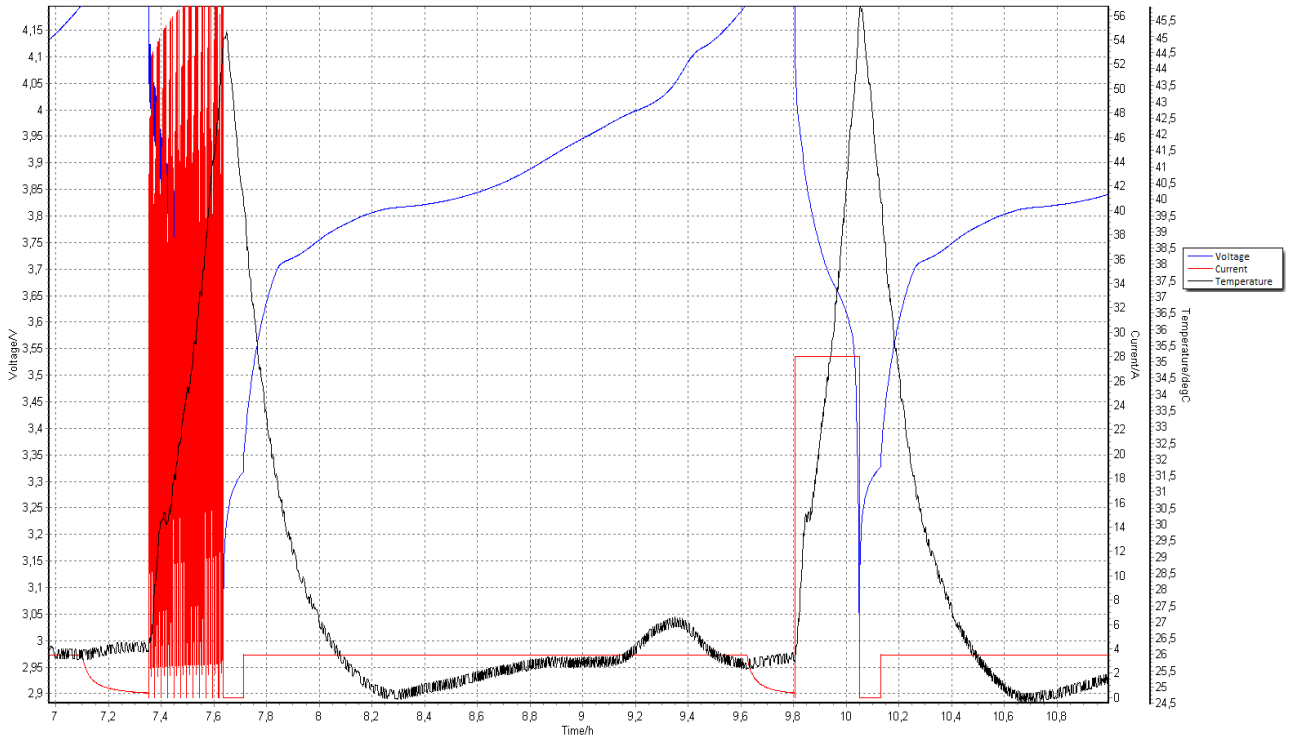

Figure 9-6: Test A-3, temperature during variable load discharge, 0.5 C charging and 6 C constant current discharge. Current (red), voltage (blue) and temperature (black) are represented on the second axis, and time on the primary axis.

The variable load situation with an average current of 3.54 C show a slightly more moderate temperature development when compared to the 4 C constant current

discharge. It can also be seen that charging the battery at a low SOC is a strict endothermic reaction, drastically lowering the temperature of the battery.

9.1.2. Test B: Charge situations and battery efficiency

Three cells of type B were used during these tests. An overview of the cell used and the test numbering is found in Table 9-3. Capacity is measured in Ah in this analysis.

Test	Type	Cell
B1-1	Charge situations	B4
B2-1	4C, 8C and Load curve	B4
B2-2	1C, 2C, 3C, 6C	B5
B2-3	Load curve A	B6
B2-4	Load curve A, with rest between discharges	B5

Table 9-3: Test B situation overview.

9.1.2.1. Test B-1: Charge situations

Results from tests according to the charge situations described in Table 9-3 are presented in Table 9-4

Test	Charge current [A]	Charge Voltage [V]	Sat. charge	Charge time [s]	Charge capacity [Ah]	Discharge capacity [Ah]	Efficiency	Cell
B1-1	1 C	4.2	<0.35A	1:08:58	7.098	7.064	99.52%	B4
B1-1	1 C	4.2	<0.35A	1:08:35	7.083	7.080	99.96%	B4
B1-1	1 C	4.2	-	58:15:46	6.796	6.791	99.93%	B4
B1-1	1 C	4.2	-	58:00:57	6.767	6.763	99.94%	B4
B1-1	1 C	4.1	<0.35A	1:08:45	6.411	6.407	99.94%	B4
B1-1	1 C	4.1	<0.35A	1:08:00	6.395	6.392	99.94%	B4
B1-1	1 C	4.1	-	52:13:22	6.092	6.089	99.95%	B4
B1-1	1 C	4.1	-	52:04:79	6.075	6.073	99.97%	B4

Table 9-4: Results from test B1, charge situation tests.

The average decrease in available capacity found when charging the battery to 4.1 V with saturation charge is 6%. Charge time is cut by approximately 10 minutes when dropping saturation charge. It is also noticed that charging the battery with saturation charge to 4.1 V and 4.2 V does not affect charging time noticeably.

9.1.2.2. Test B-2: Battery efficiency

At 1 C full charge, the tests are subjected to eight different load situations. Figure 9-7 show voltage and current plots from parts of test B2-1.

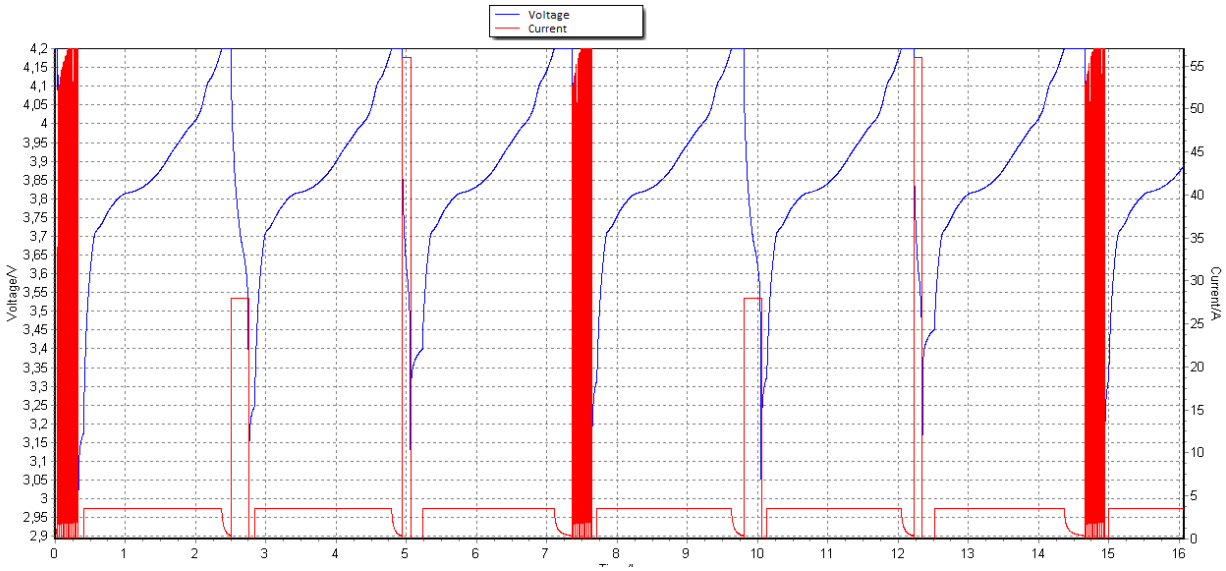

Figure 9-7: Voltage and current plots for tests performed at 4 C, 8 C and load curve A. Voltage(blue) and current(red) are represented on the secondary axis, and time on the primary. Both charge and discharge current is defined as positive current although the flow of charge is reversed in the two situations.

The plots in Figure 9-8 visualizes the calculated Peukert's coefficient from test B2. A summary of the results can be viewed in appendix G.

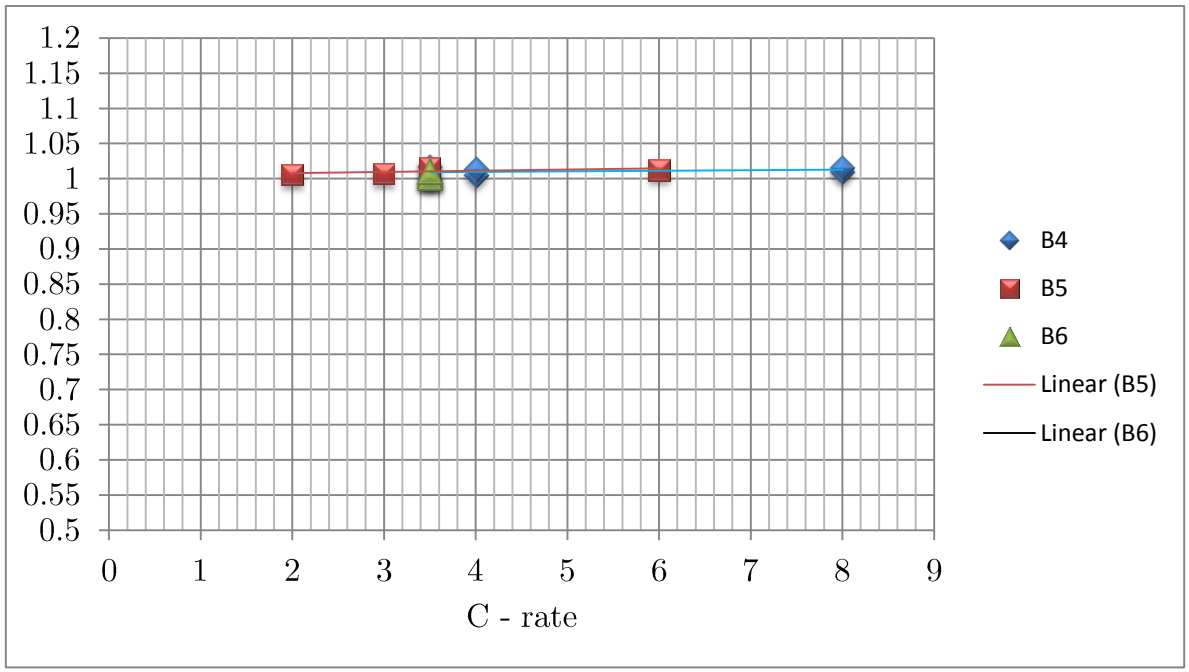

Figure 9-8: Dispersion plot of calculated Peukert's coefficient for battery cells B4, B5 and B6. Linear (B5) and (B6) are generated as a linearization of the dispersed data. Secondary axis shows the Peukert's coefficient.

Figure 9-9 show a dispersion plot of the battery efficiency compared to a reference discharge performed for each of the battery cells. Complete results can be viewed in appendix G.

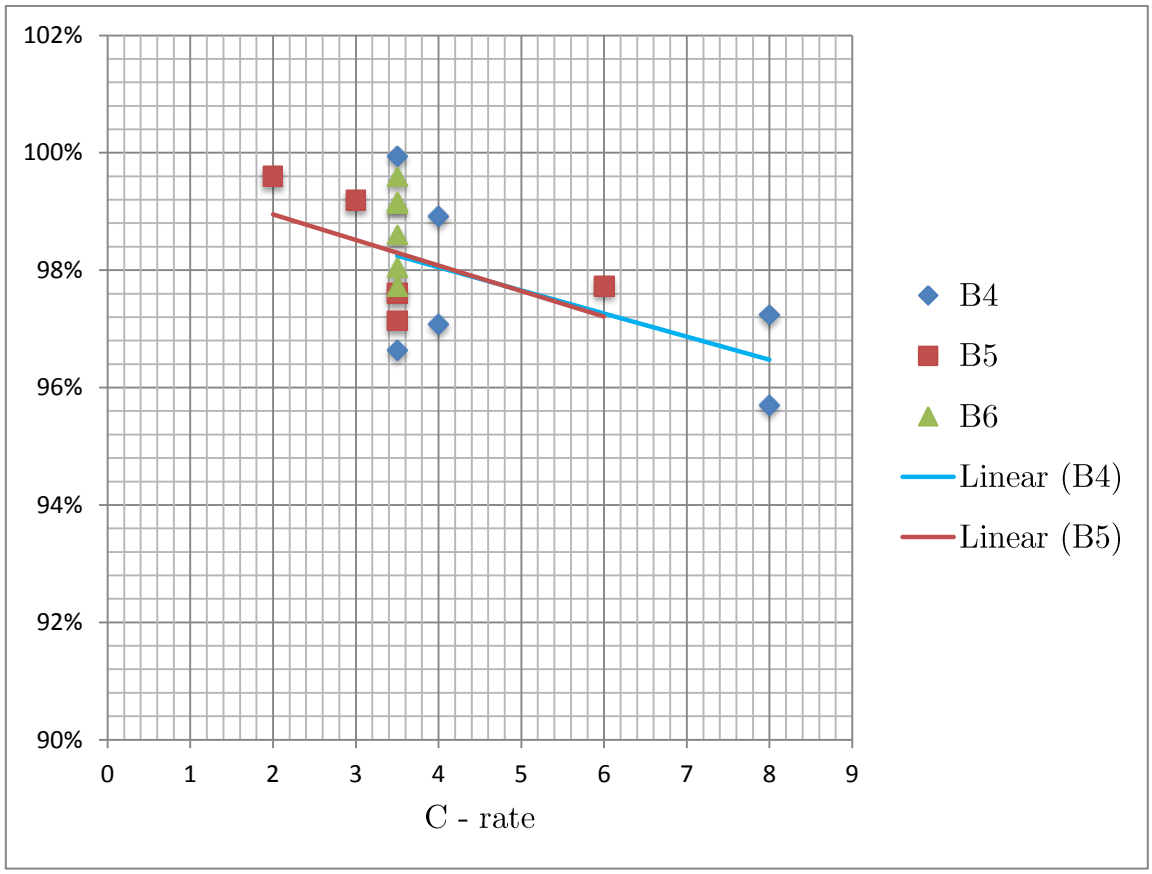

Figure 9-9: Battery efficiency over C –rating for battery cells B4, B5 and B6. Linear (B5) and (B6) are generated as linearized from the dispersed data. Secondary axis gives efficiency in [%].

In both Figure 9-9 and Figure 9-10 the load curve situation is represented by its average current, corresponding to 3.5 C.

9.1.3. Test C: Cycle life evaluation

9.1.3.1. Test C-1: Cycle life with variable load

Cycle life tests are performed based on the load curve first presented in chapter 5.2. and further modified in chapter 8.3.1. The test is set up with a complete discharge at 0.5C to evaluate the initial capacity of the battery at rated conditions at cycle 1. This capacity check is repeated after every 25th complete variable load cycle thereafter. The graphics in Figure 9-10 show the capacity fade during the cyclic life of the battery. The test is ended after 125 cycles to allow time for test C-2. The charge capacity received by the battery strongly depends on the SOC at cut – off and varies during with increasing cycles. It can be seen that the received capacity after each capacity check is elevated compared to the situation before. This can be

explained by the increased stability and reduced Peukert's effect during the 0.5 C discharge capacity checks.

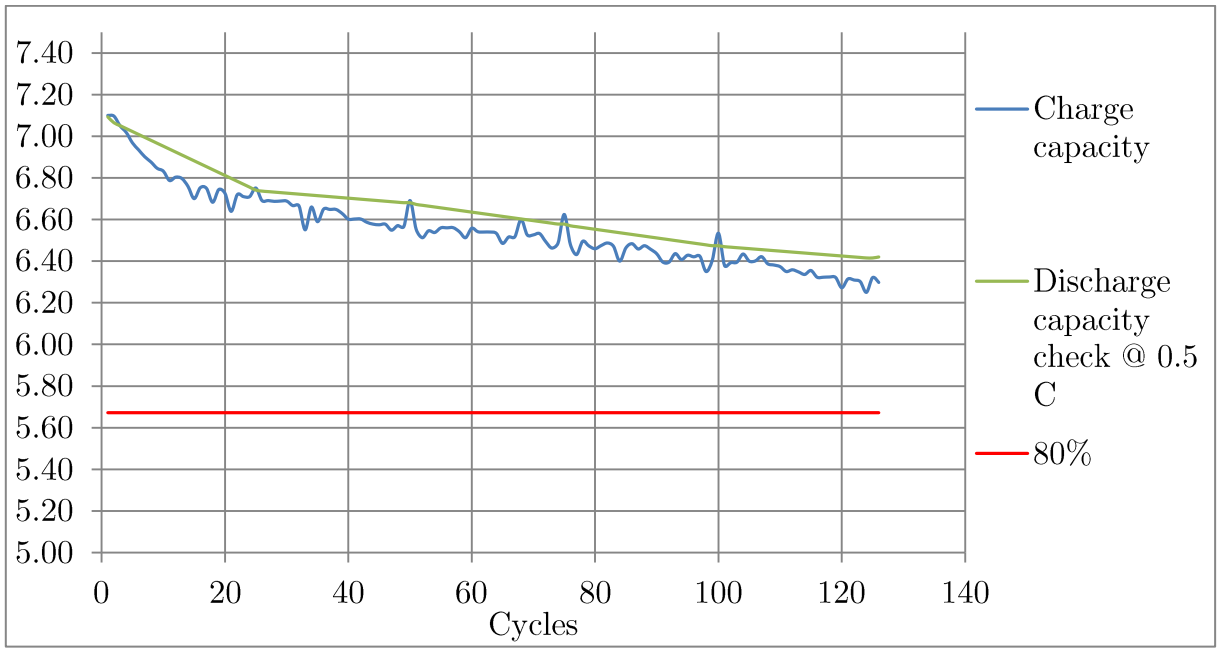

Figure 9-10: Cycle life test with variable load and no pause, according to test C-1. Blue curve represents charge capacity along the cycle life, green curve is a linearization of the discharge capacity checks each 25th cycle. Secondary axis represents capacity in [Ah].

9.1.3.2. Test C-2: Cycle life with variable load and rest during discharge

Previous experimental work cited in chapter 2.11 indicates that implementing a resting time of 20s between each simulated lap could increase cyclic lifespan of the battery. Figure 9-11 present the results compared to the identical load tests without rest time.

Because of time constraints and a program error, the test could only complete 103 cycles. The program error is elaborated in appendix K.

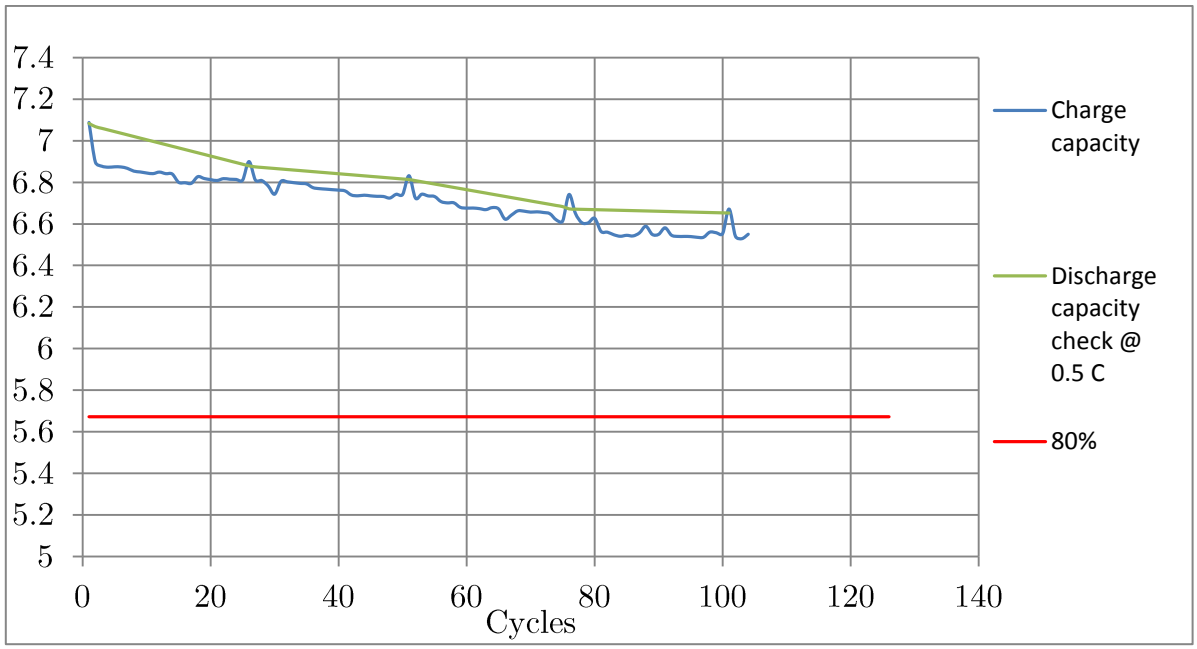

Figure 9-11: Cyclic lifespan evaluation using load curve A with an implemented 20s rest after each 85s discharge. Secondary axis represents capacity in [Ah].

9.2. Simulink simulations

9.2.1. Introduction

The Simulink model presented in chapter 5.3 is used to simulate the battery behavior corresponding to the tests from Test B. In addition, the model is used to evaluate the required capacity of the complete battery system.

9.2.2. Single cell simulations and configuration of the Simulink model

To evaluate the available energy at 0.5C after the cut-off voltage is first reached, the Simulink extension presented in chapter 5.3.2 is used. Voltage vs time curve when simulating with load curve A and evaluation remaining energy is shown in Figure 9-12.

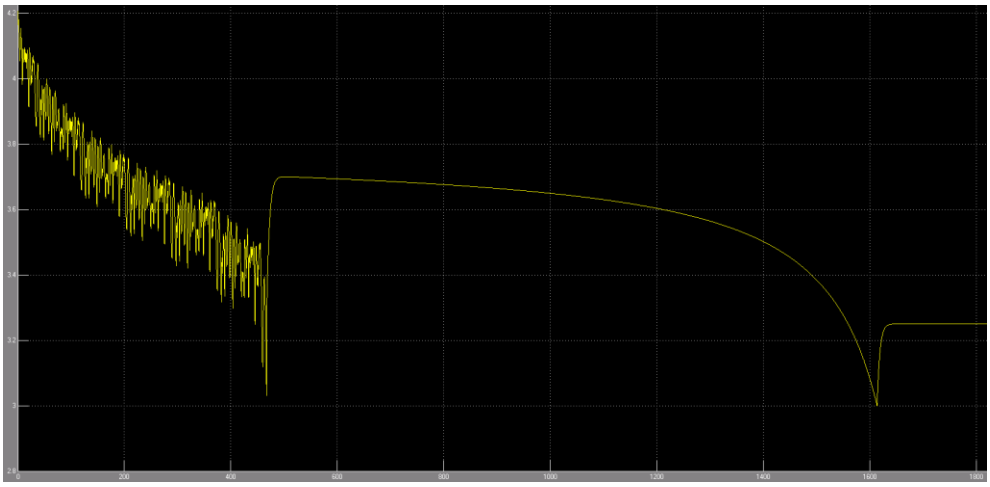

Figure 9-12: Voltage vs time curve for the Battery block from simulation at 100 % DOD using the reduced load curve and discharging the remaining energy at 0.5C when cut – off voltage is reached.

Simulation discharge conditions during these tests are presented in Table 9-5.

Test	Charge voltage [V]	SOC at start	Cut - off voltage [V]	Current
S1	4.2	100.00%	3	1 / 2 C
S2	4.2	100.00%	3	1 C
S3	4.2	100.00%	3	2 C
S4	4.2	100.00%	3	3 C
S5	4.2	100.00%	3	4 C
S6	4.2	100.00%	3	6 C
S7	4.2	100.00%	3	8 C
S8	4.2	100.00%	3	Load curve
S9	4.2	100.00%	3	Reduced load curve

Table 9-5: Simulation condition S1-S9 for comparison with single cell tests in B2 and configuration of the battery block.

To calculate the losses due to dissipated energy in the equivalent internal resistance of the battery for the constant current simulations, equation (9.2) is utilized.

$$W_{loss} = P_{loss} \cdot t = R_{internal} \cdot i^2 \cdot t \qquad (7.7)$$

For the variable load situation, losses are based on linearization of the current from the load curve. Since the load curve data is given in power, the nominal voltage of

3.7 is used to estimate the current in the battery cell at each time-step. Equation (9.3) show the linearization technique used

$$f(t_n + \frac{\Delta t}{2}) = f(t_n) + \frac{(f(t_{n+1}) - (t_n))}{2} \tag{7.8}$$

Where Δt is the time-step between data – set values given by the load curve vector. The results from simulations with the initial configuration, configuration 1, of the model is presented in

Test	Discharge time [s]	Discharge capacity [Ah]	Discharge energy [Wh]	SOC @cut off	Energy loss due to dissipation [Wh]	Total energy [Wh]
S1	7601.7	7.391	28.178	1.46%	0.052	28,230
S2	3782	7.354	27.909	0.48%	0.103	28.021
S3	1872	7.282	27.386	1.47%	0.204	27.742
S4	1235	7.203	26.874	2.50%	0.303	27.495
S5	916	7.123	26.368	5.02%	0.399	27.271
S6	596.2	6.954	25.366	5.82%	0.584	26.877
S7	435.4	6.771	24.362	8.26%	0.759	26.542
S8	1062.4	6.989	25.978	5.35%	0.457	27.362
S9	1053.1	7.121	26.344	3.59%	0.469	27.254

Table 9-6: Simulation results S1-S9 using configuration 1.

The deviation in available energy for elevated current discharge compared to lower current is the dissipated energy due to the internal resistance and the SOC at cut off. From comparison between test – results in chapter 9.1.2.2 and Table 9-6 it is evident that configuration 1 of the Simulink block leads to an unrealistic amount of energy being stored in the battery following an elevated current discharge. To account for this, the battery block is reconfigured to configuration 2. The results from the situation S1 – S9 are presented in Table 9-7. See appendix A for further explanation of the configuration.

Test	Discharge time [s]	Discharge capacity [Ah]	Discharge energy [Wh]	SOC @cut off
S1	7293.5	7.091	26.953	0.129%
S2	3645.2	7.088	26.880	0.173%
S3	1821.0	7.081	26.737	0.263%
S4	1212.9	7.075	26.595	0.358%
S5	908.8	7.068	26.453	0.456%
S6	604.6	7.053	26.168	0.668%
S7	452.4	7.036	25.882	0.902%
S8	1081.8	7.072	26.443	0.398%
S9	1053.8	7.063	26.388	0.523%

Table 9-7: Results from simulations performed applying configuration 2.

Based on the results shown in Figure 9-8 , the model is further modified with a Peukert's coefficient of 1.012, found in chapter 9.1.2.2. The block configuration is identical to the case in configuration 2, but the model is extended as elaborated in chapter 5.3.3. The results are presented in Table 9-8.

Test	Discharge time [s]	Discharge capacity [Ah]	Discharge energy [Wh]	SOC @cut off
S1	7293.5	7.091	26.953	0.129%
S2	3645.2	7.029	26.880	0.173%
S3	1821.0	6.964	26.737	0.263%
S4	1212.9	6.924	26.595	0.358%
S5	908.8	6.893	26.453	0.456%
S6	604.6	6.844	26.168	0.668%
S7	452.4	6.804	25.882	0.902%
S8	1081.8	6.893	26.443	0.398%
S9	1053.8	6.887	26.388	0.523%

Table 9-8: Configuration 3, implementing the Peukert's coefficient in to model the effective current through the battery.

9.2.3. Capacity evaluation

To represent the complete battery system, the battery model is configured according to configuration 3, appendix A. Based on the chosen manufacturer portfolio, there were five cell - designs considered suitable for the accumulator – system. Applying the 144S2P configuration, complete battery systems constructed from the alternatives are presented in Table 9-9. The discharge time represents the total amount of time available at the developed load – curve B for each system.

	Type A	Type B	Type C	Type D	Type E
Cell capacity [Ah]	6.20	7.00	6.35	6.00	8.00
Energy [kWh]	6.70	7.46	6.77	6.39	8,52
Weight [kg]	37.87	38.88	39.17	36.57	58.03
Volume [l]	16.65	17.11	18.11	15.73	19.17
Specific weight [Wh/kg]	176.9	191.9	172.8	174.7	146,82
Specific volume [Wh/l]	402.4	436.0	373.8	406.2	444,44
Continuous current rating [A]	186	112	190.5	120	560
Discharge time [s]	929,725	1052,76	934.7	883.85	1209.77
Available energy @ load curve B [Wh]	6723.88	7587.53	6767.71	6371.82	8736.39

Table 9-9: Energy and weight data for the relevant cell alternatives and Simulink simulation results regarding available discharge time in load curve B discharge situation.

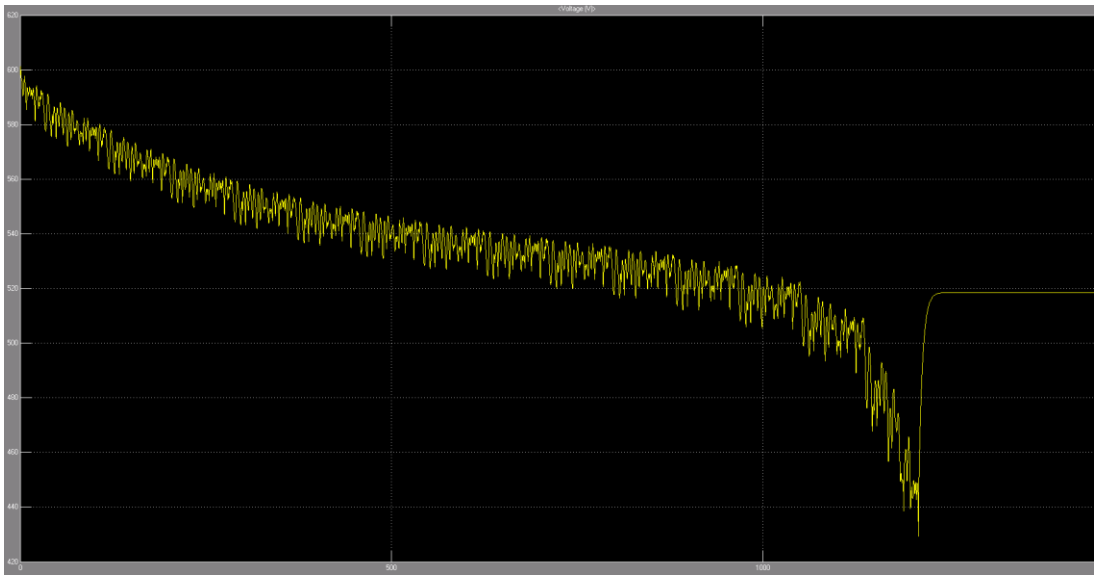

Figure 9-13: Battery system voltage over time from simulation using cell alternative number 5 and load curve A.

9.2.4. Cut – off voltage

Simulations are performed with focus on the impact of increasing the cut – off voltage from 3.0 V.

Increasing the cut-off voltage reduces the available discharge time. Figure 9-14 shows the discharge time as a function of cut – off voltage for simulations with configuration 1 and 3, as well as test results when cell B4, B5 and B6 are discharged with load curve A. A complete summary of these results can be found in appendix F.

	Simulation, config. 3	Test B4	Test B5	Test B6
Change in discharge time	-0.135%	-1.915%	-1.186%	-3.014%

Table 9-10: The effect of increasing cut off – voltage from 3.0V to 3.3V when subjected to load curve A.

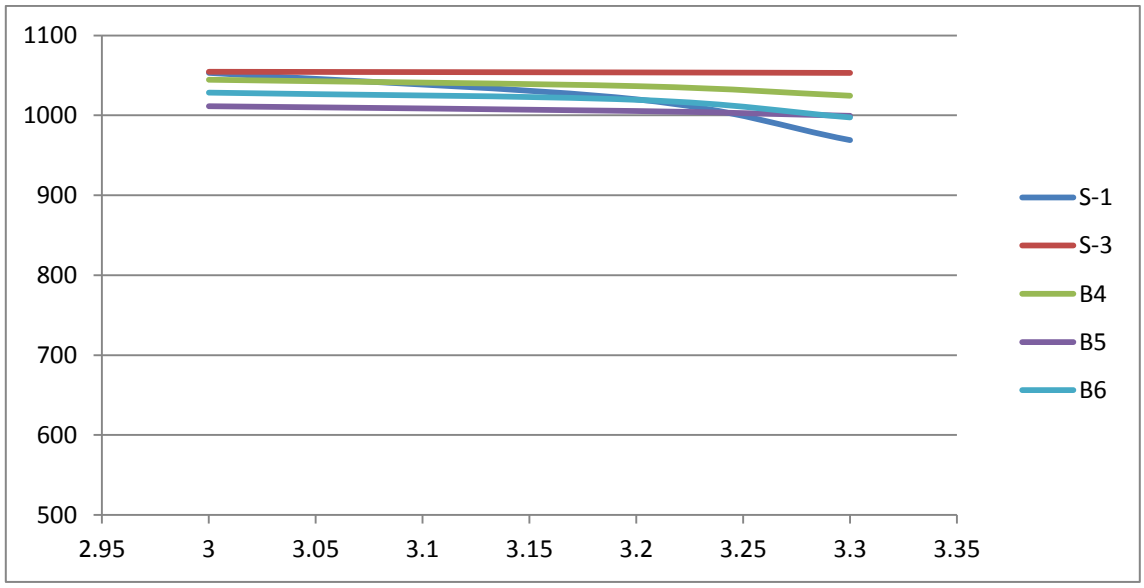

Figure 9-14: Comparison of the dependency of discharge time and altering the cut – off voltage for single cell. All 5 results are based on discharge situation @ load curve A. S -1 and S -3 are simulations with configuration 1 and configuration 3, respectively. B4, B5 and B6 represent the three different cells tested.

9.2.5. Charge conditions

To analyze the Simulink model accuracy with regards to the different charge conditions, simulations are conducted altering the battery block state of charge at the start of each simulation to correspond to the tests presented in chapter 8.3. Implementing saturation charge is not an option for the Simulink battery block. In order to model charging situation to 4.1 V, the SOC at start for the battery block is set at 93.5 %. Results are presented in Table 9-11. Configuration 3 is used for these simulations.

Test	Charge voltage [V]	SOC at start	Discharge voltage [V]	Discharge current	Discharge time [s]	Discharge capacity [Ah]
B1 – S1	4.2	100,00%	3.0	0.5 C	7293,5	7,091
B4 - S2	4,1	93.5%	3.0	0.5 C	6818,8	6.629

Table 9-11: Simulations results for evaluation of charging condition tests.

The reduction in available capacity for these two charging situations is 6,5%. Compared to the average capacity decrease found through the Simulink simulations

presented in Table 9-4, 6.0 %, the deviation from Simulink model to battery tests is 0.5%. This error is considered satisfactory.

10. Results – Tractive system tests

10.1.Tractive system test in water brake

The primary objective of the water brake tests were functionality testing and efficiency. Extensive testing with elevated load situations revealed system weaknesses. The more frequent fault was AMS communication problems and erroneous voltage measurements. A thorough review and explanation of all of the flaws revealed and rectified during these tests can be found in the appendix L.

Limited access to the water brake facilities and system failures along the testing process reduced system operation time significantly. With regards to temperature development, it was desirable to operate the system at current – levels superior to the estimated avg. current during endurance race. Due to difficulties with regulating the pump system and the motor torque request as well as the AMS shutdowns, only a handful of proper tests could be performed.

10.1.1. Temperature development in battery modules

Data that describes the accumulator system temperature behavior is necessary to determine the critical temperature in the AMS. Figure 10-1 shows temperature development in a battery module during the load test. Accumulator voltage and current for this particular test can be seen in Figure 10-3 and Figure 10-4.

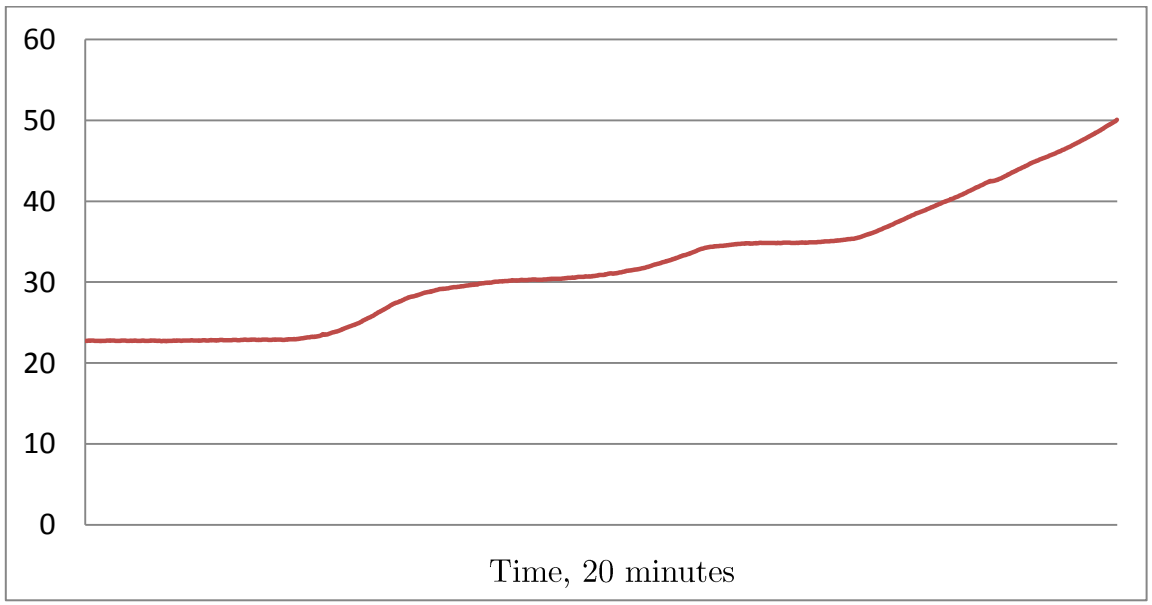

Figure 10-1: Temperature development in one of the battery - modules during the complete test. Secondary axis is given in °C.

Studying the temperature behavior in the following 20 minutes after the test is concluded, it is evident that the temperature continues to increase after shut down. This is visualized in Figure 10-2.

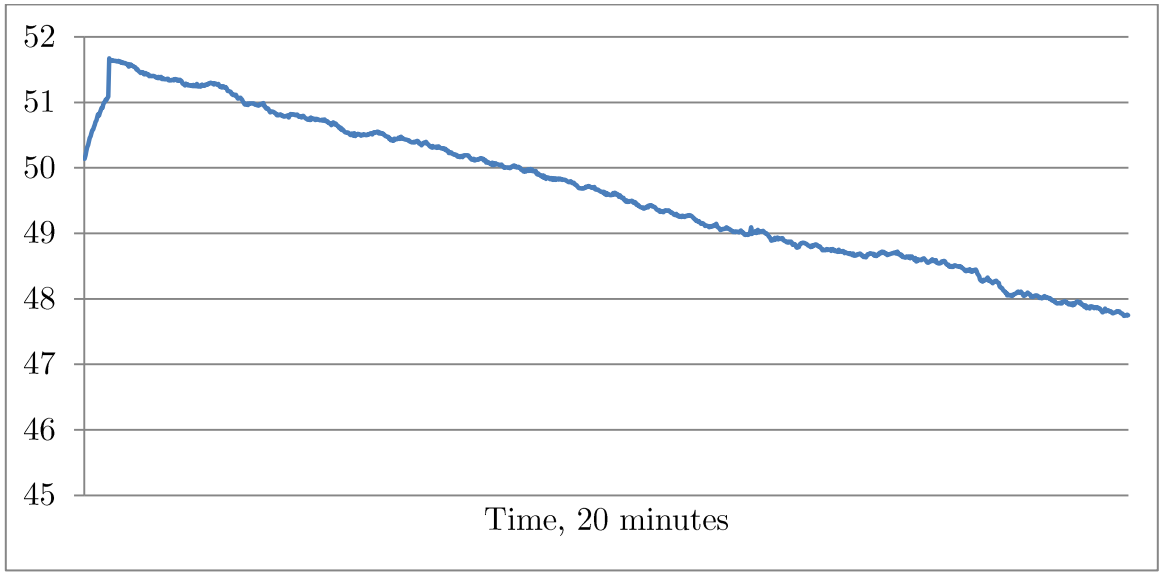

Figure 10-2: Temperature development during the 20 first minutes following the load is disconnected and current stops flowing in the system. Secondary axis is given in °C.

10.2.Current, voltage and power measurement

The current and voltage over the accumulator poles are plotted in Figure 10-3 and Figure 10-4.

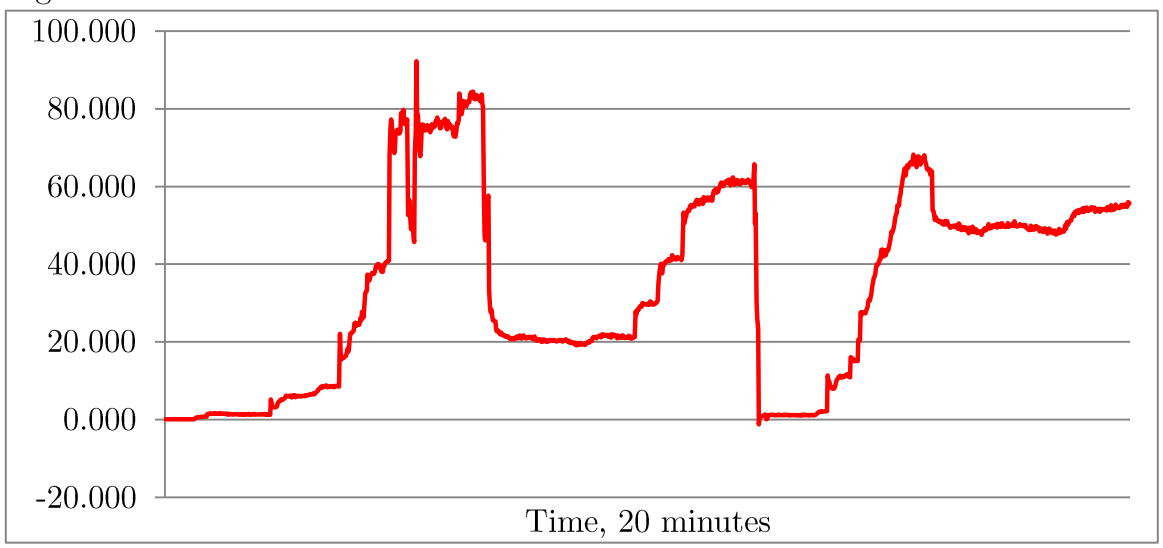

Figure 10-3: DC current from accumulator to inverter and PMSM during test. Secondary axis given in [A].

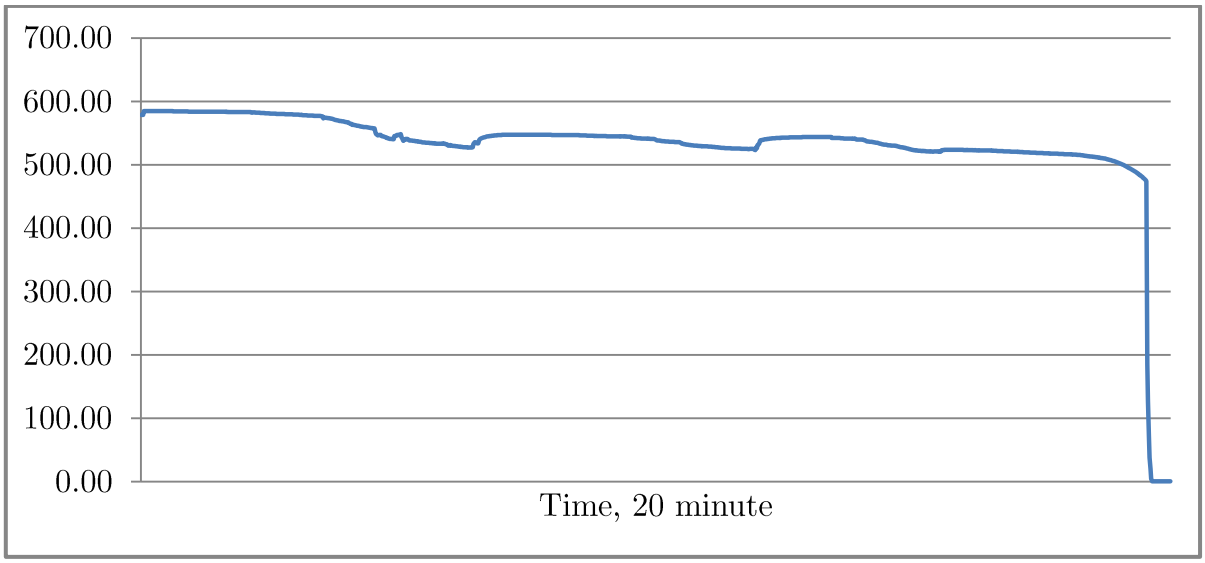

Figure 10-4: Accumulator voltage during 20 minute test. Secondary axis is given in [V].

Figure 10-5 shows plots of power delivered from the accumulator to the tractive system during the 20-minute load test.

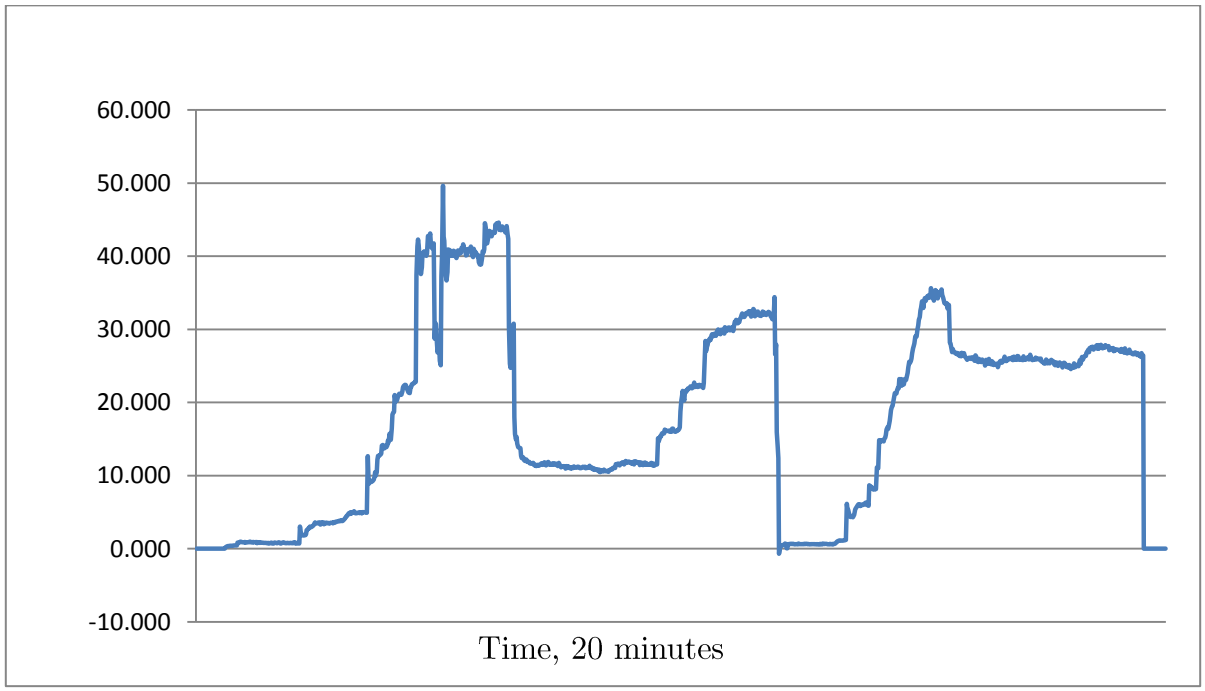

Figure 10-5: Power delivered from accumulator during 20-minute load test. Secondary axis given in [kW].

10.2.1. Water brake results

Figure 10-6 shows plots of the measured torque on the drive shaft during the 20-minute load test.

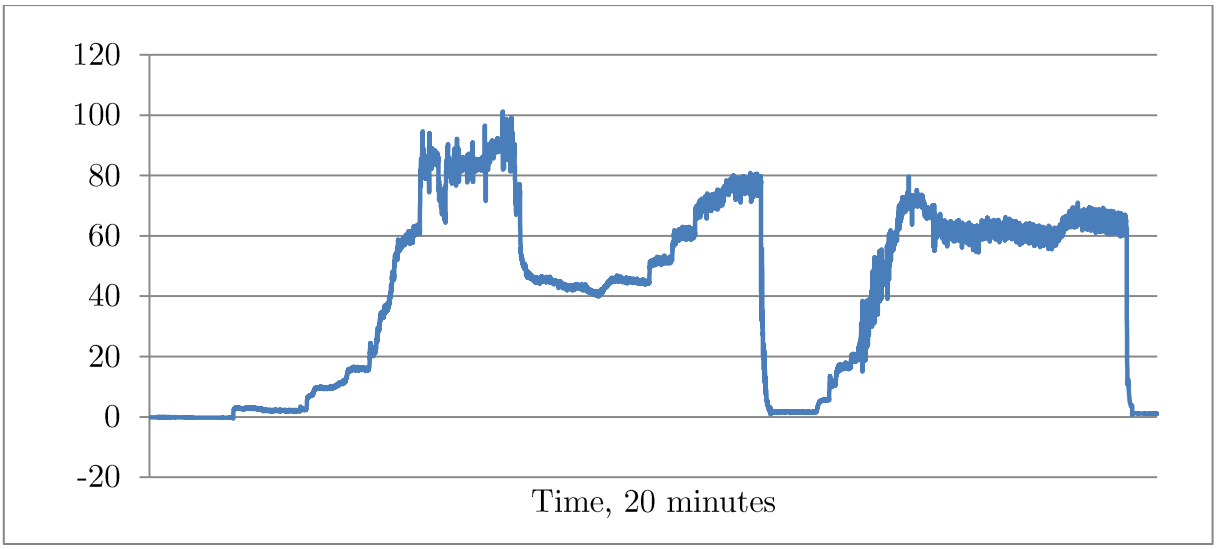

Figure 10-6: Torque measurements done on the drive shaft during the 20-minute load test. Secondary axis is given in [Nm].

Figure 10-7 shows plots of the measured shaft speed during the 20-minute load test. These measurements are considered not accurate enough to perform system efficiency calculations. This is discussed in chapter 11.4.

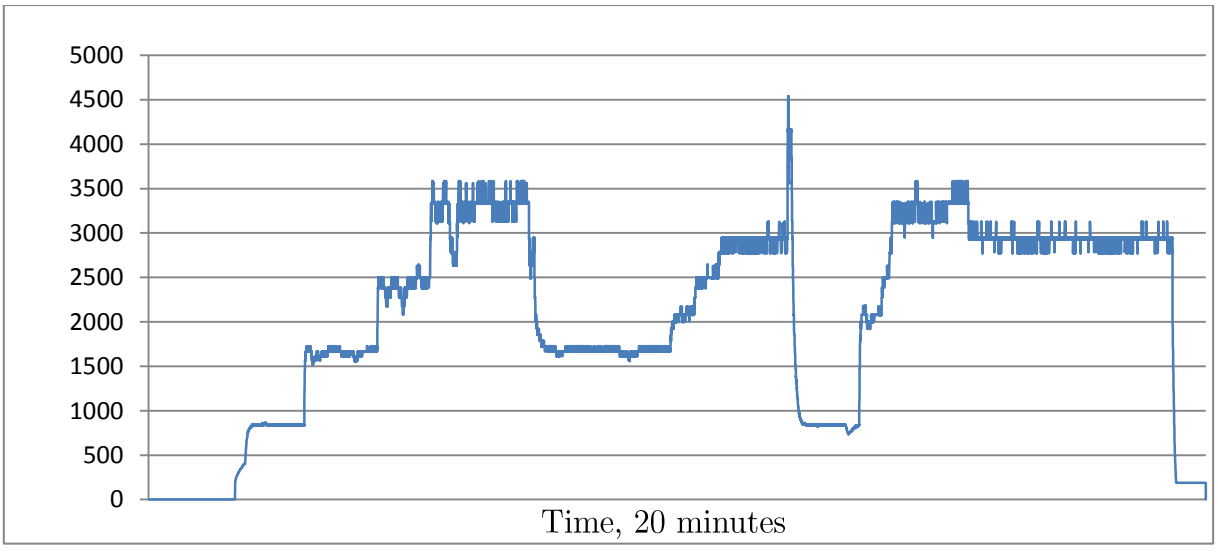

Figure 10-7: Rotor speed during the 20-minute load test. Secondary axis is given in [Hz].

10.3. Electromagnetic Interference

Initial tests powering up the inverter and recording electromagnetic radiation show a substantial increase of magnetic activity with wavelengths in the range 0 – 1 MHz with active IGBT – modules as compared to the results with the IGBT-modules deactivated. An excerpt from the results is shown in Figure 10-8.

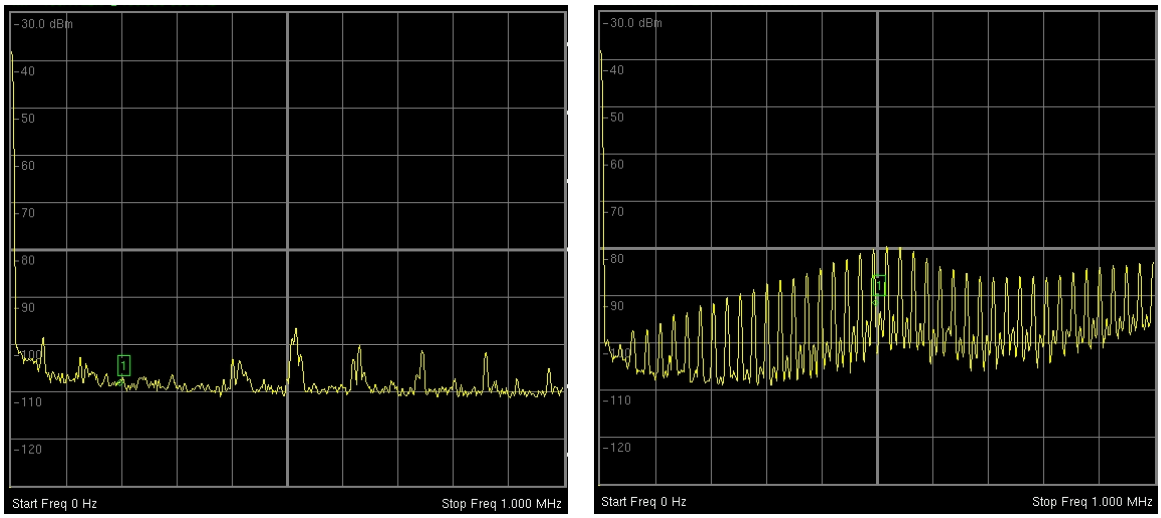

Figure 10-8: Electromagnetic radiation with IGBT – modules deactivated compared to identical test with IGBTs active. Frequency domain 0-1 MHz.

To further evaluate the frequency domain where the EMI is stronger, more tests are performed, receiving radiation at a wider spectrum of frequencies. Figure 10-9 show the frequency domain 0-30 MHz and 0-5 MHz, where the recorded interference is stronger.

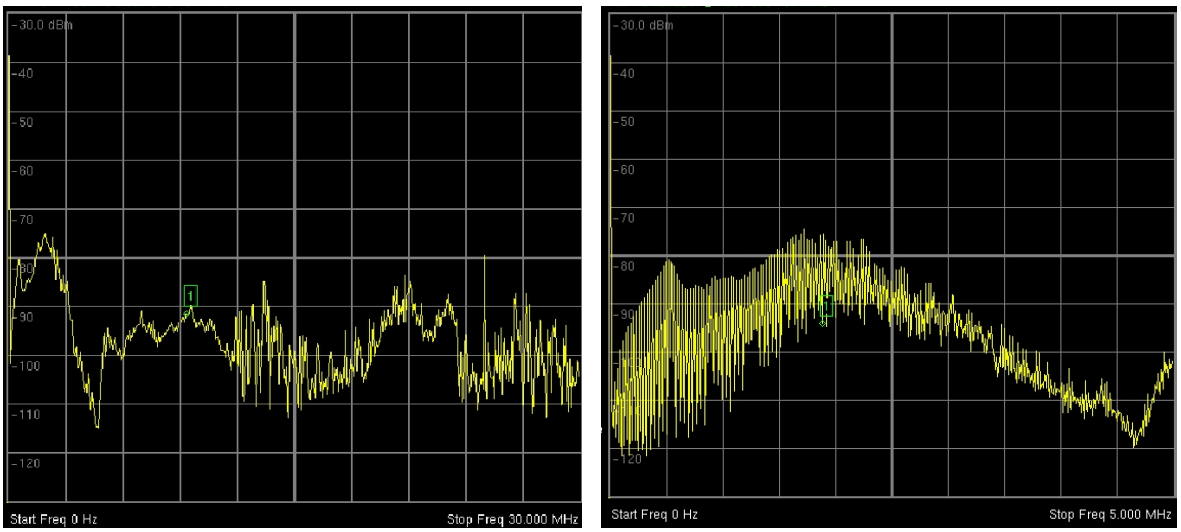

Figure 10-9: Spectrum analysis in frequency domain 0-30 MHz, and 0-5 MHz.

From the data extracted during the tests, it is evident that the major part of the EMI emissions is at 12 kHz. In the range around 2 MHz, the EMI emissions are also significant.

As discussed in chapter 4.3, shielding against low frequency interference is more efficient based on reflection, and not absorption. Reflection shielding is better performed with high permeable material. The effect of shielding interference in the range of 12kHz - 2 MHz waves with a faraday cage is considered to have little effect, so the functionality tests are performed without applying any additional interference other than shielding all high power- and communication cables.

11. Discussion

11.1. Single cell tests

11.1.1. Test A

Cell type A and cell type B are based on the same chemistry and design, using identical anode/cathode and electrolyte materials. The difference in C – rating is largely caused by the cross sectional area of the current collectors within the cell. Cell type A has a continuous current rating of 91.5 A and cell B 56 A. This implies that the current collectors in cell A have a larger cross sectional area than cell type B. Test results from test A-1 reflect this difference through the slightly higher current step response of cell type B. For cells of type A, the equivalent electric resistance during these pulses is approx. 1.9 mΩ for cell type A compared to approx. 2.3 mΩ for cell type B.

The purpose of this test was to evaluate the use of a cell with lower c-rating in a battery system. Using the 144S2P configuration with cell type A implies that the battery cannot support 85kW and still maintain within datasheet specs when cell voltage drops below 3.28 V. This calculation is shown in equation (11.1).

$$U_{\min,pack} = \frac{P_{\max}}{I_{\max}}$$
$$U_{\min,cell} = \frac{P_{\max}}{144 \cdot I_{\max}} \tag{11.1}$$
$$U_{\min,cell} = \frac{85kW}{144 \cdot 180A} = 3.28V$$

Looking at the reference discharge curve presented in Figure 11-1 it is evident that at 3.28 the cell is close to depleted and using 3.3 V as the cut – off voltage should not substantially decrease battery capacity. Test A1 supports the use of cell type B as the voltage drop for pulse discharging at 100 A results in a voltage drop of maximum 233 mV. This means that configuring the AMS to signal fault at 3.3 V could translate to a reference voltage of 3.533 V if subjected to an elevated current pulse at this moment.

From simulation and test results presented in Figure 9-14 and Table 9-10, it can be concluded that the reduction in available range, in terms of time, caused by increasing the cut – off voltage from 3.0 to 3.3 V at load curve A situation translates to a capacity loss of <3.02 %. Since the capacity increase achieved by

using cell type A is 12.9 %, cell B is considered a far better alternative in terms of energy.

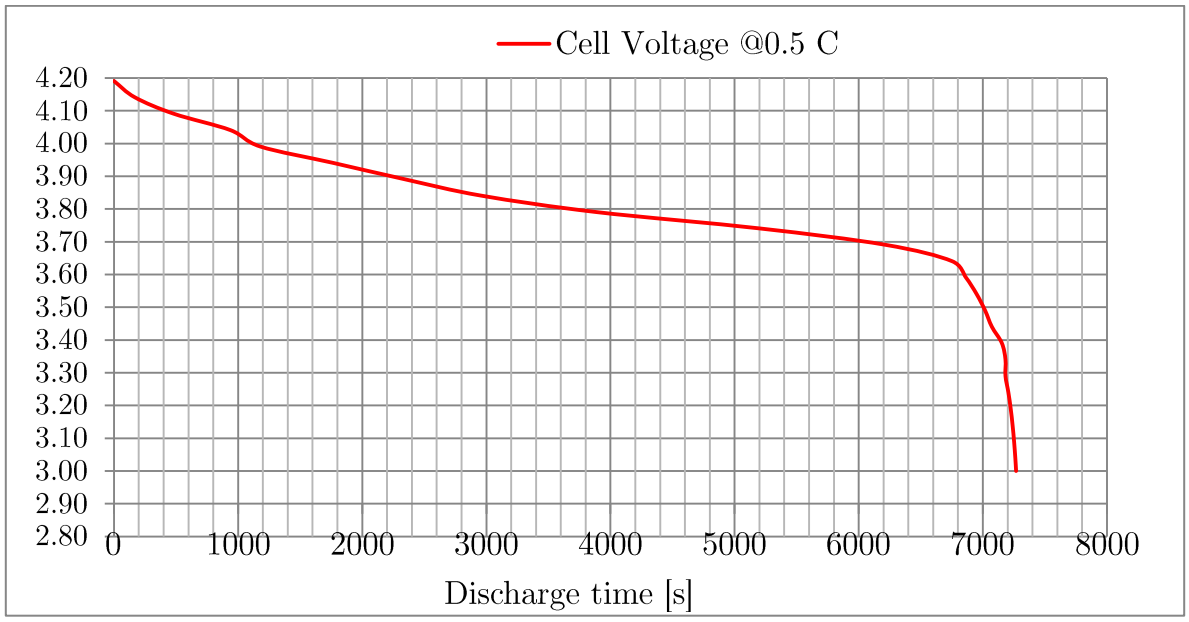

Figure 11-1: Reference discharge curve extracted from tests B1. Discharge condition 0.5 C. Secondary axis is given in [V]

Test A-2 focuses on temperature development in the two cell types. Since type B is rated for lower currents, it was assumed that the losses at elevated currents would be higher than for cell type A. An assumption supported by tests A-1. However, test A2 show that the temperature development per min and energy is higher for cell type A. All tests are performed in identical environment with the same insulation, meaning that the results indicate that cell type B has a higher specific heat capacity than cell type B. The heat dissipation in the battery is based on the equivalent resistance found in voltage drop tests and the current over time. This method is the simplest form of internal impedance testing, and the result could be caused by errors in the test-method. However, cell type B show better temperature performance, which further backs the use of type B cells in the tractive system accumulator

From A-3 it was seen that estimating the temperature development during a variable load discharge can be done based on average current. Additionally, the test revealed that charging the battery at a low SOC is an endothermic reaction, actually reducing the temperature of the battery. Since the tractive system of the racecar uses a kinetic energy recovery system, reversing the PMSM operation to generator mode through reversing the polarity of the magnetic field in the stator, this discovery is very interesting.

11.1.2. Test B

The results visualized in Figure 9-8 show a clear tendency regarding the Peukert's coefficient. For cell B4, the reference discharge was performed as the first discharge in test B2-1, and the reference capacity was not rechecked during the test. The three first discharge tests place the Peukert's coefficient surrounding 1.005196 with an error of 0.5%. The three discharges following the first 8C discharge, using load curve A, 4C and 8C results in a Peukert's coefficient centered at 1.015827 with accuracy of 0.16%. The deviation between the two sets of results can with high probability be caused by the lack of a new reference discharge following the strenuous 8C discharge, which has slightly reduced the battery capacity. The capacity deterioration is small in terms of percentage, but with the capacity fade follows that the reference discharge for the calculations is slightly higher than the real capacity, making the Peukert's coefficient slightly elevated. Unfortunately, capacity check performed in hindsight cannot be considered valid, and there was not sufficient availability of test equipment to repeat the test. The same argumentation can be used to explain the increasing coefficient from tests performed on cell B5. Capacity check was performed at the start of test B2-1, with a 1C discharge. Following this, the cell was discharged at 2C, 3C and 6C before a new capacity check was performed. After this capacity check, the load curve profile was discharged to evaluate the performance. From Figure 9-7 the increase from 2C to 3C is 0.16%, whilst from 3C to 6C the increase is 0.54%. This increase can, as with B4, be explained by a reference capacity check that is "outdated" and slightly higher than the real available capacity.

The data represented by cell B6 is gathered from the life cycle evaluation tests. Following the capacity check of the completely unused cell, four complete discharge cycles are evaluated. From results in appendix G it is clear that the Peukert's coefficient calculated for these four discharges increases. Supported by the theory in chapter 2.11, it can be argued that each discharge slightly alters the available capacity, thereby outdating the reference discharge. To further evaluate the Peukert's coefficient approximation using the average current of the variable discharge, data is gathered from capacity checks at 25 and 50 cycles and the following variable load discharge. This data is represented in Figure 9-10 where the discharge following the 25^{th} cycle has an efficiency of 99.6%, corresponding to a Peukert's coefficient of 1.0021, whilst the discharge following the 50^{th} cycle is evaluated at 98.05% and 1.0101. At the 50^{th} cycle the battery is at 94.6% of its initial capacity. As described in chapter 2.11, the battery performance is affected by the internal aging mechanism like the formation of dendrites around the

electrodes and the possible reduction of free lithium – ions in the electrolyte. When the battery is operated at a later stage in its lifespan, it is therefore natural that the performance at elevated currents is reduced.

Another factor that could cause deviation is the lack of proper temperature control. The tester has been programmed to maintain within allowable values for discharging and charging. However, some discharge cycles start at 28 degrees Celsius whilst others start at 23. The project scope does not cover over the impact of temperature on battery efficiency, but it is nevertheless mentioned as a possible factor of error.

To more accurately determine the Peukert's coefficient for the cell, it was desirable to apply more test cycles. Because of limited time in the test-rig, this was not possible during the master thesis work. Still, the results are centered with a satisfactory error of $<0.5\%$ and give a clear indication of the behavior of the battery cells at elevated current. An average value of 1.012 based on all valid results is used in the Simulink model.

Evaluation of charging time through test B-1 show that dropping saturation charge step reduces total charging time with approx. 10 minutes and reducing capacity by 4.46 %. Lowering maximum cell voltage to 4.1 V show little effect on charge time, but reduces the available capacity by 15.56%.

11.1.3. Test C

Comparing the test results from test C-1 to the datasheet cyclic lifespan for 8C from the manufacturer show that the variable load situation drastically improves battery life. This indicates that estimating cyclic lifespan for LCO-batteries cannot be performed based on the current peaks of the variable load. It also shows a decrease in life expectancy compared to the 1 C situation. Extrapolating the relatively linear behavior from test C-1 and C-2 show that the batteries can be estimated to reach 250-300 cycles at load situation in C-1, and up to 350 cycles for C-2. This indicates that estimating the cyclic life for a variable load is more accurate when using the average current than the peak discharge currents when applying a load profile relevant for an electrical racecar.

Test C-1 and C-2 were based on identical load curves, but in C-2 a 20s resting time was implemented after each 85 s discharge. Due to a program error and the restricted time in the test equipment, only 103 cycles were operated during test C-2. The program fault is explained in appendix K. The two tests are compared in Figure 11-2. The graphs are based on linearization of the capacity checks performed every 25^{th} cycle.

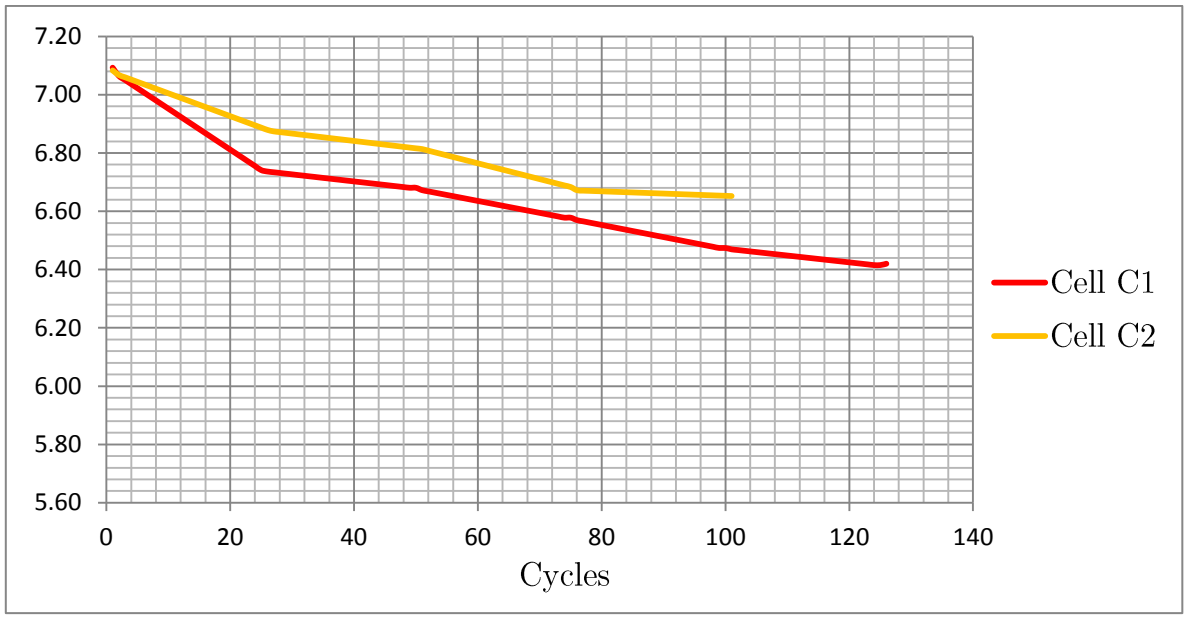

Figure 11-2: Comparison of cycle life test C-1 and C-2, evaluation the effect of implementing a resting time during discharge. Secondary axis represents capacity in [Ah].

The degradation of the batteries up to the 25th cycle shows that battery cell C1 experiences an accelerated capacity fade compared to C2. Through the 50th and 75th cycle, the capacity fade develops in a similar fashion in the two tests. Again, beyond cycle 75, battery C1 experiences a slower degradation. As recited in chapter 2.11.3, other studies have indicated that resting the battery during discharge allows the battery to remain at a stable state closer to electrochemical equilibrium. Studying the temperature plots, Figure 11-3 and Figure 11-4, developed during both test C-1 and C-2, a degree of proportionality in the degradation speed and temperature development can be seen. Up to cycle 25, the C1 is discharged at a temperature up to 10 degrees warmer than C2. This is in the same area were the difference in degradation speed is most noticeable between the two cells. The temperature development is similar during the remainder of the tests.

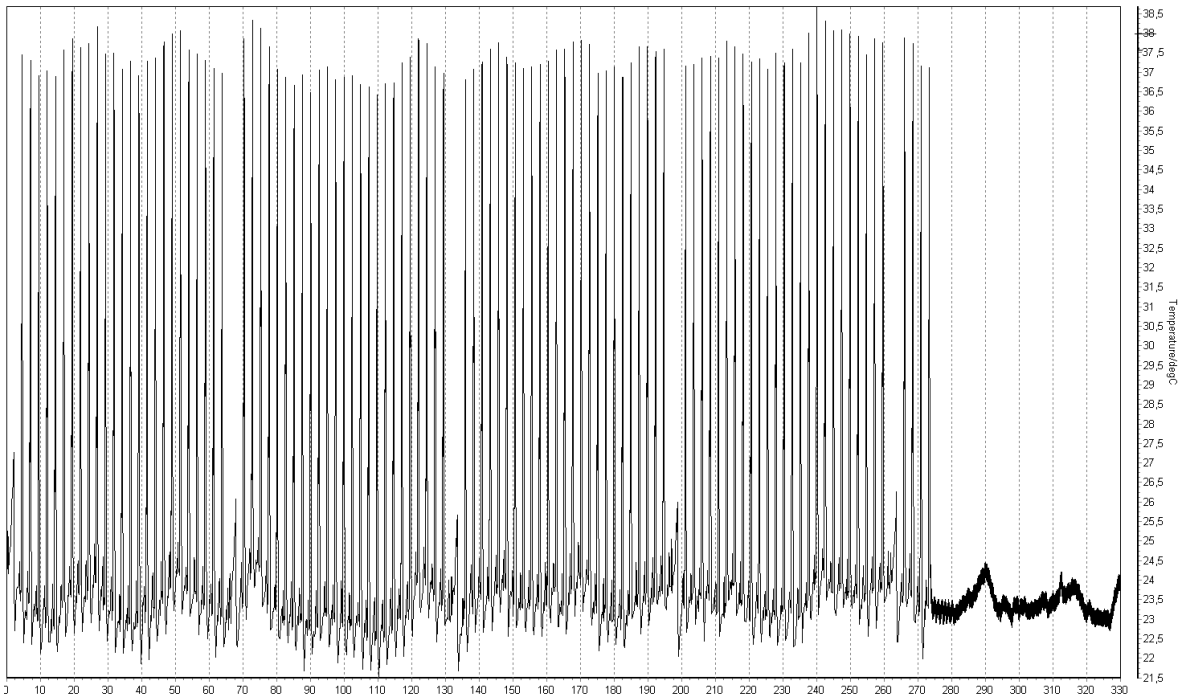

Figure 11-3: Temperature plot during cyclic lifespan test C-2

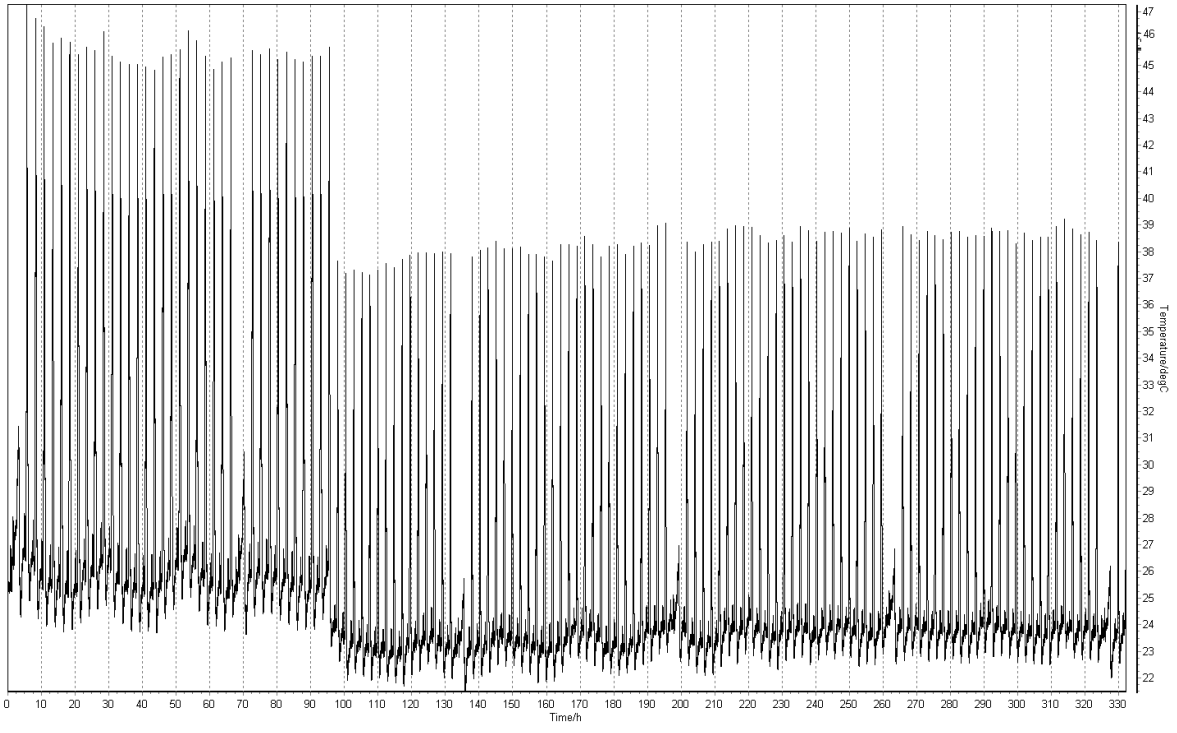

Figure 11-4: Temperature plot during cyclic lifespan test C-1.

This analysis supports that the temperature development during operation is an important parameter when estimating cyclic life. Allowing the battery to rest, and

thus keeping the cell at a more stable electrochemical state could also be a contributor to the capacity development seen in this test, but it seems evident that temperature is the determining parameter when allowing the battery to rest during discharge.

11.2. Coherence of Simulink model and single cell testing

11.2.1. Battery efficiency and charging situations

From the battery efficiency test results, the Simulink model was reconfigured twice. First by altering the battery block configuration and secondly by implementing an addition to the signal path calculating the load current to model the current by the effective current found from Peukert's coefficient. The results from the single cell simulations are compared to the test – results in appendix G. A summary of this comparison can be viewed in table 8-3, where the deviation between battery testing and simulations are presented for each configuration.

Test	Config. 1	Config. 2	Config. 3
S1	n/a	n/a	n/a
S2	n/a	n/a	n/a
S3	-1.072%	0.358%	-1.389%
S4	-1.738%	0.585%	-1.559%
S5	-1.324%	2.041%	-0.483%
S6	-3.722%	1.767%	-1.241%
S7	-3.722%	1.767%	-0.549%
S8	-3.854%	1.391%	-1.174%
S9	n/a	n/a	n/a

Table 11-1: Comparison of the three configurations of the Simulink model from the battery test average result for simulations situation S1-S9

From Table 11-1 it is evident that configuration 3 gives a more evenly accurate result for elevated currents. Using configuration 2, the available capacity is only limited by the state of charge left at cut – off voltage and the energy loss due to dissipation in the battery. As seen in Table 9-6, this reduction is very limited and does not realistically represent the battery behavior at elevated discharge currents. Configuration 1 is flawed through the setup of the Simulink battery block. Available capacity is too high, and the exponential area at the end of the discharge curve is not sufficiently steep, causing the battery to reach cut – off voltage at a SOC that is far too high.

Chapter 9.2.5 presents the simulations where it is attempted to approximate the starting SOC for different charging conditions. It was seen that approximating the starting voltage through altering SOC at start show good accuracy when compared

to tests. As shown in Table 9-11 configuration 3 models the decreased starting voltage with an accuracy of 0.5% compared to the laboratory tests. This is considered satisfactory and as an indication of that the voltage curve of the battery block is configured with good correspondence to the SOC of the real life battery.

11.3. Accumulator design

11.3.1. Capacity and Cell choice

From the market survey and theory in chapter 2, it is concluded that using NMC or LCO cells are more compatible with the requirements for tractive system accumulator for a prototype racecar. With the absolute importance of weight and volume, LCO cells are depicted as the ideal choice.

The cells evaluated in chapter 9.2.3. are all LCO from Melasta Inc. As configuration 144S2P is already decided, the battery system capacity connected to each of the five feasible cells is analyzed with focus on operating time during load curve B discharge. The same simulations indicated that 1 lap on the FSAE Germany racetrack will take 42.5 s. During the competition race the car will have to complete 23 laps, thus needing 977.5 s of driving time at full speed. Based on the data in Table 9-9, Table 11-2 is extracted showing discharge time per weight and volume for the cell alternatives.

	A	B	C	D	E
Time / weight [s/kg]	141.121	138.765	138.065	138.318	141.992
Time / volume [s/l]	61.529	55.839	51.612	56.189	63.107

Table 11-2: Operation time per weight and volume for complete battery system based on cell alternatives.

As seen in Table 9-9, the total simulation time using alternative B is 1052,76 s, which in theory is sufficient for the objective racing situation. From the same table it can be seen that all cells are designed for currents far superior to the estimated average current from the simulated load curve of 50.53 A. Cell type E also present great energy density and specific energy, but would be a severe over dimensioning of the system. Supported by the results and discussion in chapter 11.1, cell type B is the chosen battery cell for the system.

The total system efficiency is not included in this evaluation due to the malfunctioning rotor speed sensor. Accumulator, motor and inverter efficiencies show elevated efficiency from datasheet values and observation during testing, but since no data was obtained, modelling the efficiency in the Simulink model would only include more sources of error. The accumulator energy of 7.45 kWh is

extremely high in the FSAE circuit, and simulation results show that available discharge time is sufficient, and even adds a buffer. This is further attended to in further work.

11.4 Discussion and evaluation of water brake test

Testing the complete system in a laboratory environment provided an opportunity to reveal the system weaknesses prior to installation in the car. In this chapter the important results from the test – period are discussed.

11.4.1 Evaluation of temperature measurement

Additional temperature measurements were applied in order map the system behavior with regards to heat development and to evaluate the accuracy of AMS temperature measurement. Cell tests presented in chapter 9 have already indicated the temperature development in single cells, but as the cells are stacked together in modules and surrounded by firewalls, cooling during operation is very restricted.

At the end of the testing the highest recorded cell temperature was 51 °C. This is only 4 °C short of the AMS limits, indicating that the accumulator should have additional cooling in order reduce the possibility of system shutdown because of high cell temperature. As a result, two fans are installed in the accumulator casing.

The delayed reaction from the battery shown in Figure 10-2 prove that the temperature limits in the AMS should take into account that the developed heat inside the battery propagates to the aluminum film within a couple of minutes. A battery cell rated for 60 °C, should therefore be protected from this delayed temperature increase by the AMS.

11.4.2 Evaluation of voltage and current measurement

Voltage and current measurement result closely match the theory of how lithium cells react to an extensive load. The plot in Figure 11-5 show the system current and the accumulator voltage plotted in the same time period. As current increases, the accumulator responds with a voltage drop. This is both due to the internal resistance of the battery cells and the resistance in electrical connections and transitions in the system.

By examining the voltage drop when the current experiences a sudden step, the electrical resistance of the system can be approximated. Taking the 12s battery response time found in appendix A into account, Table 11-3 is extracted from the test data.

	Step 1	Step 2	Step 3
Voltage response to current step - V	18.21 V	19.57 V	9.38 V
Current step - I	65.72 A	59.67 A	24.73 A
Electrical resistance	277 mΩ	315 mΩ	321mΩ

Table 11-3: Electrical resistance in the system found from the current step response of the accumulator voltage.

The internal impedance of all the battery cells in the system translates to 144 mΩ, meaning the electrical connections represent a total resistance of approximately 160 mΩ. In terms of system efficiency this is considered very satisfactory.

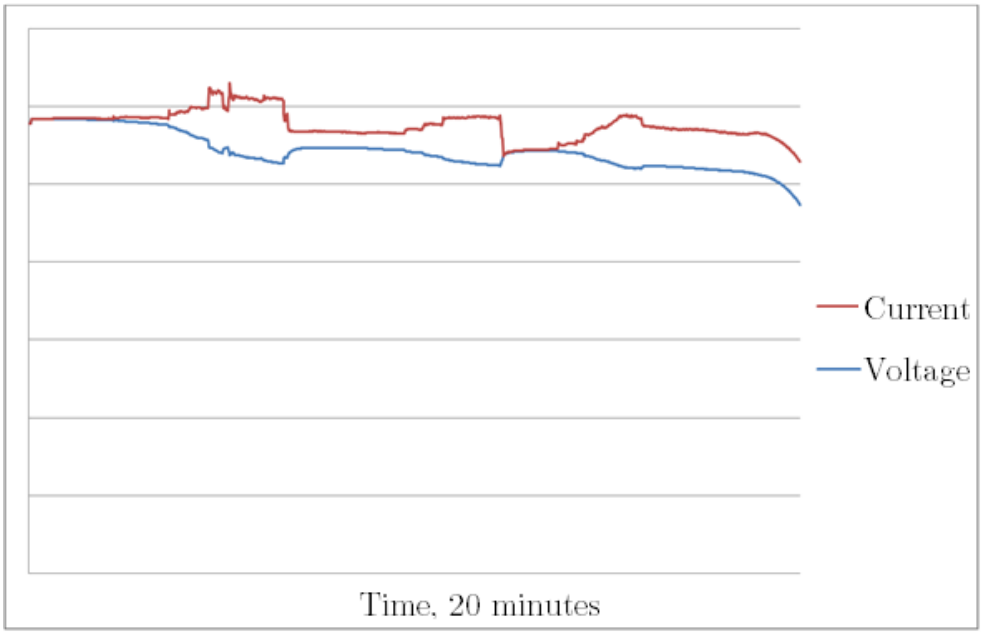

Figure 11-5: Accumulator voltage compared to DC current delivered to the load during tractive system testing

As seen in Figure 10-3, the current suddenly drops to zero in the 13th test minute. This happened because the load pump stopped unexpectedly, resulting in a sudden acceleration of the PMSM before the torque request was disabled. The sudden acceleration that followed is seen in the shaft speed plot found in Figure 10-7. The rotor field surpassed the stator field and the machine was forced into generator operation. This phenomenon explains the negative current measured in the result data.

11.4.3 System efficiency

Logging of shaft speed and torque was done in order to collect data that could be used to evaluate the systems efficiency. This is done by comparing power delivered from the accumulator with the power mechanical power transferred to the shaft, found by analyzing torque and speed.

Analysis of the results revealed errors in the data regarding the shaft speed measurements. At first glance, the results did not seem suspicious as the motor was run at an average rpm between 2500 and 3000. The labview software used to record data from the water brake records data in Hz, and calculating the rotational speed of the rotor based on the frequency data returned had obvious errors. When looking further into this, it became evident that there had been a communicational blunder and that the sensors recording rotational speed data was not properly calibrated and returns data deviating with up to 500 rpm.

We then tried to interpret the results to see if could find an approximation that could give us trustworthy results. But by studying the results shown in Figure 10-7 can it was exposed that the system recorded a speed of 800 rpm during a period where the water brake was at a standstill.

From the manufacturer datasheets the motor efficiency is rated at 90 to 96 % [36]. The inverter is specified with a maximum power loss of 4kW [42]. This translates to 4.7% power loss at 85kW. These large sources of errors combined with the sensor problems have made efficiency data impossible to extract from the tests. As this error was communicated after installing the system in the car, it was not possible to perform the tests using other sensing equipment.

A theoretical approximation of the accumulator system efficiency can be obtained by using the data in Table 11-3 and the load curves. Applying the linearized current from the load curves and the resistance found through the current step response of the system the accumulator losses during endurance race can be calculated.

	Load curve A	Load curve B
Accumulator losses [Wh]	288.33	312.48
Accumulator losses [%]	3.87	4.19

Table 11-4: Theoretical accumulator efficiency based on the electrical resistance found from the current step response and the load curves obtained in chapter 5.2.

The theoretical losses from Table 11-4 are <4.5% and are considered satisfactory.

11.4.4 Evaluation

Even though the efficiency data turned out to be corrupted, the functionality testing was a great success. Both design and assembly flaws were discovered and rectified. The important test conclusions are listed under:

- All 144 cell-connections were monitored with IR-thermometer during extensive load. Poor connections would lead to extensive heating, but none of the connections were recorded with unexpected temperature increase during testing. This test would not have been possible to perform with the accumulator installed in the car.
- Our self-designed quick release module connections were tested with voltage measurements during extensive load without any indication of problems. They were easy to handle and the heat development was not extensive.
- Safety system functionality was tested and approved for car installation.
- Motor controller was tuned and ready for car installation
- The whole tractive system with full functionality was tested and driven from the accelerator.
- Accumulator charging was done several times and team members became familiar with it.

12. Conclusions

During the master thesis work, a complete accumulator system is designed, produced and built. The system has been subjected to extensive testing in laboratory and installed in a prototype racecar. As the most important conclusion of this work, the system works as expected to power a racecar accelerating from 0-100 km/h in only 2.9 s and achieving a top speed of over 120 km/h. An overview of the important operating parameters of the system is summarized in table 12-1.

Total energy	7.46 kWh
Total weight	46.1 kg
Total volume	36.40 l
Nominal voltage	532.8 V
Max. Voltage	604.8 V
Cont. current	112 A
Pulse current (<2 sec.)	180 A
Specific energy	161.8 Wh/kg
Energy density	204.97 Wh/l

Table 12-1: Summary of accumulator system parameters.

The literature and market survey revealed NMC and LFP type cells as the most relevant available lithium – ion batteries for the conventional EV market. For a prototype racecar, the specific energy of the LCO cells surpassed the limitations in lifespan and safety and was thus deemed the best cell chemistry for a racecar application. Further focusing on weight and volume, the cells were dimensioned for the average system current, while supporting estimated current peaks for <2 sec. All tests presented support this decision with regards to performance.

Battery tests show that the Peukert's effect is very small for the 8C LCO – based battery cells compared other battery - technologies. A Peukert's coefficient of 1.012 is defined based on laboratory tests using elevated constant current and variable load discharges. The variable load situation indicate that approximating the Peukert's coefficient based on the average current give decent accuracy compared to constant current discharges. For the Simulink model developed, the Peukert's effect is modelled according to equation *(2.10)* and show an error <1.18% for all simulation conditions compared to laboratory tests. The complete Simulink model with configuration 3 is considered very accurate based on the coherence with battery tests.

Cyclic lifespan tests show that cycling the LCO batteries using a variable load curve with current peaks up to 8C achieve a major increase in lifespan compared to constant current discharges at 8C. The tests also indicate that lifespan estimation

based on average current give a more accurate result than basing estimations on the peak currents. Allowing the battery resting time during affected the cyclic lifespan positively. Data analysis revealed a clear tendency between temperature and capacity fade, indicating that the improvement in lifespan is mostly due to the temperature differences.

13. Further work

As attended to in chapter 0, the reduced availability of the battery testing equipment limited the amount of discharge cycles. The results presented in this master thesis were consistent and gave clear indications regarding the behavior of the cells. However, it would have been preferable to apply more tests cycles for redundancy. This also applies to the life cycle evaluation tests, where time – constraints only permitted cycling the battery down to approximately 91 % of the initial capacity. Even though the degradation of the battery is coherent with theory and progressed linearly until the test was stopped, a thorough test gives a better result than an estimation based on the observed behavior. Also, cycling several batteries for lifespan test would give a more redundant result. Because of the restrictions in current on the tester channels, load curve B could not be evaluated through laboratory testing. The effect of discharging a battery cell with a variable load employing short pulses beyond its continuous rated current – level is a so far unmapped field. Further work on this project should prioritize tests regarding efficiency, Peukert's effect and the effect on the cyclic lifespan with load curve B.

Tests mapping the amount of energy absorbed by the endothermic reaction in the battery during charging at low SOC should be applied. This could be an important parameter when modelling temperature behavior during racing as the car uses regenerative energy.

Theory clearly states that operating a lithium – ion battery at temperatures close to its maximum rating reduces cycle life. However, cycling the batteries in the region between 25 °C vs 35 °C using similar test situations would give clearer results. This will require close temperature control, but is an interesting aspect for optimizing the accumulator system operating conditions in a racecar.

To better estimate the lifespan of the battery when applying a variable load, a lifespan evaluation test using the average current of the load profile should be included in the further work. This will serve as a foundation for comparison and will facilitate lifespan estimation in future racecar applications.

Part of the scope for this thesis work was to evaluate the system and the simulated load curve with the system installed in the car. Due to difficulties with the telemetry in the car, the data from the car is at present not possible to extract. This is a huge point of interest and should be heavily prioritized in the continued work on the project.

Parts of the tractive system laboratory tests were compromised by a malfunctioning speed sensor. As total system efficiency is crucial for correctly

dimensioning of the accumulator system, this has to be attended to in the further work. If fixed and accurate data can be obtained, this should also be implemented in the Simulink model.

Bibliography

[1] D. Linden and T. B. Reddy, Handbook of Batteries, 3 ed., New York: McGraw - Hill, 2001.

[2] N. D. Williard, "Degradation Analysis and Health Monitoring of Lithium Ion Batteries," University of Maryland, College Park, 2011.

[3] G. Albright, J. Edie and S. Al-Hallai, "A Comparison of Lead Acid to Lithium - Ion in Stationary Storage Applications," AllCell Technologies, Chicago, 2012.

[4] K. Young, C. Fierro and M. A. Fetcenko, "Status of Ni/MH Battery Research and Industry," Power and Energy Society General Meeting, IEEE, 2011.

[5] B. E. Jay, "Performance of the Horizon Advanced Lead-Acid Battery.," Wescon/'93 Conference Record, San Fransisco, USA, 1993.

[6] Silicone Batteries, "www.Siliconebatteries.ca," Silicone Batteries, [Online]. Available: http://www.siliconebatteries.ca/siliconebatteries.html. [Accessed 20 February 2014].

[7] Datasheet, "energizer.com," [Online]. Available: http://data.energizer.com/PDFs/nh15-2500.pdf. [Accessed 04 03 2014].

[8] R. Bhandari, Role of Grids fro Electricity and Water Supply with Decreasing Cost for Photovoltaics, 15 ed., Kassel: Kassel university press GmbH, 2010.

[9] National Research Council, Review of the Research Program of the Partnership for a New Generation of Vehciles, 3rd ed., National Academic Press, 1997.

[10] F. Béguin, E. R. Piñero and E. Frackowiak, Carbons for Electrochemical Energy Storage and Conversion Systems, London: CRC Press, 2010.

[11] Maxwell Technologies, "www.maxwell.no," [Online]. Available: http://www.maxwell.com/products/ultracapacitors/docs/k2series_ds_1015370-4.pdf. [Accessed 05 03 2014].

[12] N. Gholamabbas and G. Pistoia, Lithium Batteries: Science and Technology, Austin, Texas: Kluwer Academic Publishers, 2005.

[13] A. Patil, J. -. W. Choi and S. J. Yoon, "Review of Issue and Challenges Facing Rechargeable Nanostructures Lithium Batteries," Nanotechnology Materials and Devices Conference, IEEE,

Gyeongju, 2006.

[14] L. Gaines and R. Cuenca, "Cost of Lithium - Ion Batteries for Vehicle," Argonne National Laboratory Transportation Technology and R & D Center., Chicago, 2000.

[15] Panasonic Corporation, "www.panasonic.com," [Online]. Available: http://www.panasonic.com/industrial/includes/pdf/UPF476790.pdf. [Accessed 2014].

[16] Kokam Co. Ltd., "www.kokam.com," [Online]. Available: http://www.kokam.com/new/kokam/sub01/sub01_01.html. [Accessed 2014].

[17] Valence Technology, "www.valence.com," [Online]. Available: http://www.valence.com/sites/default/files/26650_datasheet_april_2013.pdf. [Accessed 2014].

[18] Gaia Advanced Lithium Battery Systems, "www.gaia-akku.com," [Online]. Available: http://www.gaia-akku.com/fileadmin/user_upload/downloads/cells/7,5AhUHP_NCA.pdf. [Accessed 2014].

[19] A123 Systems, "www.a123systems.com," [Online]. Available: http://www.a123systems.com/prismatic-cell-amp20.htm. [Accessed 2014].

[20] Lighting Global, "Lithium-Ion Battery Overview," International Finance Group, 2012.

[21] J. McDowall, Understanding lithium - ion technology, Saft America Inc., 2008.

[22] J. B. Goodenough, A. K. Padhi, K. S. Nanjundaswamy and C. Masqueller, "Cathode Materials for Secondary Batteries". Patent 5,910,382, 8 June 1999.

[23] Energy Innovation Group, "www.eigbatterygroup.com," [Online]. Available: http://www.eigbattery.com/_eng/designer/skin/02/01_03.asp. [Accessed 20 01 2014].

[24] Hitachi Ltd., "www.hitachi.com," 2014. [Online]. Available: http://www.hitachi.com/rev/pdf/2014/r2014_02_107.pdf. [Accessed 15 03 2014].

[25] D. Doughty and P. E. Roth, "A General Discussion of Li Ion Battery Safety," *The Electrochemical Society Interface,* June 2012.

[26] M. R. Jongerden and B. R. Haverkort, "Battery Modelling," University of Twente, Twente, 2009.

[27] D. Rakhmatov and S. Vrudhula, An Analytical High - Level Battery Model for Use in Energy Management of Portable Electronic Systems, Proceedings of the International Conference on

Computer Aided Design, 2011, pp. 288-493.

[28] D. Doerffel and S. A. Sharkh, A Critical Review of Using the Peukert Equation for Determining the Remaining Cpacity of Lead - Acid and Lithium - Ion Batteries, vol. 155, Journal of Power Sources, 2006, pp. 395-400.

[29] T. Guena and P. Leblanc, "How depth of discharge affects the cycle life of lithium - metal - polymer batteries," Telecommunications Energy Conference. INTELEC '06., 2006.

[30] J. Groot, "State - of - health estimation of li - ion batteries: Cycle life test methods," Chalmers University of Technology, Goteborg, 2012.

[31] S. K. Rahimian, S. C. Rayman and R. E. White, "Maximizing the life of a lithium - ion cell by optimization of charging rates," *Journal of the Electrochemical Society,* Vols. 157. A1302-A1308, 2010.

[32] M. Ecker, J. B. Gerschler, J. Vogel, S. Kabitz, F. Hust, P. Dechent and D. U. Sauer, "Development of a lifetime prediction model for lithium - ion batteries based on extended accelerated aging test data," *Journal of Power Sources,* vol. 215, pp. 248-257, 2012.

[33] H. T. Mahmoud and L. Xu, "A combined Li-Ion & lead - acid battery system for start - stop application: potential & realization," Chalmers University of Technology, Goteborg, 2011.

[34] C. Karnjanapiboon, K. Jirasereeamornkul and V. Monyakul, "High efficiency battery management system for serially connected battery string," King Mongkut's University of Technology Thonburi, Bankok, 2009.

[35] S. Moore and P. Schneider, "A review of cell equalization methods for lithium ion and lithium polymer battery systems," SAE World Congress, Detroit, 2001.

[36] ENSTROJ Sušnik Roman s.p., "www.enstroj.si," [Online]. Available: http://www.enstroj.si/Electric-products/emrax-228-motorsgen.html. [Accessed 05 04 2014].

[37] S. Weber, E. Guttowski, E. Hoene, W. John and H. Reichi, "EMI coupling from automotive traction systems," Franhofer Institure for Reliability and Microgeneration, Munich, 2013.

[38] H. Ott, Noise reduction techniques in instrumentation, 3rd ed., New York: John Wiley & Sons, 1988.

[39] Bender, The power in electrical safety , *A-Isometer IR155-3203 / IR155-3204,* 2010.

[40] J. W. N. a. S. Riedel, *Electric Circuits,* 7 ed., Pearson, 2007.

[41] Eltek Valere, "www.eltek.com," [Online]. Available: http://eltek.com/search/?cat=10003&c=&q=ev+power+charger. [Accessed 20 01 2014].

[42] Unitek Industrie Elektronik, "www.unitek-online.de," [Online]. Available: http://www.unitek-online.de/pdf/download/Antriebe-Drive/BAMOCAR/E-BAMOCAR-D3.pdf. [Accessed 01 06 2014].

Appendix A – Configuration of Simulink battery block

The first set of parameters to be configured for the Simulink block is shown in figure A-1. During the development of the Simulink model, the parameters based on battery type and nominal values were used. For the evaluated cells in this master thesis work, the results were far off from the test – situations. Instead, configuring the block to fit the reference curve at nominal load was attempted.

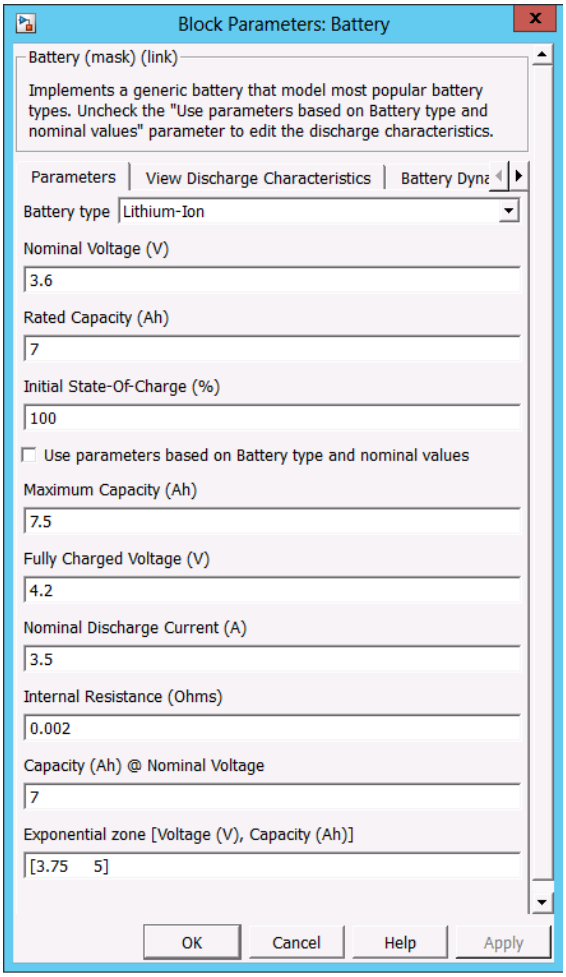

Figure A-1: Configuration of Simulink battery block, overview of the battery parameters.

Configuration of discharge curve

To determine nominal voltages and the exponential zones, tests subjecting the cells to 0.5 C current and 1 C current are conducted. As the LiCoO2 – based cells have a flat voltage platform compared to other chemistries, the configuration of the

battery – block can be complicated. Figure A-2 is an excerpt from the Simulink help section, showing how to calibrate the model after the voltage curve of the battery.

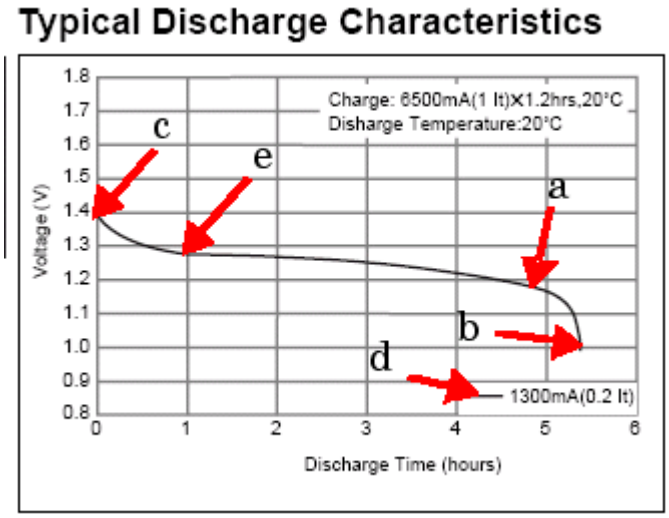

Figure A-2: Except from Simulink library lithium ion block help section regarding adaptation of the load curve of the battery to the specific cell to be used.

In the figure description extracted from the Simulink library help section parameters are explained as follows:

C: Fully charged voltage
E: End of exponential area
A: end of nominal area
B: Cut off voltage

Configuration of the Simulink block according to the battery cells used for testing is performed on the foundation of a reference curve at 0.5 C discharge. This curve is presented in Figure A-3. In the initial configuration, the objective was to achieve a voltage curve from the Simulink battery block that represents the battery cell with an error as small as possible.

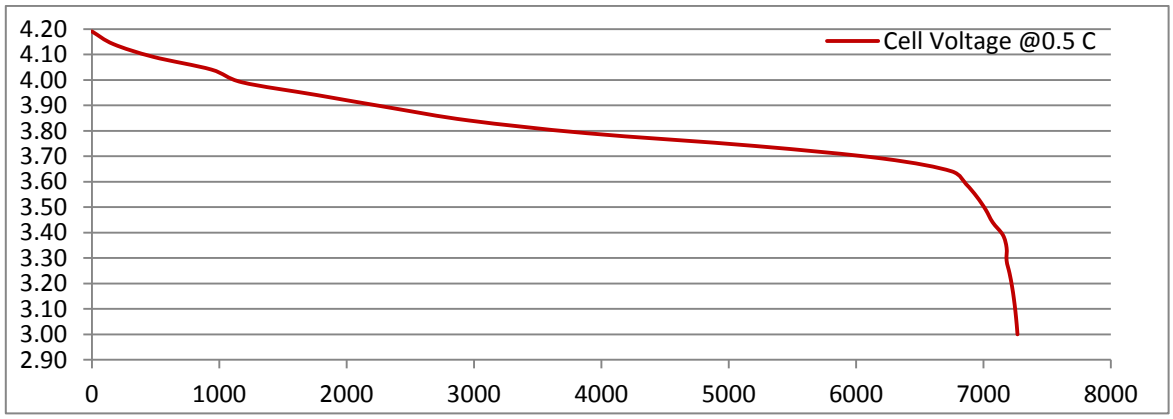

Figure A-3: Reference curve for LCO battery at 0.5 C.

Figure A-4 shows the voltage curve of the battery block when configured for configuration 1.

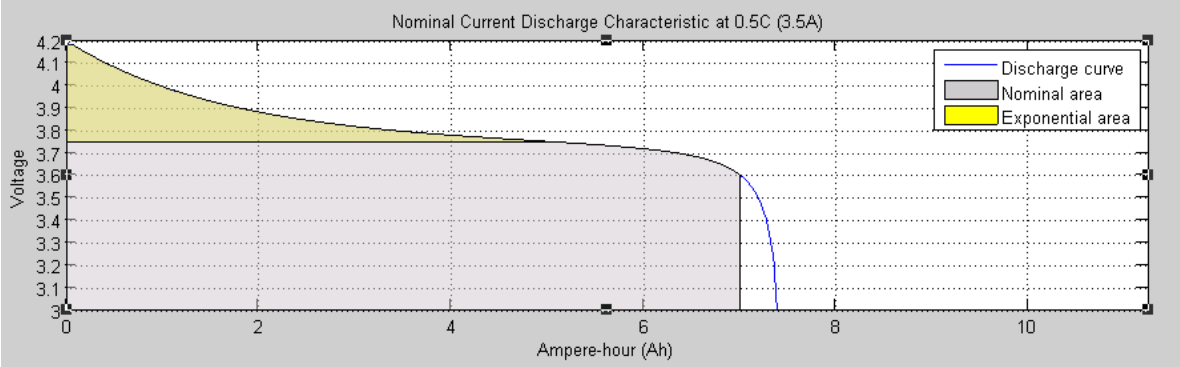

Figure A-4: Configured block reference curve for 0.5 C discharge.

The configuration is achieved by calculating SOC based on total discharge time and applying datasheet values for capacity.

Battery response time

Another important parameter in the Simulink block when using applying variable load to the battery is the response time. The response time represents the voltage dynamics and can be observed when a voltage step is applied to the battery. From Simulink library, a battery response time of 30 s is used to exemplify. This can be seen in figure A-5.

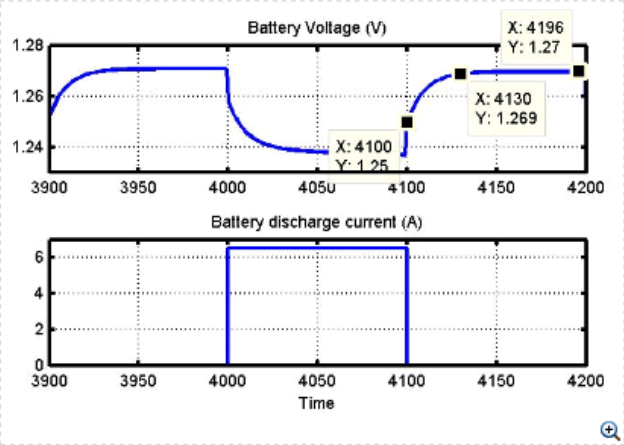

Figure A-5: Battery response time from Simulink help library.

To set the response time of the LiCoO2 battery cell, a current pulse is applied and the data is analyzed. The results can be seen in A-6, using the current pulse from A-7. The same pulse is applied to three different cells of the same type.

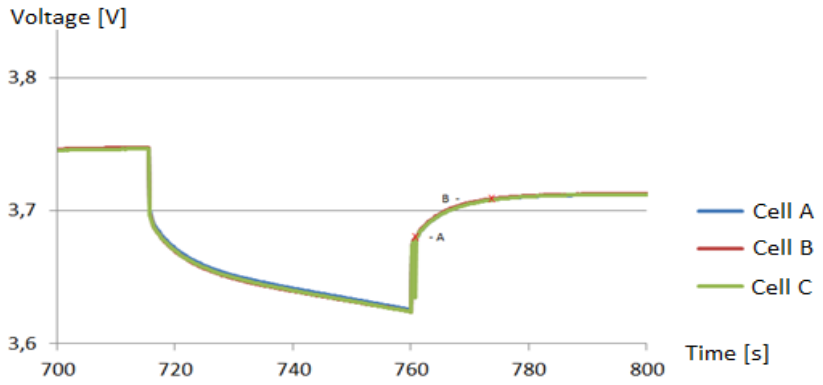

Figure A-6: Response time modelling of LiCoO2 battery cell.

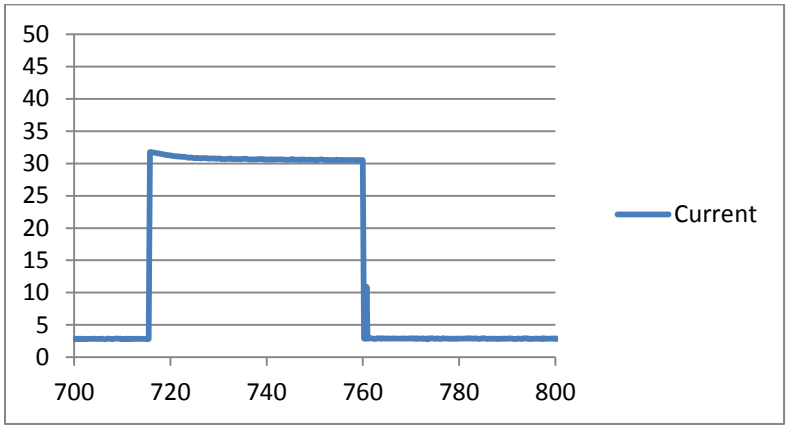

Figure A-7: Discharge pulse to determine battery response time.

Point A: Time = 761s, Voltage = 3.682V

Point B: Time = 773 s, Voltage = 3.720 V

Battery response time = 12 s.

Configuration 1

Configuration 1 is shown in Figure A-1. Battery response time is equal for all configurations. This configuration lead to elevated amounts of energy being stored in the battery when subjected to elevated currents. As it was concluded that the exponential area when the battery is close to depletion was not sufficiently steep.

Configuration 2

To account for the exponential area error in configuration 1, the model block was reconfigured. The maximum capacity of the battery is altered and the exponential zone is changed. In order to find the new values, several attempts were made while studying the reference discharge curve.

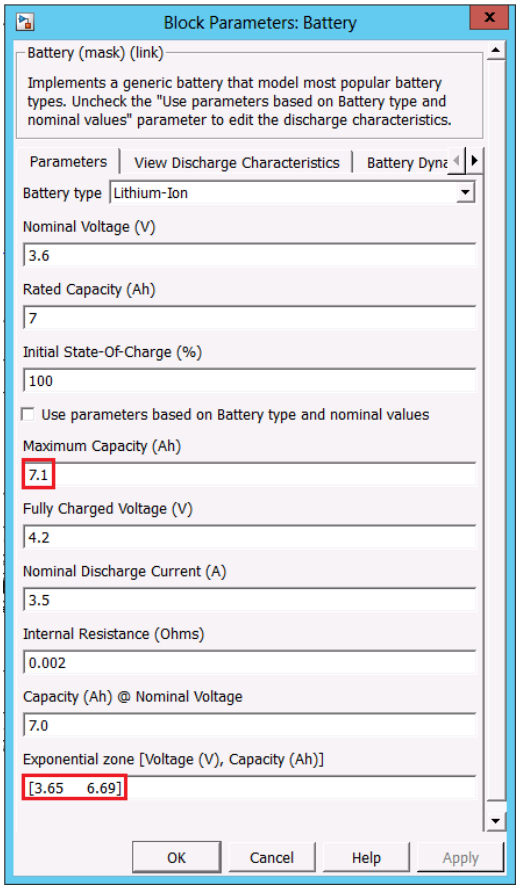

Figure A-8: Simulink battery block configuration 2

The obtained discharge curve for the model is presented in figure A-9.

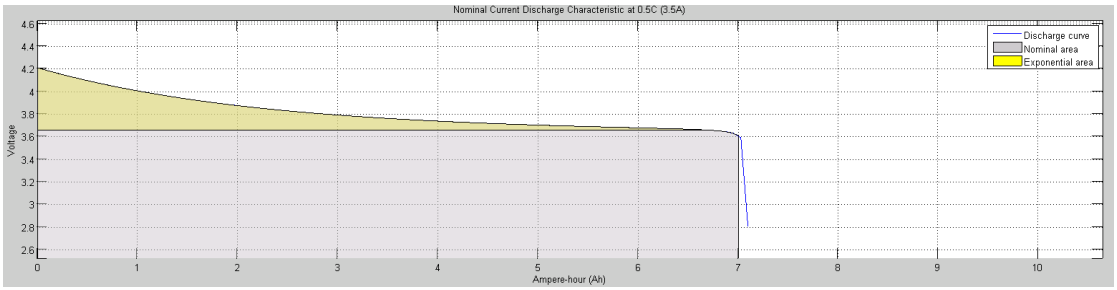

Figure A-9: Simulink battery block discharge curve.

Configuration 3

In model configuration 3, the battery block remains the same as in configuration 2, but the model extension taking Peukert's effect into account is added. This is thoroughly explained in chapter 5.3.

Appendix B – Data processing using Matlab

```
% Open textfile containing testdata and store
fid = fopen('C:\Users\Eiriken\Documents\MATLAB\cyclelife.txt', 'r')
result = zeros(1000000, 3);
count = 0;
i = 1;
%Define needed variables and arrays for capacity check
capacityCheck = zeros(7,3);
capacityCheckCycle = 1;
cycle = 1;
%Define needed variables and arrays for charge cycles
chargeCycle = 1;
chargeCapacity = zeros(200,3);
%Define needed variables and arrays for fastwave discharges
it=1;
tempFastwaveAh = zeros(30,1);
tempFastwaveWh = zeros(30,1);
fastwave = zeros(200,3);
fastwaveCycle = 1;

% Get data from first column
while count == 0
    fgets(fid)
    [A,count] = fscanf(fid, '%i %i %i %id %i:%i:%f %id %i:%i:%f %f %f %f
%f %c')
end
% Get data and store if column is readable
while count ~= 0
    i = i + 1;
    fgets(fid);
    [A,count] = fscanf(fid, '%i %i %i %id %i:%i:%f %id %i:%i:%f %f %f %f
%f %c');

    if(count > 16)
        result(i, 1) = A(12);  %Capacity Ah
        result(i, 2) = A(13);  %Capacity Wh
        result(i, 3) = A(16);  %State R/D/C
    end
    if(mod(i, 100) == 0)
        i
    end
    % Find and store capacity check discharges by identifying the first
    % column in a charge following a discharge with >6 Ah capacity.
    if i>100
     if result(i-1,1) > 6 && result(i,1) <0.001 && result(i-1,3) == 68 &&
result(i,3) == 82
          capacityCheck(capacityCheckCycle, 1) = cycle;
          capacityCheck(capacityCheckCycle, 2) = result(i-1,1);
          capacityCheck(capacityCheckCycle, 3) = result(i-1,2);
          cycle = 25*capacityCheckCycle;
          capacityCheckCycle = capacityCheckCycle +1;
     end
    end
```

```
    % Find and store capacity of each charge by identifying the last
column
    % in a charge state.
    if result(i-1,1) > 6 && result(i,1) <0.001 && result(i-1,3) == 67
        chargeCapacity(chargeCycle,1) = chargeCycle;
        chargeCapacity(chargeCycle,2) = result(i-1,1);
        chargeCapacity(chargeCycle,3) = result(i-1,2);
        chargeCycle = chargeCycle +1;
    end
    % Find and save capacity for each fastwave discharge by identifying
the
    % end of each fastwave - step and adding the results
    if  result(i-1,1) < 0 && result(i,3) == 82 && result(i-1,3) == 68
        tempFastwaveAh(it) = abs(result(i-1,1));
        tempFastwaveWh(it) = abs(result(i-1,2));
        it = it+1;

    end
        % Find end of the complete fastwave discharge - cycle and store
        % values
    if i>100
        if (result(i,3) == 67 && result(i-1,3)~= 67)  && (result(i-10,1)
+ result(i-20) + result(i-30,1) < 0)
          fastwave(fastwaveCycle, 1) = fastwaveCycle;
          AhCapacity = 0;
          WhCapacity = 0;
          for k=1:30
             AhCapacity = AhCapacity + tempFastwaveAh(k);
             WhCapacity = WhCapacity + tempFastwaveWh(k);
          end
          % When the end of a fastwave discharge is identified, vectors
          % used to summarize the capacity are reset and values stored.
           fastwave(fastwaveCycle, 2) = AhCapacity;
           fastwave(fastwaveCycle, 3) = WhCapacity;
           it=1;
           tempFastwaveAh = zeros(30,1);
           tempFastwaveWh = zeros(30,1);
           fastwaveCycle = fastwaveCycle + 1;
     end
    end
end
```

Appendix C – Matlab analyze tool

CalcPower2 – Calculate power and energy based on scope results from Simulink

```
function[totalEnergy] =  calcPower2(batteryVoltage, batteryCurrent,
batterySOC)

display([':::::Analyzing tool for Simulink Li-Ion simulations::::'])
    display([' Nominal rated battery capacity is defined through
discharge at 0.5 C. '])

%Define number of values for current & voltage and identify timestep used
%in Simulink model.
firstStop = 1;
timetocutoff = 0;
dimensions = size(batteryVoltage);
timestep = batteryVoltage(dimensions(1,1), 1)/dimensions(1,1);
initialVoltage = batteryVoltage(1,2);

%Initialize variables used
Energy = 0;
endVoltage = 601;
sumPower = 0;
avgPower = 0;
instaPower = 0;
startSOC = batterySOC(1,2);
i = 0;

while ( i < dimensions(1,1)-1 && firstStop == 1 )
    i = i+1;
    %Calculate total energy extracted from battery
    instaPower =
(batteryVoltage(i,2)+batteryVoltage(i+1,2))/2*(batteryCurrent(i,2)+batter
yCurrent(i+1,2))/2;
    timestepEnergy = instaPower * timestep;
    %tempEnergy = totalEnergy + timestepEnergy;
    Energy = Energy + timestepEnergy;
    %Calculate average power
    sumPower = sumPower + instaPower;
    if i<(dimensions(1,1)-1000)
      if (batteryCurrent(i,2) == 0 && batteryCurrent (i+999,2) == 0 &&
firstStop == 1)
          timetocutoff = batteryCurrent(i,1);
          %endVoltage = batteryVoltage(i,2);
         firstStop = 0;
      end
    end
    %Search for cut off voltage
    voltage = batteryVoltage(i,2);
    if voltage < endVoltage
        endVoltage = voltage;
    end
```

```
end
%Define average power and total energy in Wh
avgPower = sumPower/i;
totalEnergy = Energy / 3600 ;
endSOC = batterySOC(i,2);

display(['Total energy extracted from battery during simulation: '])
display(['        ', num2str(totalEnergy), 'Wh'])
display(['Average power during simulation is: '])
display(['        ', num2str(avgPower/1000), 'kW'])
display(['The simulation time until cut - off voltage is reached is '])
display(['        ', num2str(timetocutoff), ' seconds'])
%display(['At cut of voltage, the battery state of charge is : '])
%display(['         ', num2str(endSOC), '%'])
display(['DOD for this simulation is : '])
display(['        ', num2str(startSOC), ' / ', num2str(endSOC)])
%Start and end voltage
display(['At the given SOC at start, the voltage is : '])
display(['        ', num2str(initialVoltage), ' V ,', ' ',
num2str(endVoltage),' V '])

calcEfficiency(totalEnergy, startSOC);
```

CalcEfficiency – Calculate energy efficiency based on simulation results and user input

```
function [efficiency] = calcEfficiency(Energy, startSOC)
nomEnergy = input('Insert nominal capacity of battery in Wh:  ');
nomEnergySOC = nomEnergy *startSOC/100;
efficiency = 100*Energy / nomEnergySOC;

display(['The efficiency of the battery with applied load is: '])
display(['        ', num2str(efficiency), '%'])

display(['The extracted energy compared to 100/0 DOD at 0.5 C'])
display(['        ', num2str(100*Energy/nomEnergy),' %      '])

end
```

Appendix D– Complete results Test A

Pulses 6.1 Ah Cell								
	Time	Voltage			Current	Voltage Dip		
	13.536	3.690	3.689	3.686	2.991	0.041	0.093	0.098
Pulse 1	13.907	3.649	3.596	3.588	2.980	0.069	0.014	0.012
	14.364	3.580	3.582	3.576	82.117	0.007	0.006	0.006
	14.733	3.574	3.576	3.570	81.918	0.005	0.005	0.005
	15.101	3.568	3.571	3.565	81.786	0.005	0.005	0.005
	15.472	3.564	3.566	3.560	81.710	-0.099	-0.097	-0.101
	15.841	3.663	3.663	3.661	81.484			
				Total Voltage Drop		0.127	0.123	0.126
	Time	Voltage			Current	Voltage Dip		
Pulse 2	5.106	3.983	3.978	3.990		0.000	0.040	0.136
	5.476	3.983	3.938	3.854	2.876	0.153	0.109	0.024
	5.933	3.830	3.829	3.831	87.239	0.012	0.011	0.012
	6.302	3.818	3.817	3.819	86.941	0.009	0.008	0.009
	6.673	3.808	3.809	3.810	86.742	0.008	0.007	0.007
	7.043	3.801	3.802	3.803	86.556	-0.130	-0.129	-0.138
	7.411	3.931	3.931	3.941	86.366	-0.012	-0.010	-0.010
	7.868	3.943	3.941	3.950	2.927			
				Total Voltage Drop		0.182	0.176	0.188
	Time	Voltage			Current	Voltage Dip		
Pulse 3	58.245	3.970	3.967	3.974	2.843	0.196	0.193	0.204
	59.071	3.774	3.774	3.771	107.905	0.015	0.013	0.013
	59.439	3.759	3.761	3.757	107.501	0.011	0.010	0.011
	59.808	3.748	3.750	3.747	107.212	0.009	0.009	0.009
	0.177	3.739	3.741	3.738	106.987	-0.173	-0.171	-0.182
	0.546	3.912	3.913	3.920	67.075	-0.013	-0.011	-0.010
	1.004	3.924	3.923	3.930	2.871			
				Total Voltage Drop		0.231	0.226	0.237
	Time	Voltage			Current	Voltage Dip		
Pulse 4	4.131	3.699	3.698	3.695	3.008	0.097	0.096	0.101
	4.500	3.602	3.601	3.594	3.012	0.014	0.012	0.011
	4.957	3.588	3.590	3.583	82.274	0.006	0.006	0.006

	5.326	3.581	3.583	3.577	82.121	0.006	0.005	0.005
	5.694	3.576	3.578	3.572	81.992	0.005	0.005	0.005
	6.066	3.571	3.573	3.567	81.877	-0.102	-0.099	-0.103
	6.523	3.673	3.673	3.670	2.956			
				Total Voltage Drop		0.128	0.124	0.128
	Time	Voltage			Current	Voltage Dip		
Pulse 5	25.956	3.975	3.971	3.980	2.843	0.000	0.106	0.136
	26.325	3.975	3.864	3.844	2.852	0.193	0.083	0.065
	26.782	3.782	3.781	3.779	108.137	0.016	0.014	0.015
	27.152	3.766	3.767	3.765	107.677	0.012	0.011	0.011
	27.521	3.754	3.756	3.754	107.358	0.009	0.009	0.009
	27.891	3.745	3.747	3.744	107.141	-0.168	-0.167	-0.178
	28.259	3.913	3.914	3.922	106.873	-0.015	-0.013	-0.012
	28.717	3.928	3.927	3.934	2.836			
				Total Voltage Drop		0.230	0.223	0.236
	Time	Voltage			Current	Voltage Dip		
Pulse 6	58.688	3.416	3.381	3.375	2.420	0.094	0.097	0.103
	59.188	3.322	3.284	3.273	2.419	0.028	0.031	0.030
	59.776	3.294	3.253	3.242	75.161	0.018	0.021	0.021
	0.019	3.276	3.232	3.222	74.742	-0.068	-0.069	-0.075
	0.688	3.344	3.301	3.297	74.167	-0.009	-0.007	-0.005
	1.276	3.352	3.308	3.302	2.443			
				Total Voltage Drop		0.141	0.149	0.154

Table D-1: Test results test A1 using cell type A

Pulses 7 Ah Cell								
	Time	Voltage			Current	Voltage Dip		
Pulse 1	53.532	4.064	4.068	4.077	0.560	0.000	0.062	0.124
	53.947	4.064	4.006	3.952	64.330	0.186	0.157	0.077
	54.450	3.877	3.849	3.875	89.310	0.017	0.018	0.015
	54.865	3.860	3.831	3.861	88.620	0.013	0.013	0.012
	55.281	3.848	3.818	3.849	88.620	0.010	0.011	-0.156
	55.695	3.838	3.807	4.005				

				Total Voltage Drop		0.226	0.261	0.228
	Time	Voltage			Current	Voltage Dip		
Pulse 2	45.718	3.954	3.953	3.958	2.757	0.079	0.119	0.164
	46.133	3.875	3.834	3.794	85.884	0.097	0.082	0.023
	46.636	3.778	3.752	3.771	85.501	0.013	0.013	0.012
	47.051	3.766	3.739	3.760	85.249	0.009	0.010	0.009
	47.465	3.756	3.729	3.751	84.994	0.008	-0.164	-0.156
	47.881	3.748	3.893	3.906	2.802			
				Total Voltage Drop		0.206	0.224	0.207
	Time	Voltage			Current	Voltage Dip		
Pulse 3	44.956	3.956	3.955	3.959	2.481	0.000	0.117	0.110
	45.372	3.956	3.838	3.849	85.992	0.174	0.083	0.074
	45.874	3.782	3.755	3.775	85.650	0.013	0.014	0.012
	46.289	3.769	3.741	3.763	85.405	0.010	0.010	0.009
	46.705	3.759	3.731	3.754	85.098	0.008	-0.033	-0.153
	47.119	3.751	3.764	3.907	2.814			
				Total Voltage Drop		0.204	0.224	0.206
	Time	Voltage			Current	Voltage Dip		
Pulse 4	24.435	3.855	3.854	3.858	2.839	0.000	0.000	0.000
	24.850	3.855	3.854	3.858	84.293	0.156	0.172	0.166
	25.352	3.699	3.682	3.693	83.976	0.012	0.012	0.011
	25.767	3.687	3.670	3.682	83.717	0.009	0.009	0.008
	26.181	3.678	3.661	3.674	83.488	0.007	0.007	0.007
	26.596	3.671	3.654	3.667	50.648	-0.145	-0.160	-0.155
	27.011	3.816	3.814	3.822	low			
				Total Voltage Drop		0.184	0.200	0.191

	Time	Voltage			Current	Voltage Dip		
Pulse 5	38.715	3.844	3.843	3.847	2.780	0.000	0.151	0.148
	39.130	3.844	3.692	3.698	83.968	0.160	0.024	0.020
	39.633	3.685	3.668	3.679	83.638	0.010	0.011	0.009
	40.048	3.674	3.658	3.669	83.435	0.008	0.008	0.007
	40.462	3.667	3.650	3.662	83.195	0.006	-0.121	-0.140
	40.878	3.661	3.771	3.802	2.802			
				Total Voltage Drop		0.184	0.193	0.185
	Time	Voltage			Current	Voltage Dip		
Pulse 6	46.302	3.641	3.651	3.645	2.948	0.000	0.000	0.122
	46.717	3.641	3.651	3.523	80.453	0.137	0.142	0.022
	47.220	3.504	3.509	3.502	80.228	0.012	0.011	0.011
	47.635	3.492	3.498	3.491	79.976	0.011	0.010	0.010
	48.050	3.481	3.488	3.480	79.753	0.010	0.009	-0.113
	48.464	3.471	3.478	3.593	2.996			
				Total Voltage Drop		0.170	0.172	0.165
	Time	Voltage			Current	Voltage Dip		
Pulse 7	5.211	3.734	3.735	3.734	2.874	0.129	0.125	0.175
	5.629	3.605	3.610	3.559	101.857	0.062	0.070	0.020
	6.131	3.543	3.539	3.539	101.508	-0.169	-0.174	-0.175
	6.546	3.711	3.713	3.714	2.969	3.711	3.713	3.714
						0	0	0
				Total Voltage Drop		0.191	0.196	0.195
	Time	Voltage			Current	Voltage Dip		
Pulse 8	13.819	3.808	3.807	3.810	2.870	0.147	0.142	0.194
	14.23	3.66	3.66	3.616	103.05	0.062	0.078	0.020

	4	1	5		5			
	14.737	3.599	3.587	3.595	102.776	0.011	0.011	0.010
	15.152	3.587	3.576	3.585	102.471	0.008	0.008	0.008
	15.567	3.579	3.568	3.577	102.347	-0.180	-0.191	-0.189
	15.981	3.759	3.759	3.766	2.909			
				Total Voltage Drop		0.229	0.239	0.233
				Total Voltage Drop		0.074	0.089	0.031
	Time	Voltage			Current	Voltage Dip		
Pulse 9	31.181	3.828	3.827	3.831	2.944	0.149	0.159	0.156
	31.596	3.680	3.668	3.675	83.302	0.018	0.017	0.015
	32.098	3.662	3.650	3.660	83.086	0.009	0.009	0.008
	32.513	3.653	3.641	3.652	82.932	0.007	0.007	0.007
	32.928	3.646	3.634	3.645	82.745	-0.141	-0.152	-0.149
	33.343	3.787	3.786	3.794	2.929			
				Total Voltage Drop		0.182	0.193	0.186

Table D-2: Test results from A1 using cell type B

Appendix E – Results from single cell test A2

				Avg. Temp Increase [K/min x J]
Cell type B	Test A2 – 1 Cell B1, B2, B3	Avg. Current [A]	31,04305	0,0013655
		Heat Dissipation (Based on Avg. Current) [J]	1410,815	
		Heat Dissipation (Based on Real - Time Data) [J]	1699,673	
		Avg. Temperature per minute [K]	1,928852	
		Time [s]	732	
		Total temperature Increase [K]	20,224	
		Temperature Increase [K / Min x J]	0,001367	
	Test A2 – 2 Cell B1, B2, B3	Avg. Current [A]	30,6805	
		Heat Dissipation (Based on Avg. Current) [J]	1351,697	
		Heat Dissipation (Based on Real - Time Data) [J]	1210,507	
		Avg. Temperature per minute [K]	1,862201	
		Time [s]	718	
		Total temperature Increase [K]	22,28433	
		Temperature Increase [K / Min x J]	0,001378	
	Test A2 – 3 Cell B1, B2, B3	Avg. Current [A]	30,60955	
		Heat Dissipation (Based on Avg. Current) [J]	1354,822	
		Heat Dissipation (Based on Real - Time Data) [J]	1198,294	
		Avg. Temperature per minute [K]	1,831231	
		Time [s]	723	
		Total temperature Increase [K]	22,06633	
		Temperature Increase [K / Min x J]	0,001352	
Cell A	Test A2 – 4 Cell A1, A2, A3	Avg. Current [A]	30,6495	0,0017336
		Heat Dissipation (Based on Avg. Current) [J]	1193,028	
		Heat Dissipation (Based on Real - Time Data) [J]	1177,686	
		Avg. Temperature per minute [K]	1,89578	
		Time [s]	635	
		Total temperature Increase [K]	20,06367	
		Temperature Increase [K / Min x J]	0,001589	

	Test A2 – 5 Cell A1, A2, A3	Avg. Current [A]	30,35641
		Heat Dissipation (Based on Avg. Current) [J]	1153,733
		Heat Dissipation (Based on Real - Time Data) [J]	1162,935
		Avg. Temperature per minute [K]	1,825463
		Time [s]	626
		Total temperature Increase [K]	19,04567
		Temperature Increase [K / Min x J]	0,001582
	Test A2 – 6 Cell A1, A2, A3	Avg. Current [A]	27,20881
		Heat Dissipation (Based on Avg. Current) [J]	949,0893
		Heat Dissipation (Based on Real - Time Data) [J]	940,2632
		Avg. Temperature per minute [K]	1,903495
		Time [s]	641
		Total temperature Increase [K]	20,33567
		Temperature Increase [K / Min x J]	0,002006
	Test A2 - Cell A1, A2, A3	Avg. Current [A]	30,25958
		Heat Dissipation (Based on Avg. Current) [J]	1124,408
		Heat Dissipation (Based on Real - Time Data) [J]	1072,912
		Avg. Temperature per minute [K]	1,976287
		Time [s]	614
		Total temperature Increase [K]	20,224
		Temperature Increase [K / Min x J]	0,001758

Table E-1 Test results from test A-2 using cell types A and B.

Appendix F – Simulation and test results regarding cut – off voltage

	Load situation	Load curve A	Load curve A	Load curve A
	Cell	-	-	-
	Start voltage [V]	4.2	4.2	4.2
	Capacity [Ah]	7	7	7
	Cut off voltage [V]	3	3.2	3.3
	SOC start	100.00%	100.00%	100.00%
1	SOC cut off	5.05%	7.49%	13.31%
	Discharge. Time [s]	1053.15	1020	969
3	SOC cut off	0.58%	0.79%	0.92%
	Discharge. Time [s]	1054.5	1053.67	1053.08
B4	SOC cut off	0.057%	1.359%	2.506%
	Discharge. Time [s]	1044.52	1036.52	1024.52
B5	SOC cut off	2.400%	3.868%	4.898%
	Discharge. Time [s]	1011.4	1005.4	999.4
B6	SOC cut off	0.874%	2.820%	2.890%
	Discharge. Time [s]	1028.4	1019.4	997.4

Table F-1: Test – and simulation – results regarding effect of cut – off voltage

Appendix G – Simulation and tests results to configure lithium ion battery block

Test	Configuration 1		Configuration 2		Configuration 3		Test results			Cell
	Cap. [Ah]	Eff. [%]	Cap. [Ah]	Eff. [%]	Cap. [Ah]	Eff. [%]	Cap. [Ah]	Eff. [%]	Avg. Eff. [%]	
S1	7.391	100%	7.091	100%	7.091	100%	7.064	100%	100%	B4
							7.083	100%		B5
							7.093	100%		B6
							6.741	100%		B6
							6.681	100%		B6
S2	7.354	99.51%	7.088	99.96%	7.029	99.13%	7.111	100%	100%	B5
S3	7.282	98.53%	7.081	99.96%	6.964	98.22%	7.083	99.60%	99.60%	B5
S4	7.203	97.47%	7.075	99.77%	6.924	97.64%	7.054	99.19%	99.19%	B5
S5	7.123	96.39%	7.068	99.67%	6.893	97.21%	6.988	98.27%	97.68%	B4
							6.858	97.09%		B4
S6	6.954	94.10%	7.053	99.46%	6.844	96.52%	6.950	97.73%	97.73%	B5
S7	6.771	91.62%	7.036	99.23%	6.804	95.95%	6.870	97.25%	96.48%	B4
							6.761	95.71%		B4
S8	6.989	94.57%	7.072	99.73%	6.893	97.21%	6.914	97.61%	98.36%	B5
							6.881	97.14%		B5
							7.060	99.94%		B4
							6.827	96.64%		B4
							7.032	99.14%		B6
							7.034	99.17%		B6
							6.994	98.61%		B6
							6.932	97.73%		B6
							6.714	99.60%		B6
							6.550	98.05%		B6
S9	7.121	96.35%	7.063	99.61%	6.887	97.13%	n/a	n/a	n/a	n/a

Table G-1: Comparison of test – results and simulation results regarding battery efficiency.

Appendix H – Excerpt from datasheet cell type B, Melasta Inc.

1. 序言 PREFACE

此规格书适用于深圳鸿星电池有限公司的锂聚合物可充电电池产品

The specification is suitable for the performance of Lithium-Polymer (LIP) rechargeable battery produced by the SHENZHEN MELASTA BATTERY CO., LTD.

2. 型号 MODEL

LPA045135 7000mAh 8C 3.7V

3. 产品规格 SPECIFICATION

单颗电池规格 Specifications of single cell

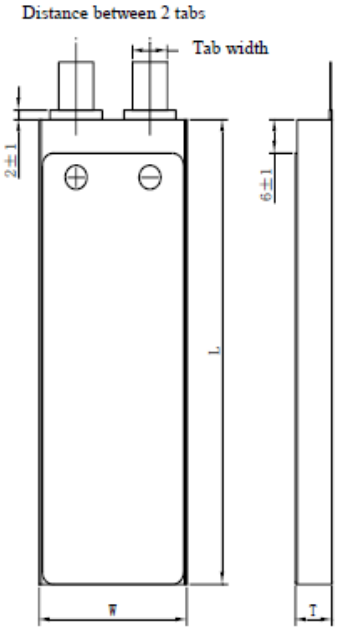

◆标称容量 Typical Capacity①		7.0Ah
◆标称电压 Nominal Voltage		3.7V
◆充电条件 Charge Condition	最大电流 Max. Continuous charge Current	14.0A
	峰值充电 Peak Charge current	28A(≤1 sec)
	电压 Voltage	4.2V±0.03V
◆ 放电条件 Discharge Condition	Max Continuous discharge Current	56A
	Peak Discharge Current	90A(≤2 secs)
	Cut-off Voltage	3.0V
◆交流内阻 AC Impedance(mOHM)		<2.0
◆循环寿命【充电:1.0C,放电:8C】 Cycle Life【CHA:1.0C,DCH:8C】		>100cycles
◆使用温度 Operating Temp.	充电 Charge	0℃~45℃
	放电 Discharge	-20℃~60℃
◆ 电芯尺寸 Cell Dimensions	厚度 Thickness(T)	9.7±0.3mm
	宽度 Width(W)	45±0.5mm
	长度 Length(L)	136.5±0.5mm
	极耳间距 Distance between 2 tabs	23±1mm
◆ 极耳尺寸 Dimensions of Cell tabs	极耳宽度 Tab Width	12mm
	极耳厚度 Tab Thickness	0.2mm
	极耳长度 Tab Length	30mm
◆重量 Weight(g)		135.0±2.0
①标称容量：0.5CmA,4.2V~3.0V@23℃±2℃ Typical Capacity:0.5CmA,4.2V~3.0V@23℃±2℃		

Appendix I – Datasheet INR18650-29E Samsung SDI

Spec. No.	INR18650-29E	Version No.	1.1

1. Scope

This product specification has been prepared to specify the rechargeable lithium-ion cell ('cell') to be supplied to the customer by Samsung SDI Co., Ltd.

2. Description and Model

2.1 Description Cell (lithium-ion rechargeable cell)

2.2 Model INR18650-29E

3. Nominal Specifications

Item	Specification
3.1. Nominal Capacity	2,850mAh (0.2C, 2.50V discharge)
3.1.1. Typical Capacity	2,850mAh (0.2C, 2.50V discharge)
3.1.2. Minimum Capacity	2,750mAh (0.2C, 2.50V discharge)
3.2. Charging Voltage	4.20 ± 0.05 V
3.3. Nominal Voltage	3.65V (0.2C discharge)
3.4. Charging Method	CC-CV (constant voltage with limited current)
3.5. Charging Current	Standard charge: 1,375mA
3.6. Charging Time	Standard charge: 3hours
3.7. Max. Charge Current	2750mA (not for cyclelife)
3.8. Max. Discharge Current	2,750mAh (continuous discharge) 8250mAh (not for continuous discharge)
3.9. Discharge Cut-off Voltage	2.50V
3.10. Cell Weight (max. (g))	48g
3.11. Cell Dimension	Diameter(max.) : 18.40 mm Height(max) : 65.00 mm
3.12. Operating Temperature (Cell Surface Temperature)	Charge: 0 to 45°C Discharge: -20 to 60°C
3.13. Storage Temperature	1 year : -20~25°C (1*) 3 months : -20~45°C (1*) 1 month : -20~60°C (1*)

Note (1): If the cell is kept as ex-factory status (50% of charge),
The capacity recovery rate is more than 80%.

Appendix J – Test results test B-2

Test	Discharge current [C]	Discharge Voltage [V]	Discharge capacity [Ah]	Discharge capacity [Wh]	Efficiency [Ah]	Efficiency	Peukert's coefficient	Cell
B1-1	0.5	3.0	7.064	27.011	-		-	B4
B2-1	4	3.0	6.988	26.033	98.93%	98.93%	1.0052	B4
B2-1	4	3.0	6.858	25.499	97.09%	97.09%	1.0142	B4
B2-1	8	3.0	6.870	24.970	97.25%	97.25%	1.0101	B4
B2-1	8	3.0	6.761	24.515	95.71%	95.71%	1.0158	B4
B2-1	Load curve	3.0	7.060	26.298	99.94%	99.94%	1.0003	B4
B2-1	Load curve	3.0	6.827	25.377	96.64%	96.64%	1.0175	B4
Constant current discharges								
B2-2	1	3.0	7.111	26.782	-		-	B5
B2-2	2	3.0	7.0827	26.75284	99.60%	99.60%	1.0058	B5
B2-2	3	3.0	7.05366	26.41195	99.59%	99.59%	1.0074	B5
B2-2	6	3.0	6.95005	25.50297	98.53%	98.53%	1.0128	B5
Start of cycle life test 2								
B2-4	0.5	3.0	7.083	27.080	-		-	B5
B2-4	Load curve	3.0	6.914	25.696	97.61%	97.61%	1.0124	B5
B2-4	Load curve	3.0	6.8809	25.555	96.76%	96.76%	1.0148	B5
Start of cycle life test 1								
B2-3	0.5 C	3.0	7.093	27.144	-		-	B6
B2-3	Load curve	3.0	7.032	2.163	99.14%	99.14%	1.0043	B6
B2-3	Load curve	3.0	7.034	26.148	99.17%	99.17%	1.0043	B6
B2-3	Load curve	3.0	6.994	25.99	98.61%	98.61%	1.0072	B6
B2-3	Load curve	3.0	6.932	25.838	97.73%	97.73%	1.0117	B6
New reference cycle life test 1, cycle 25								
B2-3	0.5 C	3.0	6.741	25.725	-		-	B6
B2-3	Load curve	3.0	6.714	24.834	99.60%	99.60%	1.0021	B6
New reference cycle life test 1, cycle 50								
B2-3	0.5 C	3.0	6.681	25.449	-		-	B6
B2-3	Load curve	3.0	6.55	24.073	98.05%	98.05%	1.0101	B6

Table J-1: Complete results from test B-2 regarding Peukert's effect and charge / discharge efficiency.

Appendix K – Maccor build test software setup

The battery tests performed in tests B and C are based on the Maccor 4200 series equipment. Using the associated build test – software, test are programmed in a step by step procedure each step is manually programmed. The excerpt in figure SS show parts of test C2 test build up. Using the fastwave protocol configured in Microsoft Excel with a predefined power – load the load curve is looped in a repeating sequence until end conditions are met. The error noticed in test C2 is due to a faulty logical operator in step 21. In this step, the battery is set to rest until temperature exceeds 35 degrees. This is a simple error, as the logical operator has erroneous polarity. Unfortunately, there was not sufficient time to repeat the test after the fault was discovered. Because of this, only 103 cycles were performed for test C2.

Step	Type	Mode	Value	Limit	Value	End Type	Op	Value	Goto	Report Type	Value	Options
13	Do3											
14	Advance Cycle											
15	Rest					Thermocouple	<=	1 / 55,0	016	Step Time	00:00:01	ANNN
16	FastWave	FileName	Reduced_life_cycle			Thermocouple	>=	1 / 60,0	017			
17	Rest					Thermocouple	<=	1 / 55,0	018	Step Time	00:00:05	ANNN
18	Discharge	Current	7.0			Voltage	<=	3,1	021	Step Time	00:00:01	ANNN
						Step Time	=	00:00:01	019			
						Voltage	<=	2,7	025			
						Amp Hour	>=	1,0	019			
19	Rest					Step Time	=	00:00:20	020			ANNN
20	Loop3					Loop Count	=	30	021			
21	Rest					Thermocouple	>=	1 / 35,0	022	Step Time	00:00:05	ANNN
22	Loop2					Loop Count	=	25	023			
23	Loop1					Loop Count	=	8	024			
24	Charge	Current	7.0			Voltage	>=	3,8	025	Voltage	0,05	ANNN
						Step Time	=	01:30:00	025			
						Amp Hour	>=	8,0	025			
						Thermocouple	>=	1 / 45,0	025			
25	End											

Figure K-1: Maccor Build Test software build-up. The C-2 test error can be seen in step 21, where the logical operator has reversed polarity.

Appendix L – Summary of faults during water brake testing

Voltage measurement

The most protruding fault during the water brake tests were unstable voltage measurement by the AMS. As the AMS detects a voltage below the critical value of 3.05, it enters fault mode and opens the shutdown circuit. Through troubleshooting it was discovered that several of the aluminum bus bars between cells were pulled unevenly together. This resulted in poor connection between the cell-tabs and the top plate. To rectify these errors, the connections were drilled open and connected again. While repairing it was also noticed that some of the connections were proper pressure was not applied had oxidized. The bus-bars were opened and sanded over again.

The problem was severely reduced, but still some measurements occasionally return erroneous values. After thorough troubleshooting it was discovered that the $0.2mm^2$ cables used had poor mechanical strength and wires inside the conductor were easily damaged. By replacing several cables and installing them carefully, the AMS voltage measurements worked satisfactory.

Discharge resistor

When the AMS enters fault mode during charging it is supposed to open shutdown circuit through the power stage relay and send a CAN message to the charger modules to stop it. Some situations where the charger did not cooperate with the AMS to stop charging occurred. In this instance the charger directs current trough the discharge resistor instead of the accumulator. As the discharge resistor is not dimensioned to handle elevated currents, this posed a potentially hazardous situation. At one point the discharge resistor exploded and was in danger of short-circuiting the whole accumulator.

In order to prevent this from happening again an extra relay (K13) was installed in the shutdown circuit. One of the relay contacts is connected in series with charger relay coil and in that way physically shuts down the charger when the shutdown circuit is opened.

EMI

During the initial period of the tractive system tests the PMSM was controlled by regulating speed. When operated in this mode, the communication system in the AMS was taken out by EMI. Within moments after activating the IGBTs, the AMS reported critical values and communication errors. The behavior was coherent with the results from the EMI – tests. Situation was bettered by covering both the inverter and the accumulator in a provisional aluminum blanket. Applying torque control instead of speed control to the PMSM, the EMI problems were denoted to history.

Unfortunately, the cause of the increased disturbance when using speed control could not be resolved.